Manipulation of Phase and Polarization with Liquid Crystal Technology and its Application in Advanced Optics

Fatimah Alsaiari

A thesis submitted

in partial fulfillment of the requirements

for the Doctorate in Philosophy degree in

Physics

Ottawa Carleton Institute of Physics

Faculty of science

University of Ottawa

Abstract

The use of Liquid Crystal (LC) materials, mainly in display applications, has contributed to major advancement in liquid crystal science and technology. New and more complex phases of liquid crystals were developed to compete with conventional nematic LC displays. The challenge now is to manufacture high birefringence liquid crystal materials with low viscosity. LC is also used in many other applications, such as temperature sensors and photonics beam shaping in the form of spatial light modulators (SLM) and q-plates. The first objective of this thesis is to investigate the magic mirror effect using a SLM following Sir Michael Berry's theory. Here, we demonstrated a simple way of producing the magic mirror effect using LC devices and aimed to use a micron-sized device to shape the phase and polarization of light with gentle phase variation. We were able to generate the magic mirror image intensity pattern, both experimentally and theoretically. This was done by computing and generating the desired phase pattern of an image on the SLM, then aligning light propagation through this phase pattern. The experimental and theoretical results showed good agreement when comparing the produced intensity patterns. In the second part of this thesis, we experimentally investigated the use of structured photons, created using q-plates, which is a birefringent liquid crystal cell of OAM and SAM coupling, in quantum key distribution (QKD) using the BB84 protocol through orbital angular momentum (OAM) maintaining optical fibres. Here, we were successful in generating a secure key between two parties with a quantum bit error rate of 8.6% which is below the security threshold of 11%. This work demonstrates the feasibility of using structured light in QKD through fibres to boost key rates and security.

Acknowledgements

I offer my honest gratitude to my supervisor, Dr.Ebrahim Karimi, whose contributions to my research, and studies in Quantum Optics cannot be overemphasized. He always supported me with great guidance and encouragement, especially he helped me through the most difficult times during my research program, and I will not forget it. He gave me valuable advice and ideas during the whole PhD study.

I would thank Dr.Ravi Bhardwaj, Dr.Lora Ramunno, for their support as members of my graduate advisory committee.

Also, I would like to express my thanks to my SQO members. We were not just a group; we were work as a family. That has been done by encouragement and support from our supervisor. Thanks to Alicia, Felix, Reza, Alessio, Fred, Qasem, Sajdah, Manuel, Dilip, Kevin, Florence, Yingwen, Sana, Maryam, Robert, and Hugo. Special thanks to Rezae, Alicia, Felix, Fershad, Alessio, Fred, Robert for making all of the works presented in this thesis possible.

I would like to express my external gratitude to my dear mother, Sikinah Hussain, my deceased father, for their unconditioned support and prayers. I would like to thanks my brother Saleh, Sulaiman and sister Sharifah, Maryam, and Mubarkh.

I would like to thank the Ministry of Higher Education that gave me a chance to continue my education in Canada and complete my PhD degree. Also, I would like to thank the Saudi cultural bureau for their continued support in Canada. Special thanks to Drs. Faika and Nouah.

Also, many thanks to all my friends for their understanding and supporting me during study time. Special thanks to my friend Farah Hussain who helped me a lot and support me.

Finally, this last word of acknowledgment I have saved for my husband Rashed Alshmasy who with his continued and unfailing love, support and understanding made the

completion of the thesis possible. He has been with me all these years and has made them the best years of my life throughout this journey in Canada. I appreciate my kids Abdurahman, Shama, and Sikinah for their patience. Words would never say how grateful I am to them.

Dedication

To my husband, Rashed Alshamasy, and our children. To my mother, brother and sisters, especially Maryam Alsaiari.

Publications and Presentations

First project: Magic Mirror

The results published in a peer-reviewed journal of optics in 2022. Also, the results present in Optica journal news.

Peer-reviewed publication: Felix Hufnagel, Alessio D'Errico, Hugo Larocque, Fatimah Alsaiari, Jeremy Upham, and Ebrahim Karimi, Flat magic window, *Optica* **9**, 479-484 (2022).

My contribution: performing the numerical calculation for the magic mirror, finding proper phase patterns, building the experimental setup, and recording all data with the spatial light modulator. Characterization of q-plates.

Second project: Quantum Key Distribution through Vortex Fibre

The results published in a peer-reviewed journal of optics in 2018 and are presented in several national and international conferences.

My contribution in the lab for the quantum key distribution (QKD) project was focused on the alignment of the source and building it, alignment the optical fibre, measuring photons counts, making a very narrow band pass filter using gratings and a slit, collecting the data for polarization tomography, running the experiment and taking the data for the QKD protocol.

Peer-reviewed publication: Alicia Sit, Robert Fickler, Fatimah Alsaiari, Frédéric Bouchard, Hugo Larocque, Patrick Gregg, Lu Yan, Robert W. Boyd, Siddharth Ramachandran, and Ebrahim Karimi, Quantum cryptography with structured photons through a vortex fiber, *Optics Letters* **43**, 4108-4111 (2018).

Conference presentation: Fatimah Alsaiari, Alicia Sit, Frederic Bouchard, Lu Yan, Patrick

Gregg, Hugo Larocque, Robert Fickler, Andrea Rubano, Lorenzo Marrucci, Robert W Boyd, Siddharth Ramachandran, Ebrahim Karimi, Quantum Key Distribution with structured photons in optical vortex fiber, Photonic North Conference, June 8, 2017, Ottawa, Canada.

Table of Contents

List of Tables

List of Figures

Chapter 1

Introduction

This chapter is an introduction and an overview of what has been reported in the literature regarding to magic mirror and quantum key distribution. We also introduce our contribution in the field, followed by physics background, and the thesis outline.

1.1 Literature review

In the year 1888, Austrian scientist Friedrich Reinitzer discovered the field of liquid crystal science, reporting the double melting point of the cholesterol benzoate hence the in-between state was termed as liquid crystal phase. Since the discovery, liquid crystals(LCs) became a focal point of research engaging scientists and engineers around the globe exploring the potential and application of such exotic crystal phase of matter. Widespread applications of LC technology were in the field of photonics [26], integrated optics [110], sensing/detecting [112], digital displays [92] etc. Liquid Crystals owe their various physical properties such as inducing large phase shifts due to high optical anisotropy and compatibility with silicon based technology/VLSI [116] as reorientation of molecular optical axis requires very low external voltage control because of strong electro-optic effect in LCs. Optical devices based on LCs have been the driving force behind many technological/research

breakthroughs in the field of photonics [106, 40]. Voltage controlled molecular optical axis tilt also termed as voltage induced birefringence pave the basis for phase and amplitude modulation in the optical devices based on LCs under the influence of external electric field. Spatial light modulator(SLMs) [97],q-plates [105, 66], polarization grating [62], LC actuators [80]etc. are just a few examples of LC based optical devices. More recent applications based on a mixture of different families of LCs provide wideband frequency-based birefringence at constant voltage amplitude [32, 12]. The possibility of controlling multiple properties i.e. electric permittivity, elasticity, optical refractive indices at the molecular level makes LC based technology a primary candidate for first generation molecular electronic devices [45].

In this thesis, we endeavor to make our contributions to the field of photonics by demonstrating the application of liquid crystal in the magic mirror effect, using SLMs, and in quantum key distribution, using q-plates.

Historically, the oriental magical mirror received great attention from the optics community [94]. According to Se-yuen Mak, the mirror cast in bronze dates back to the Han Dynasty (206 BC-24 AD) [73]. In oriental magic mirrors, relief undetectable by the naked eye can cause the surface to reflect an incoming beam and create a distinct pattern onto a screen corresponding to the back pattern [94]. It is suggested that light is transmitted from the bronze mirror, and this mirror can produce a real image on the wall. The bronze mirrors were known almost 2000 years ago, and people lost the technique of fabrication. Now in China and Japan, with modern technology, scientists are able to produce the magic mirror. However, the scientific principle behind this magic mirror is still a puzzle for the physicist [73].

Scholar Kua Shen [27] explains that the effect of this magic mirror is caused by small deformations of the profile as the thinner part cools faster than the thicker part, and this is not observable by the eye. Also, he noted that the very thin mirrors did not have this property which gives acknowledgment to the ancients' high skill. Dzhou Mi [27] found a

mirror from the end of the 13th century that reproduced, in reflected light, the details of an image from the backside of the mirror. More details on the physics behind understanding the image formation process will be provided later in chapter 4.

Sir Michael Berry [13] was the first to resolve the mystery of the magic mirror and explain its theory. He described the action of the magic mirror using the coordinates transformation and in terms of the Laplacian of the surface relief. Our work applies the theory to flat optics. We generate a 'Flat' magic window where, instead of the surface relief, the refractive index gently varies across the plate surface. In addition, we demonstrated the generation of this magic mirror, also known as Laplacian magic windows. With such windows, we can look through the window and not observe any patterns, however, upon light propagation through it, an interesting intensity pattern will appear. To achieve this, we took an image and computed the desired phase pattern which we imprinted on an SLM. Then, by reflecting light off this phase pattern, the intensity pattern of the image appears after a certain propagation distance of the light beam.

Information security plays a pivotal role in our lives by keeping our personal digital data secure, as for example securing our social media data like our political inclination, our personal banking details, online shopping, e-mail accounts, and banking passwords, etc. As more and more security concerns arise, the need for information security is intensifying and standards for this security becoming higher. Quantum information technologies such as quantum computation, quantum sensing and quantum cryptography [122], will most definitely define the future of information security technologies.

Quantum key distribution (QKD) allows the sharing of a secure key between two parties using quantum mechanical properties of photons. Theoretically, the protocols of QKD are 100% secure, any attempts of eavesdropping will introduce noise in the quantum channel which can be picked up immediately by the two communicating parties. The foremost QKD channels are through optical fibres and free-space links containing the following linkage configurations, ground-to-ground and satellite- to-ground [70]. QKD systems using optical

fibre links are available commercially [81]. Regarding the other channel category, several ground-to-ground links throughout the globe are built to test standard QKD protocols ranging from several hundred meters, similar to the ones used in the USA, to intra-city types reaching several kilometers as the ones installed in Vienna (Austria) [64], and in some parts of Canada (Ottawa) [102]. Two years ago, a threshold to a global quantum network was set after establishing successful connections between satellites and ground stations for QKD in China and Italy [121, 121, 113]. Aside from both categories, scholars of this field are also investigating quantum communication through underwater channels [20, 100].

In this study, we demonstrate QKD using photons containing orbital angular momentum (OAM) degrees of freedom through a vortex fibre by following the BB84 protocol [10]. Practically, it is not expedient to use a standard step-index fibre for quantum communication tasks using spatial modes of light as these modes are not preserved in step-index fibre. The vortex fibre is a unique fibre having a ring of higher refractive index towards the edge in its transverse profile which preserves the OAM modes of light through propagation, as its profile mimics the OAM beam modes. This vortex fibre has been fabricated by our colleagues from Boston University [22]. We use liquid crystal devices, know as q-plates, to generate the desired OAM modes of light required for this demonstration.

1.2 Physics Background

Maxwell's equations form the foundations of classical electromagnetism and classical optics. From Maxwell's equations one can obtain the electromagnetic wave equation, which in the paraxial limit describes the propagation of laser beams. The solutions to the paraxial wave equation includes Laguerre-Gaussian (LG) modes in cylindrical coordinates and Hermite-Gaussian (HG) modes in Cartesian coordinates. As a photon has different degrees of freedom including spin angular momentum (SAM) and orbital angular momentum (OAM), combining SAM and OAM may lead to interesting polarization and phase profiles

in the beam. These combined states are often referred to as the structured light and some examples of these states include vector vortex modes and poincaré beams. In the next section, Fresnel diffraction and Fraunhofer diffraction will be discussed.

1.3 Maxwell's Equations

Electromagnetic energy can be transformed into thermal or mechanical energies. For instance, a particle with a charge q travelling with a velocity v in the presence of EM field will experience a force, known as the Lorentz force, given by

$$\vec{F}(\vec{r};t) = q\left(\vec{E}(\vec{r};t) + \vec{v}\times\vec{B}(\vec{r};t)\right) \tag{1.1}$$

In Cartesian coordinates, the Lorentz force can be expressed as

$$F_i = q(E_i + \varepsilon_{ijk} v_i B_k) \tag{1.2}$$

Here,the Levi–Civita symbol ε_{ijk} was used to express the cross product term $\vec{v}\times\vec{B}$. ε_{ijk} is equal to 1 for even permutations of ijk and 0 for odd permutations. In addition its also zero for repeated incidies, eg, xxy or xxx.

The work carried out by the Lorentz force on a charged particle moving with a velocity $\vec{v}$ in a time interval t_0 to t_1 is given by

$$W(t_0,t_1) = \int_{t_0}^{t_1} dt\, v_i F_i = q\int_{t_0}^{t_1} dt\, v_i E_i \tag{1.3}$$

For a charge distribution in the presence of an electric field, a more general form than 1.3 (which is only for a point charge) is product of the charge flux density, $j = \rho\, v$, and electric field

$$q^E = -j_i E_i = -\vec{j} \cdot \vec{E}, \tag{1.4}$$

where q^E is the energy density associated with a moving charge distribution in an EM field [2].

In the absence of a free charges and currents, the Maxwell's equations in a vacuum can be written as

$$\vec{\nabla} \cdot \vec{E} = 0 \tag{1.5}$$

$$\vec{\nabla} \cdot \vec{B} = 0 \tag{1.6}$$

$$\vec{\nabla} \times \vec{E} = -\frac{\partial \vec{B}}{\partial t} \tag{1.7}$$

$$\vec{\nabla} \times \vec{B} = \varepsilon_0 \mu_0 \frac{\partial \vec{E}}{\partial t}, \tag{1.8}$$

where $\vec{E}$, $\vec{B}$, μ_0, ε_0 are the electric field, the magnetic field, vacuum permeability and permittivity constants, respectively.

After taking curl of equation (1.7) and equation (1.8), we can obtain the wave equations for E and B fields

$$\left(\nabla^2 - \mu_0 \varepsilon_0 \frac{\partial^2}{\partial t^2} \right) \vec{E}(\vec{r}, t) = 0, \tag{1.9}$$

$$\left(\nabla^2 - \mu_0 \varepsilon_0 \frac{\partial^2}{\partial t^2} \right) \vec{B}(\vec{r}, t) = 0, \tag{1.10}$$

where ∇^2 is the Laplacian. The general form of the wave equation for a scalar function $\psi(\vec{r}; t)$ is given by

$$\left(\nabla^2 - \mu_0 \varepsilon_0 \frac{\partial^2}{\partial t^2} \right) \psi(\vec{r}, t) = 0 \tag{1.11}$$

After substituting $\psi(\vec{r}; t) = \varphi(\vec{r}) \exp(-i\omega t)$ into equation (1.11), and using the separation

of variables, one can obtain the Helmholtz equation

$$\left(\nabla^2 + \frac{\omega^2}{c^2}\right)\varphi(\vec{r}) = \left(\nabla^2 + k^2\right)\varphi(\vec{r}) = 0, \tag{1.12}$$

where $k = \omega/c$ is wave vector of the electromagnetic field.

For a special case where the beam propagates along the z-direction, $\exp(ikz)$, equation (1.12) yields

$$\left(\frac{\partial^2}{\partial x^2} + \frac{\partial^2}{\partial y^2} + \frac{\partial^2}{\partial z^2} + 2ik\frac{\partial}{\partial z}\right)\varphi(r) = 0. \tag{1.13}$$

Using equation (1.13) and the dimensionless variables $u = x/\omega_0$, $v = y/\omega_0$, and $\zeta = z/z_R$, one can obtain the paraxial wave equation, given below

$$(\partial_u^2 + \partial_v^2 + 4i\partial_\zeta)\varphi(u, v, \zeta) = 0 \tag{1.14}$$

where $z_R = \frac{kw_0^2}{2}$ is the Rayleigh range. Equation (1.15) arises from (1.13) after the paraxial approximation where the $\partial^2/\partial z^2$ term is dropped

$$-\frac{1}{2k}\nabla_\perp^2\varphi(\vec{r}_\perp, z) = i\partial_z\varphi(\vec{r}_\perp, z), \tag{1.15}$$

where $\nabla_\perp^2$ is the transverse Laplacian operator and $\vec{r}_\perp = (x, y)$. By replacing the longitudinal coordinate z with time t, the free particle Schrödinger equation will be identical to paraxial wave equation, as written

$$-\frac{\hbar^2}{2m}\nabla^2\Psi(r, t) = i\hbar\frac{\partial}{\partial t}\Psi(r, t), \tag{1.16}$$

where is ∇^2 is the Laplacian, $\hbar$ is the reduced Planck constant, m is the mass of the particle. There are several solutions to the paraxial wave equation, such as Laguerre-Gaussian and Hermite–Gaussian [2].

Hermite–Gaussian beams

Hermite–Gaussian beams form a complete set of solutions for paraxial wave equation. Hermite–Gaussian modes in Cartesian coordinates are given by [39]

$$\psi_{m,n}(\vec{r}) = \sqrt{\frac{2}{\pi\omega^2(z)}} H_m\left[\frac{2x}{\omega(z)}\right] H_n\left[\frac{2y}{\omega(z)}\right] \times \exp\left[-i(m+n+1)\Phi(z) + \frac{ik\rho^2}{2q(z)}\right] \quad (1.17)$$

where H_m is the Hermite polynomial of order n and argument x, $\rho = \sqrt{x^2+y^2}$ is the radial distance,$\Phi(z) = \tan^{-1}\left(\frac{z}{z_0}\right)$ is phase angle, and $q(z)$ is complex beam parameter.

Laguerre–Gaussian beam (LG)

The Laguerre-Gauss modes (LG) form a complete orthonormal basis set of solutions for paraxial wave equation. LG modes in cylindrical coordinates (ρ,φ,z) for a complex scalar function are given by

$$\begin{aligned} \mathrm{LG}_{p\ell}(\rho,\varphi,z) = & \sqrt{\frac{2p!}{\pi(p+|\ell|!)}} \left(\frac{\omega_0}{\omega(z)}\right) \left(\frac{\sqrt{2}\rho}{\omega(z)}\right)^{|\ell|} \exp[-\frac{\rho^2}{\omega(z)^2}] L_p^{|\ell|}\left(\frac{2\rho^2}{\omega(z)^2}\right) \\ \times & \exp\left[i\left(\ell\varphi - \frac{k\rho^2}{2R(z)} + (2p+|\ell|+1)\tan^{-1}\left(\frac{z}{z_R}\right)\right)\right] \end{aligned} \quad (1.18)$$

Here, $\ell \in \{0, \pm1, \pm2, \ldots\}$ is the index of the azimuthal mode, $p \in \{0, 1, 2, \ldots\}$ is the index of the radial mode, $L_p^{|\ell|}$ is the generalised Laguerre polynomial, $\omega(z) = \omega_0(1+(\frac{z}{z_R})^2)^{\frac{1}{2}}$ is the beam's waist at $z = 0$, z_R is the Rayleigh range, k is the wave number, $R(z) = z(1+\left(\frac{z_R}{z}\right)^2)$ is the radius of curvature, and $(2p+|\ell|+1)\tan^{-1}\left(\frac{z}{z_R}\right)$ is Gouy phase.

LG modes possess an azimuthal phase front, i.e., $\exp(i\ell\varphi)$, which is an eigenstate of the z-component of orbital angular momentum (OAM) operator $L_z = -i\hbar\partial_\varphi$. Indeed, optical angular momentum can be separated into spin angular momentum (SAM) and orbital angular momentum (OAM) components in the paraxial regime for a monochromatic beam.

As briefly mentioned, the OAM depends on the phase front, while the SAM is associated with the vectorial nature of the electric field's oscillation. OAM defines light with a helical phase front, and each photon carrying this helical wavefront carries an integer OAM value of $\ell\hbar$ [1]. Figure 1.1 shows theoretical intensity profiles, and phase in the transverse plane and along the propagation direction for OAM values of $\ell = 0, \pm 1, \pm 2$. Due to the nature of the cylindrical coordinates, the azimuthal phase φ is undefined on the beam axis leading to a phase singularity which consequently results in a dark region intensity profile [83] - this is shown in the middle column of Figure 1.1. ℓ and p roles in the intensity and phase distribution depend on their values. Therefore, if p and ℓ values are zero, the fundamental beam, also known as the Gaussian beam, will register, and for the intensity profile, the phase is a constant flat. If p's value is zero and ℓ is one, the intensity will look like a ring with a maximum at a certain radius; however, the phase is increasing azimuthally. For ℓ=2, the ring-like shape becomes bigger compared to the previous scenario, and the azimuthal phase variation is faster, becoming twice faster. For a negative ℓ, for instance, (-1, -2, ... etc.), it will be the same case, but the phase change will be counter-clockwise. In summary, as ℓ increases, the radius gets bigger, and as p increases, extra rings with opposite phases are added.

The optical beams carrying OAM, i.e., OAM modes, can be generated by controlling the incoming beam using various devices, including spiral phase-plates, spatial light modulators (SLMs), or a q-plate [7, 49, 77, 54, 21, 66]. The OAM modes have found many applications in classical optics such as optical tweezers, imaging, lithography [3, 41, 50, 87, 46] as well as applications in quantum information processing, and more specifically in quantum cryptography [114, 19].

Combining two photonics degrees of freedom (DOF), e.g., SAM and OAM, may lead to interesting applications in high-resolution imaging and optical metrology. Such states are known as the structured light and examples include the Poincaré [5] and vector vortex beams [25], which possess a space-varying polarization profile [96].

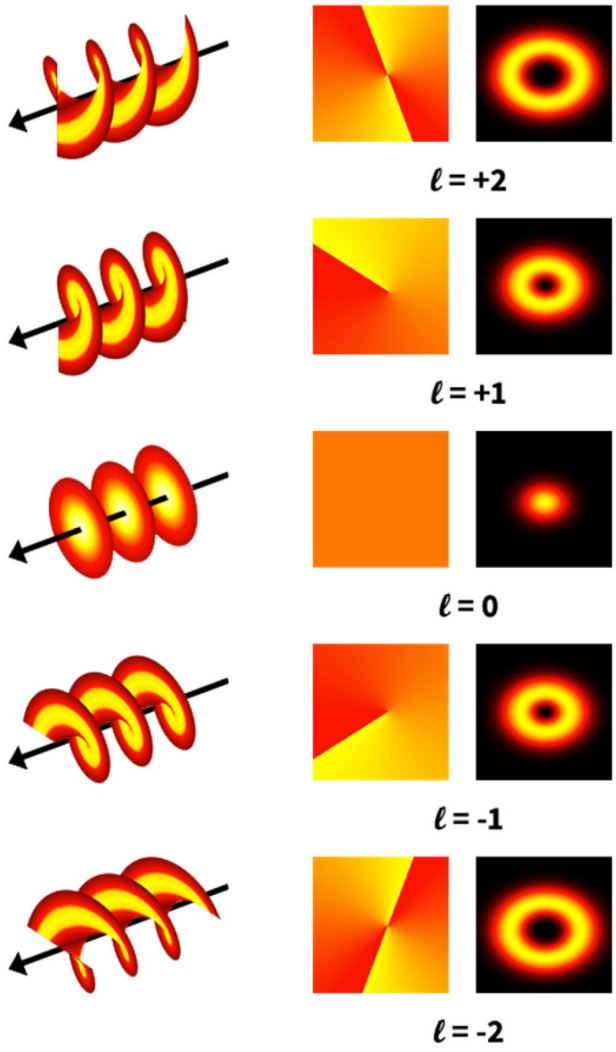

Figure 1.1: Illustration of the wavefront distributions, phase and intensity for optical beams carrying orbital angular momentum of $\ell = 0, \pm 1, \pm 2$. The left column is the wavefront, the middle column is phase and the right column is intensity. When $\ell = 0$ the wavefront distributions are those for a Gaussian beam and the phase is constant. When $\ell = 1$ the wavefront has a helical form and the phase changes by φ and intensity has a doughnut-shape [15].

1.4 Polarization of Light

Light is an electromagnetic wave consists of oscillating electric and magnetic fields which are mutually orthogonal. The oscillation direction of the electric field is commonly referred to as the polarization direction. Depending on the electric field's oscillations' geometry, three main classes of the polarization are linear, circular, and elliptical. For plane wave

beam propagating in the z-direction, the polarization can be expressed, in the transverse plane, using a normalized complex vector by

$$\vec{E} = \begin{bmatrix} a_x e^{i\varphi_x} \\ a_y e^{i\varphi_y} \end{bmatrix}, \tag{1.19}$$

where a_x, φ_x and a_y, φ_y are the amplitudes and the phases of the x and y components of the electric field, respectively.

For linearly polarized light, the electric field's amplitude is constant and it only oscillates in one direction which is perpendicular to the propagation direction. Therefore, in a linearly polarized light, the electric field is restricted to only one plane in the propagation direction. For a circularly polarized light, the amplitude of the electric field is constant, but the direction that the electric field vector rotates around is perpendicular to the propagation direction. A circularly polarized light comprises of two orthogonal linear components which have a phase difference of $\pi/2$. In our adopted sign convention: if the electric field rotates clockwise (counter-clockwise) with respect to the propagation direction, it is called right (left) circular polarization. In an elliptically polarized light, the amplitude of the electric field is not constant and it rotates on a plane perpendicular to the propagation direction. An elliptically polarized light comprises of two orthogonal linear components with a phase difference other than $\pi/2$.

An elliptical polarization can be represented by polarization ellipse described by the angle of the electric field vector from the major axis denoted by ψ, and the eccentricity denoted by χ, as shown schematically in Figure 1.2; the following equations can mathematically describe the elliptical polarization

$$\tan 2\psi = \frac{2r}{1-r^2}\cos\varphi, \tag{1.20}$$

$$\sin 2\chi = \frac{2r}{1+r^2}\sin\varphi, \tag{1.21}$$

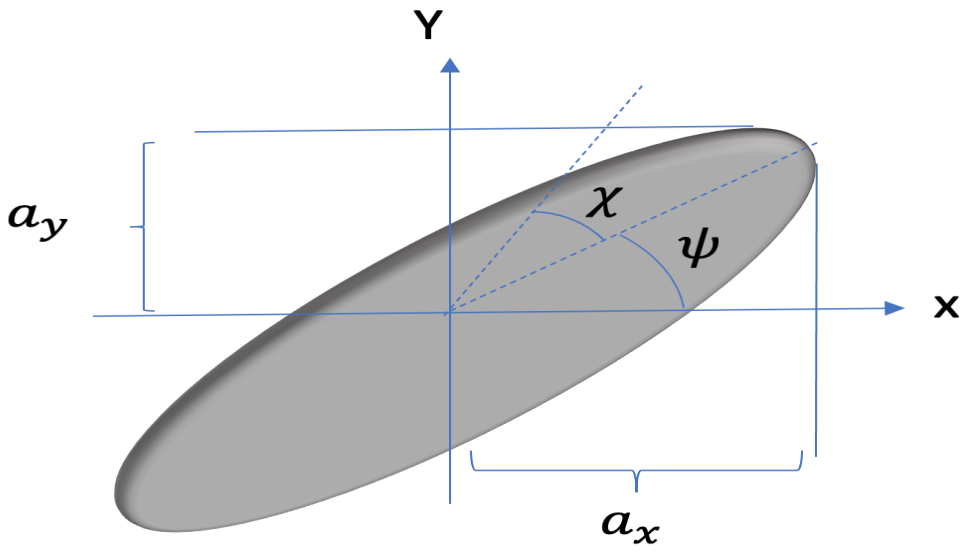

Figure 1.2: This figure explains elliptically-polarized light. The angle from the major axis is given by ψ and the eccentricity is given by χ.

where is $r = a_x/a_y$ and $\varphi = \varphi_x - \varphi_y$. Any polarization state can be represented by a point on the surface of a sphere of unit radius, as shown in Figure 1.3. This sphere is called the Poincaré sphere (PS) or the Bloch sphere. The Stokes vector (S_0, S_1, S_2, S_3) indicates the geometric location of an arbitrary polarization state on the PS as the sphere is plotted upon three dimensional Cartesian coordinates: (S_1, S_2, S_3). The quantity S_0 represents the total optical intensity, S_1 describes the horizontal and vertical (H-V) polarization bases, S_2 describes the diagonal and anti-diagonal (D-A) polarization bases, and S_3 describes the left and right circular (L-R) polarization bases. The relationships between the Stokes parameters, the polarization ellipse, and the intensity are given by

$$S_1 = S_0 \cos 2\chi \cos 2\psi, \tag{1.22}$$

$$S_2 = S_0 \cos 2\chi \sin 2\psi, \tag{1.23}$$

$$S_3 = S_0 \sin 2\chi. \tag{1.24}$$

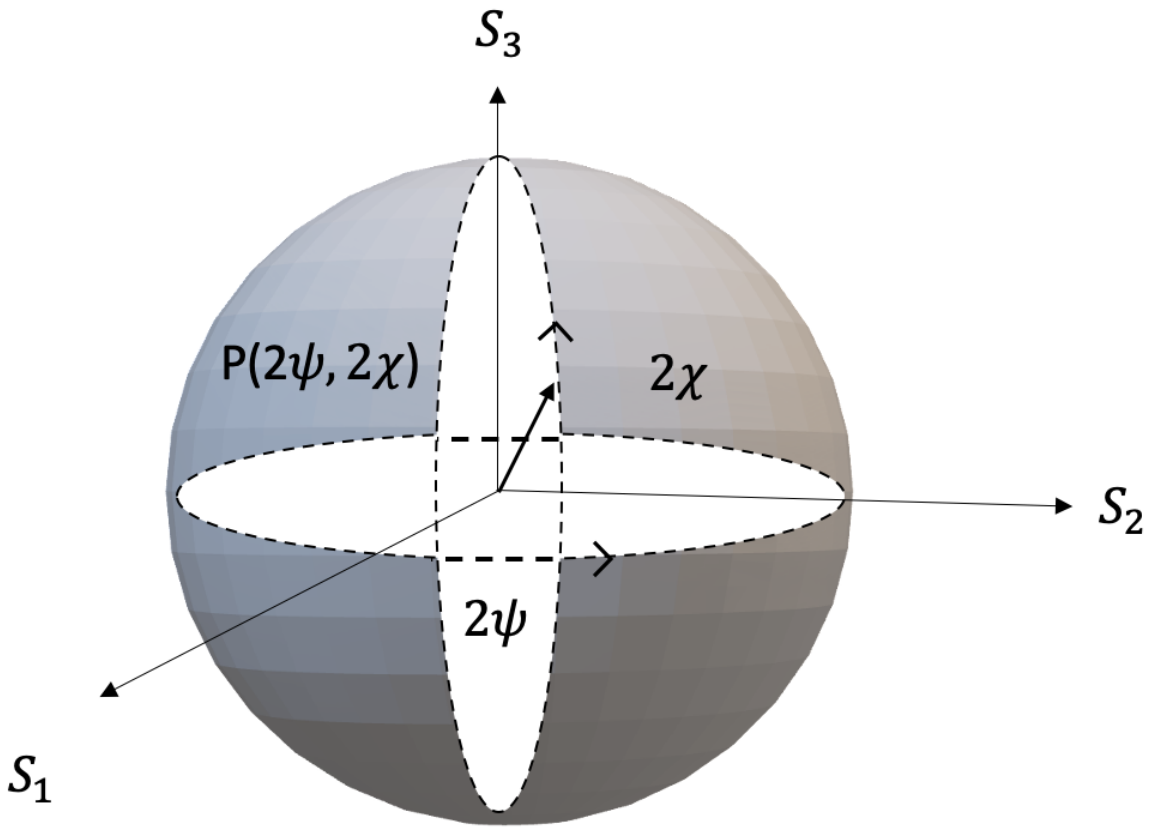

Figure 1.3: An Illustration of the light polarizations on the Poincaré sphere. Here χ is the azimuthal angle and ψ the ellipticity. The azimuthal angle χ appears from the south pole, while the ellipticity angle ψ appears from the equator to the north pole.

Using the complex vector notation, since S_0 is equal to unity ($S_0 = a_x^2 + a_y^2 = 1$), we can take $a_x = \cos\alpha$ and $a_y = \sin\alpha$. Then, the Stokes parameters can be written as

$$S_1 = E_x E_x^* - E_y E_y^* = a_x^2 - a_y^2 = \cos 2\alpha, \tag{1.25}$$

$$S_2 = E_x E_y^* + E_y E_x^* = 2a_x^2 a_y^2 \cos\varphi = \sin 2\alpha \cos\varphi, \tag{1.26}$$

$$S_3 = i(E_x E_y^* - E_y E_x^*) = 2a_x^2 a_y^2 \sin\varphi = \sin 2\alpha \sin\varphi, \tag{1.27}$$

where $*$ stands for complex conjugate, $\alpha \in [0,\pi]$, and $\varphi \in [0,2\pi]$. We should note that the angle in real space are twice of the angle shown on the poincaré sphere [74, 4, 104].

1.5 Vortex Light

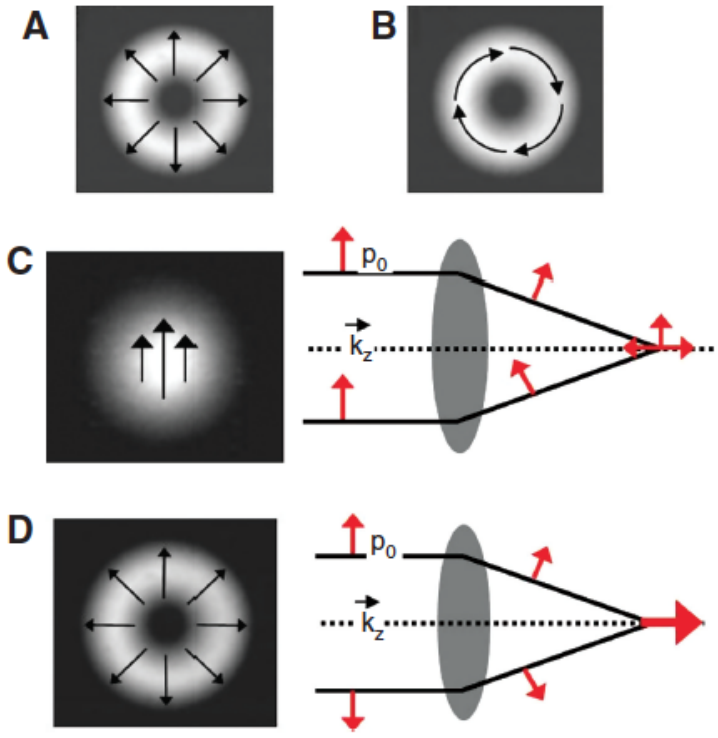

Figure 1.4: The images represent intensity profile for radially-polarised beam (B) azimuthally-polarized beams; (C, D) The focus of the beam passing high-NA lenses for different beam shapes.The red arrow is polarization orientations. High numeric aperture (NA) is effect incoming beams by shape the beam. The tide focusing beam occurs when high NA lens is close to 1. At the tide focusing regime, when the focal length is very small, the electric field points to the center. For this reason, it show as a dot as shown in the image [90].

Spatially uniform polarization adjustments characterize plane waves and Gaussian beams. It contrasts with cylindrical vector beams of the kind exhibited in Figure 1.4 A and B. These beams are known as polarization vortices since they have zero intensity at the center [90]. Radial and azimuthal polarization states are vector state examples, for they are

producible with a spatial light modulator [58], or nano-structured waveplates [66]. Under a physically instinctive manner, some fundamental variations among plane-polarized Gaussian beams and polarization vortices are visualized by considering their focusing properties during crossing through a high numerical aperture lens. Figure 1.4 C and D schematically demonstrate a Gaussian beam's focusing and radially polarized beam by a high numerical aperture lens, sequentially.

A simple ray-tracing delineation reveals that, at focus, the Gaussian beam's polarization adjustment is overly complicated, leading to self- aperturing effects. In comparison, the different spatial portions of benefactions at focus from the radially polarized beam constructively interfere to form an incredibly unique light distribution at focus [90].

1.6 Generation of Orbital Angular Momentum

There are several techniques to produce OAM beams as mentioned before such as spiral phase plate, q-plate, and hologram. The first technique to be discussed is the spiral phase plate (SPP). It is a transparent plate in which the thickness depends on the azimuthal angle φ, as shown in Figure 1.5. SPPs are optical phase components that look like a helix staircase, which can convert Gaussian input beam to an OAM beam, moreover, they were examined by Beijersbergen et al. (1994) [7]. If the incident beam is defined by the complex amplitude $u(\rho, \varphi, z)$, the amplitude u' after the plate is described by [7]

$$u' = u \exp(-i\Delta\ell\varphi) \tag{1.28}$$

The relation between the step height(h) of the plate and $\Delta\ell$ is azimuthal mode given by

$$\Delta\ell = h\left(\frac{\Delta n}{\lambda}\right), \tag{1.29}$$

where Δn is the refractive index difference between the plate and the surrounding medium, h is the excess height, and λ is the vacuum wavelength. The SPP has converted the non-helical phase front beams into beams having the helical phase front. However, it may change the helical phase front of the beam according to equation (1.28), which leads to the phase changing while the amplitude is not changing. In other words, SPP is not a pure mode convert [7, 98].

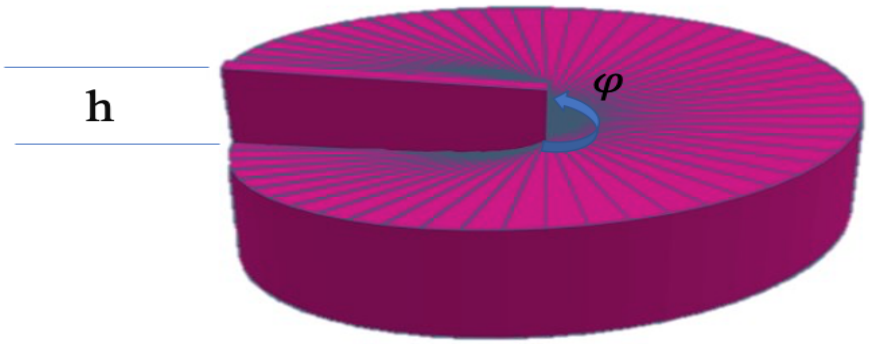

Figure 1.5: The schematic representation of spiral phase plate. Spiral phase plate converts a Gaussian to helical phased beams.

The second technique to produce OAM beams is a hologram. The hologram modifies the phase of the incident beam, which is displayed on the SLM. The LG beam with an azimuthal phase pattern is generated using the inference pattern from pitched fork hologram by illuminating them with a Gaussian beam. Due to fringes, the beam will have diffraction.

Then, holograms output after incident Gaussian beam is a zero-order beam and two conjugate first-order diffracted beams. These first-order diffracted beams contain singularity of opposite charge [48] as shown in Figure 1.6. The third technique is q-plate which will be explained in more detail in chapter 3- section 3.7.

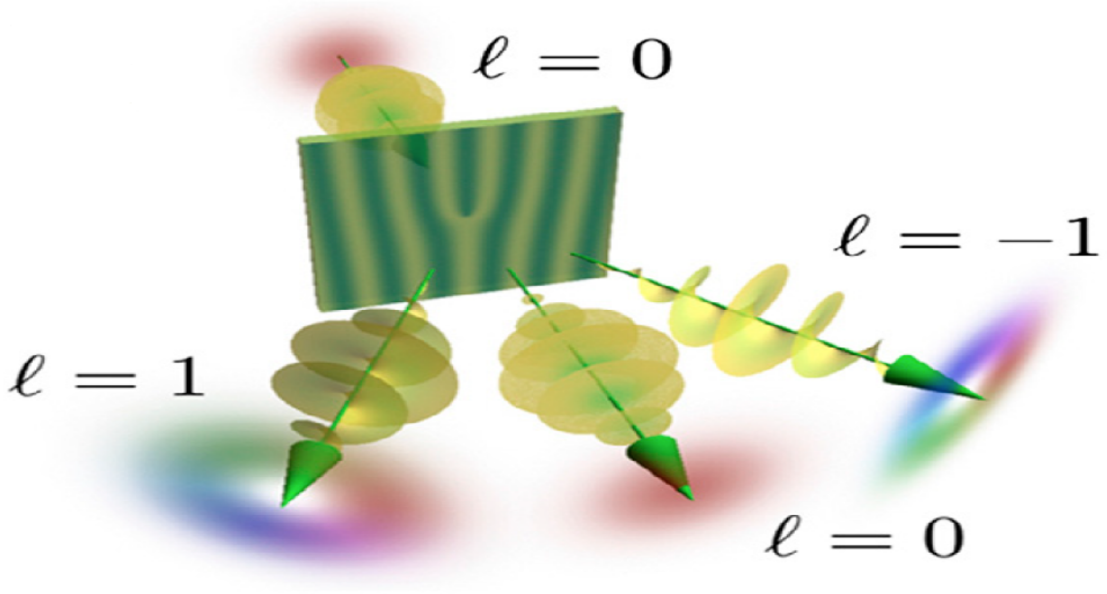

Figure 1.6: OAM formation through a hologram. The Gaussian beam converts to Laguerre-Gaussian modes with a diffraction order $\ell = \pm 1$ [67].

1.6.1 Mutually Unbiased Bases (MUBs)

Mutually unbiased bases play an important role in quantum information applications like quantum key distribution and quantum state reconstruction. The meaning of having mutually unbiased bases is that, if we know about one preparation base but not about the measurement base, for example, we prepare a quantum state in one basis (linear polarization state), then we measure the quantum state in a measurement basis, which may or may not be the same. It is important to find the maximum of MUB in Hilbert space of dimension d. The method to find the prime-power dimension by d + 1, for example for D=2 maximum MUB is three set vector, MUB is important for encoding the information on a photon using BB84 protocol [33].

If we have set of bases $|\Phi_1\rangle, |\Phi_2\rangle, ..., |\Phi_d\rangle$, $|\psi_1\rangle, |\psi_2\rangle, ..., |\psi_d\rangle$, $|\chi_1\rangle, |\chi_2\rangle, ..., |\chi_d\rangle$, each one of them is complete and orthogonal.

In BB84 for d=2, the MUB can be written as

$$
\begin{aligned}
I &= \{|\Phi_1\rangle, |\Phi_2\rangle\} \\
II &= \{\ |\psi_1\rangle, |\psi_2\rangle\} \\
III &= \{\ |\chi_1\rangle, |\chi_2\rangle\},
\end{aligned} \tag{1.30}
$$

I, II and III are three set of vector of MUB. We know $\langle\Phi_1|\Phi_2\rangle = \delta_{ij}$ and the same thing for $\langle\psi_1|\psi_2\rangle = \delta_{ij}$, $\langle\chi_1|\chi_2\rangle = \delta_{ij}$ where δ_{ij} is such that it is equal to 1 when i=j and zero otherwise. If we take one of the sets of MUB and project on other MUB, then the relationship between them is

$$
|\langle\Phi_i|\chi_j\rangle|^2 = \frac{1}{d}, \tag{1.31}
$$

where d is space dimension. In the case of polarization of light, the set of basis for the MUB can be written as

$$
\begin{aligned}
I &= \{|H\rangle, |V\rangle\} \\
II &= \{\ |A\rangle, |D\rangle\} \\
III &= \{\ |L\rangle, |R\rangle\},
\end{aligned} \tag{1.32}
$$

where is $|H\rangle$ is the horizontal polarization state, $|V\rangle$ is the vertical polarization state,$|A\rangle$ is the anti diagonal polarization state $|D\rangle$ diagonal polarization state, $|L\rangle$ is left polarization state, and $|R\rangle$ is right polarization state.

Then, by following the equations above, we have

$\langle H|H\rangle$,$\langle V|V\rangle$,$\langle A|A\rangle$,$\langle D|D\rangle$,$\langle L|L\rangle$,$\langle R|R\rangle$ =1

$\langle H|V\rangle, \langle V|H\rangle, \langle A|D\rangle, \langle D|A\rangle, \langle L|R\rangle, \langle R|L\rangle = 0.$

The rest of the vectors will give half of the probability. This is how we fill probability

density matrix as shown in Figure 1.7.

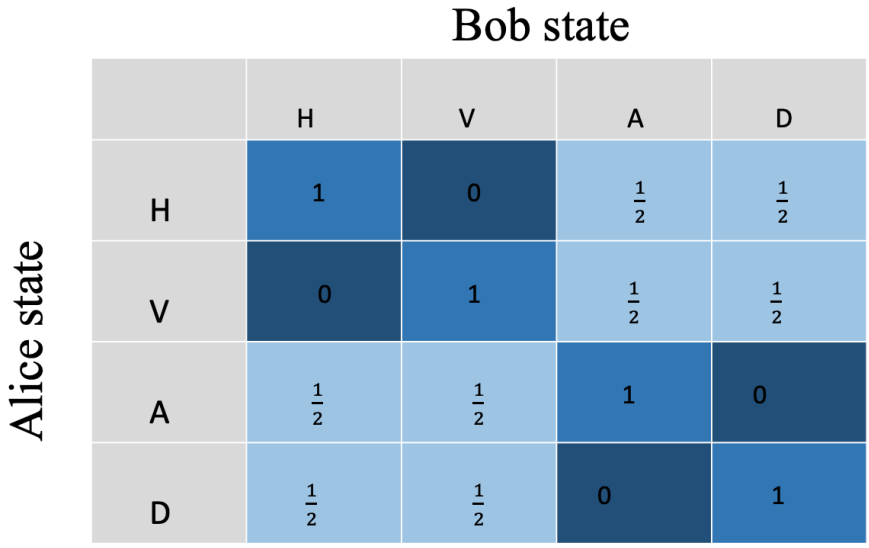

Figure 1.7: The image represents the theoretical probability of a detection matrix for an ideal BB84 for d=2). The rows representing the Alice send (H, V, A, D) are the generation states, while columns measured by Bob (H, V, A, D) are the projections states.

1.7 Polarization Tomography

This technique aims to characterize an arbitrary polarization state and its orthogonal components via the quantum state tomography. In the laboratory, we utilized the tomography to reconstruct the polarization of an unknown quantum state using a series of quarter-wave plates, half-wave plates then a polarizing beam splitter to project the polarization state, such states can be represented by higher order Poincaré sphere for Laguerre-Gauss modes [78, 25], on the three mutually unbiased bases (MUB): $(|H\rangle, |V\rangle, |A\rangle, |D\rangle, |R\rangle, |L\rangle)$ or (S_1, S_2, S_3) base. This process includes analyzing the six polarization basis vector projections $(|H\rangle, |V\rangle, |A\rangle, |D\rangle, |R\rangle, |L\rangle)$, where $|H\rangle$ is horizontal state, $|V\rangle$ is vertical state, $|A\rangle$ is anti diagonal state $|D\rangle$ diagonal state, $|L\rangle$ is left state, $|R\rangle$ is right state. The latter

states are related to $|H\rangle, |V\rangle$ polarization states via the following relations

$$|A\rangle = \frac{1}{\sqrt{2}}(|H\rangle - |V\rangle) \tag{1.33}$$

$$|D\rangle = \frac{1}{\sqrt{2}}(|H\rangle + |V\rangle) \tag{1.34}$$

$$|R\rangle = \frac{1}{\sqrt{2}}(|H\rangle - i\,|V\rangle) \tag{1.35}$$

$$|L\rangle = \frac{1}{\sqrt{2}}(|H\rangle + i\,|V\rangle) \tag{1.36}$$

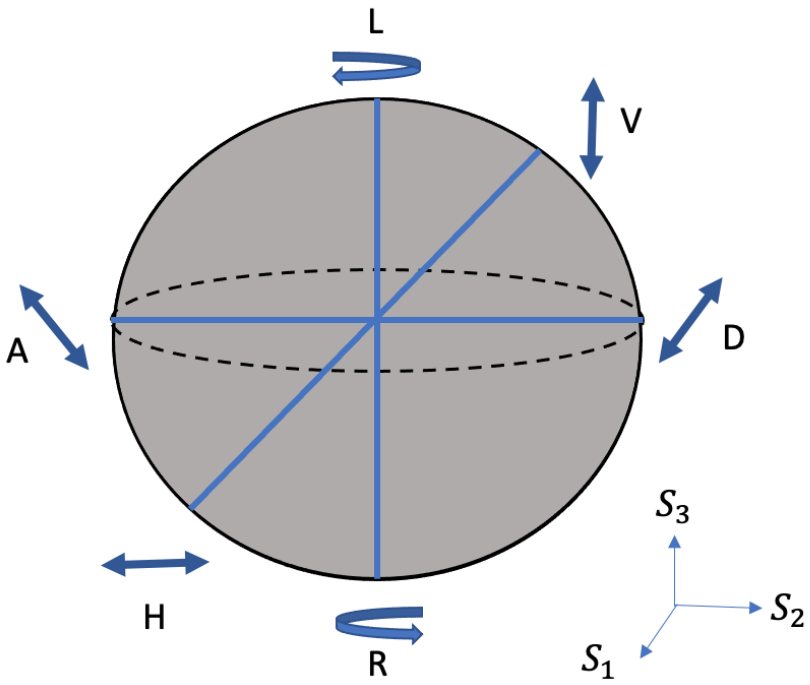

Figure 1.8: The diagram of the light polarizations on the Poincaré sphere. Linear polarization lying on the equators (H, V, A, D) and circular polarization lying on the poles (R, L), are in the following sequence: L is the left circular polarization representing the north pole and R: is the right circular polarization representing the south poles.

Each projection on the Poincaré sphere can be calculated using stokes parameters, which can be determined by recording the beam intensity profiles of each projection with

either bucket detector (for uniformly polarized optical beams) or CCD camera (for spatially structured optical beams). From each intensity profile, we can calculate the stokes parameters by given relations below

$$\begin{aligned} S_1 &= I_H - I_V, \\ S_2 &= I_D - I_A, \\ S_3 &= I_L - I_R, \end{aligned} \tag{1.37}$$

where I_H is the intensity distribution associated to the horizontal polarization state, I_V is the intensity distribution associated to the vertical polarization state, I_A is the intensity distribution associated to the anti diagonal polarization state, I_D is the intensity distribution associated to the diagonal polarization state, I_L is the intensity distribution associated to the left polarization state, I_R is the intensity distribution associated to the right polarization state.

1.8 Optical Fibre

An optical fibre is a rod-like insulator composed of a low-loss substance, such as thin silica glass, which acts as a waveguide with a step-index profile. It has a central core in which the light travels with minimal loss; all light within the central core is fully internally-reflected when it hits the outer cladding, which is made of a substance with slightly higher refractive index. In its purest form, overlooking polarization, the wave equation for transverse electric field given by [90]

$$[\nabla_t^2 + n^2 k^2]\vec{e}_t = \beta^2 \vec{e}_t, \tag{1.38}$$

where n is refractive index, k is the free-space wavevector on the basis that ($\frac{2\pi}{\lambda}$, as λ is the wavelength), and β^2 is the propagation constant.

Equivalently it is characterized by an effective mode group index through $n_{eff} = \frac{\lambda\beta}{2\pi}$. The eventual intensity distributions for e_t are presented as a diagram of n_{eff} for the three primary modes as shown in Figure 1.9 A. The close examination of the profiles of these fields suggests that regardless of the strictly cylindrically symmetric nature of optical fibres, the solutions cannot resemble vortices of the kind described in section 1.5.This fallacy is due to the scalar approximation of equation 1.38, which does not account for the index gradients. Hence, achieving accurate resolutions would require using the full vector wave equation which is written as follows [107],

$$[\nabla_t^2 + n^2k^2]\vec{e_t} + \nabla_t[e_t.\nabla_t(ln(n^2)] = \beta^2\vec{e_t} \tag{1.39}$$

where n is the refractive index of the fibre, ($k = 2\pi/\lambda$) is the wave vector e_t is the transverse electric field, and β is the propagation constant for each vector mode. Figure 1.9 B presents the related intensity distributions for e_t and the delineative designs of n_{eff}, for the full vector solution that corresponds to the same step-index waveguide. It shows that optical fibre's true modes have more mixed degeneracies, as shown in Figure 1.9 C–E. For the first higher order indicated solutions (LP_{11} modes in the scalar estimation), four modal solutions exist, TE_{01}, HE^{21}_{even}, HE^{21}_{odd}, and TM_{01} as shown in Figure 1.9 B and D. The two HE_{21} modes are clearly degenerate and have a n_{eff} separated from the TE_{01} as well as TM_{01} modes. Moreover, the higher azimuthal index ($L > 1$) with all higher-order solutions, for example, $LP_{L,m}$ modes, contain two degenerate solutions that are named $HE_{L+1,m}$, and $EH_{L-1,m}$ modes. Consequently, only one of each degenerate pair's field distribution as presented in Figure 1.9 E. Commonly, modes with almost similar n_{eff} could also have similar group velocities and contain a single-mode group. In these circumstances, the LP_{1m} mode group is the scalar approximation of the four-vector modes,TE_{01}, HE^{2m}_{even},HE^{2m}_{odd} and

TM_{01}, in addition to all other $LP_{L,m}$ at $L > 1$ mode groups that constitute HE and EH true mode mixtures.

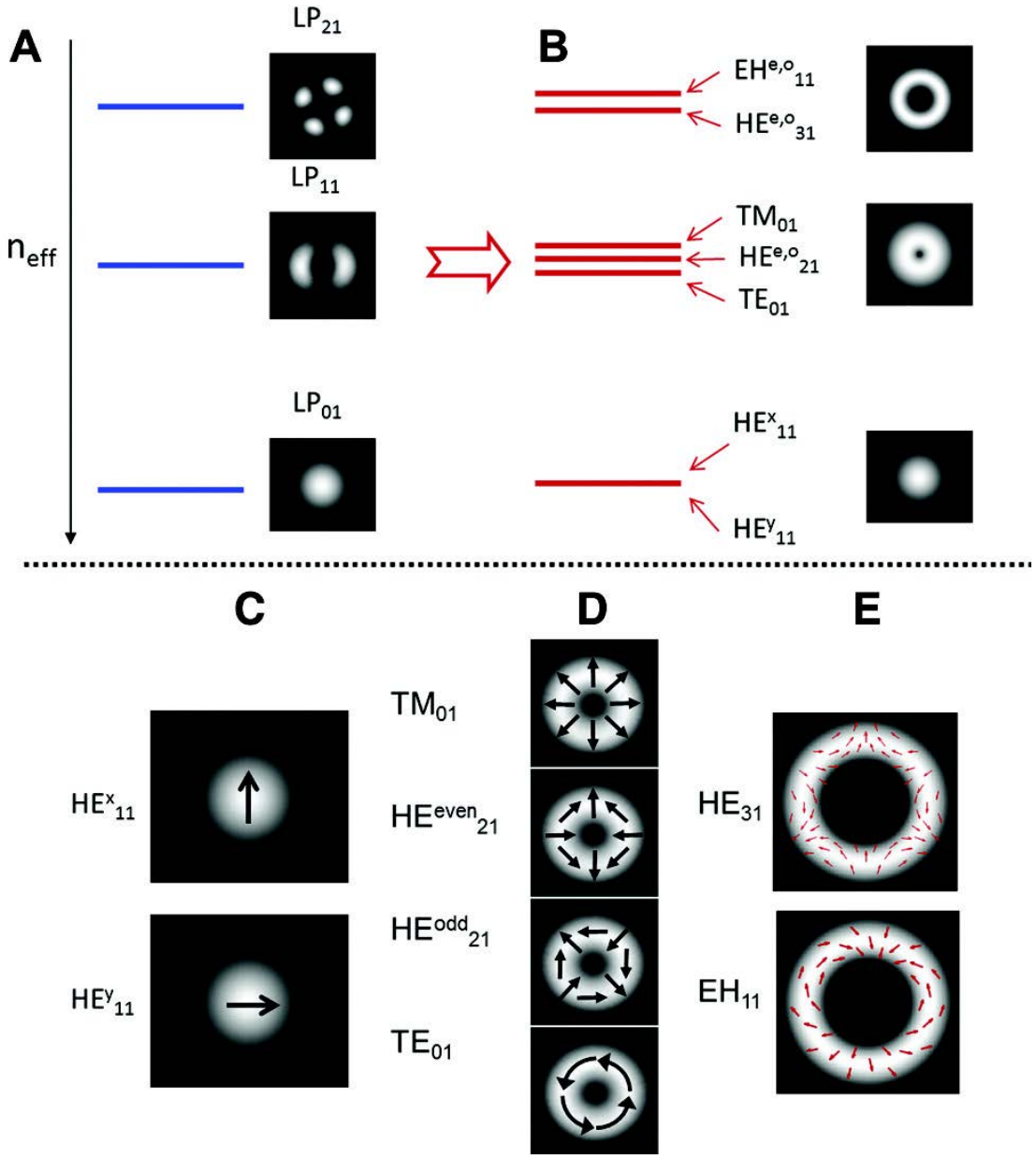

Figure 1.9: Step-index fibre modes in the (A) scalar estimation and (B) full vector solutions. Vertically accumulated lines and associated arrows exhibit comparable n_{eff} for each solution: (C, D, and E) [90].

In reviewing the allowed resolutions, as shown in Figure 1.9 D, there is evidence that shows the optic fibre is generating polarization vortex situations, for example, the azimuthally or radially polarized rays with the TE_{01}, TM_{01} fibre modes [85, 90]. More detail

is coming in chapter 5.

1.9 Fresnel and Fraunhofer Diffraction

The two comparative models are valid depending on the observation point's range related to the aperture position, the aperture capacity, and the wavelength of the incident light.

1.9.1 Fresnel Diffraction

It is noted that for a restricted aperture S_A, all the integral terms are not required to be included at distances broader than the wavelength of the incident light (λ). The Fresnel diffraction formula wide-field form is given as [61]

$$E_x(x,y,z) = \frac{1}{i\lambda}\int\int_{S_A} dx'\ dy'\ E_x(x',y',0)\,\frac{\exp(ikR)}{2\pi R}\,\frac{z}{R} \tag{1.40}$$

Assume ($\frac{z}{R} \approx 1$) and the approximation ($\frac{1}{R} \approx \frac{1}{z}$),

$$R = \sqrt{(x-x')^2+(y-y')^2+z^2} \approx z\left[1+\frac{(x-x')^2+(y-y')^2}{2z^2} - \frac{1}{8}(\frac{(x-x')^2+(y-y')^2}{z^2})^2 + ...\right] \tag{1.41}$$

where z is the distance from the centre of the aperature to the centre of the screen and R is the distance between each point on the aperature and each point on the screen. The third term in the binomial expansion above is dismissible if the value is below 1 radian, then the condition becomes

$$z^3 \gg \frac{k}{8}\left[(x-x')^2+(y-y')^2\right]^2_{max} \tag{1.42}$$

Applying this condition to equation 1.40, then Fresnel diffraction can be written as [61]

$$E_x(x,y,z) = \frac{\varrho^{ikz}}{i\lambda z}\int\int_{S_A} dx'dy' E_x(x',y',0)e^{\frac{i\pi}{\lambda z}\left[(x-x')^2+(y-y')^2\right]} \tag{1.43}$$

It is important to maintain under consideration that the equation above is for the field distribution's 2D convolution in the $(z = 0)$ plane beside the Fresnel impulse response $h_F(x,y,z)$ which is given by

$$h_F(x,y;z) = \frac{exp(ikz)}{i\lambda z}\exp\left[\frac{i\pi}{\lambda z}(x^2+y^2)\right]. \tag{1.44}$$

1.9.2 Fraunhoffer Diffraction

The Fraunhofer diffraction model additionally converges the Fresnel diffraction. The Fresnel diffraction relation from equation (1.43) will slightly differ with the below modified form [61]

$$u(x,y,z) = \frac{e^{ikz}e^{\frac{i\pi}{\lambda z}(x^2+y^2)}}{i\lambda z}\int\int_{S_A} dx'dy' u(x',y',0)e^{\frac{i\pi}{\lambda z}(x'^2+y'^2)}e^{-i\frac{2\pi}{\lambda z}(xx'+yy')} \tag{1.45}$$

Furthermore, it is recommended to observe that the Fresnel diffraction is commensurate to the input field $[u(x',y',0)]$ 2D Fourier transform multiplied by a quadratic phase factor. An example of a small quadratic phase factor due to (z) for distances and the aperture sizes is shown below

$$\frac{\pi(x'^2+y'^2)_{max}}{\lambda} \ll z \tag{1.46}$$

The Fresnel diffraction relation can be rewritten as

$$u(x,y,z) = \frac{e^{ikz}e^{\frac{i\pi}{\lambda z}(x^2+y^2)}}{i\lambda z}\int\int_{S_A} dx'dy'u(x',y',0)exp\left[\frac{-i2\pi}{\lambda z}(xx'+yy')\right] \tag{1.47}$$

This relation is known as the Fraunhofer diffraction formula, and it is discernible that the input and output, in this case, are correlated due to a Fourier transform relationship [61].

1.10 Outline of Thesis

The rest of this thesis is organized in the following way:

In chapter 2, I introduce the basic fundamental principle of liquid crystal.

In Chapter 3, I present an overview of the workings of the spatial light modulator and the fabrication of the q-plates.

In Chapter 4, I present the experimental and theoretical results of the magic mirror effect using a spatial light modulator.

In Chapter 5, I present the results for quantum key distribution using orbital angular momentum mode of light via a vortex fibre using the BB84 protocol.

Finally, in Chapter 6, I conclude the works presented in my thesis and also discuss outlooks for future works .

Chapter 2

Liquid crystals

This chapter includes a background regarding liquid crystals features such as electrical and magnetic effects and their deformation. The information presented here will help understand chapter 4.

2.1 Introduction to Liquid Crystals (LC)

Before the discovery of the liquid crystal (LC) phase by Reinitzer [28], the common perception was that there were only three states of matter in nature: solid, liquid, and gas, as shown schematically in Figure 2.1. This simple classification of the states of matter is based on the degree of the order in their molecular or atomic arrangements. The solid state is generally the most dense and has the highest degree of order; the molecules are almost fixed at specific locations (referred to as lattice sites) within the crystalline structure, with no translational motion. In solids, the intermolecular attraction forces are strong enough to balance the repulsive forces from the electron clouds (and nuclei) of the adjacent atoms or molecules. Therefore, the molecules or atoms energetically prefer to remain in fixed locations, and large external forces are required to disturb or deform the solid structure. In liquids, the molecules are not restricted to specific locations or orientation, and there-

fore the degree of order of molecular arrangements in liquids is less than that in solids. In liquids, the inter-molecular attractive forces are weaker than the repulsive forces, and therefore the molecules have some level of freedom to diffuse, leading to collisions and changes in their orientations. Due to the weak attractive intermolecular forces, liquids are easily deformed and reshaped with the application of relatively small external forces. The gas phase is the least dense state with the lowest degree of order in their molecular arrangements.

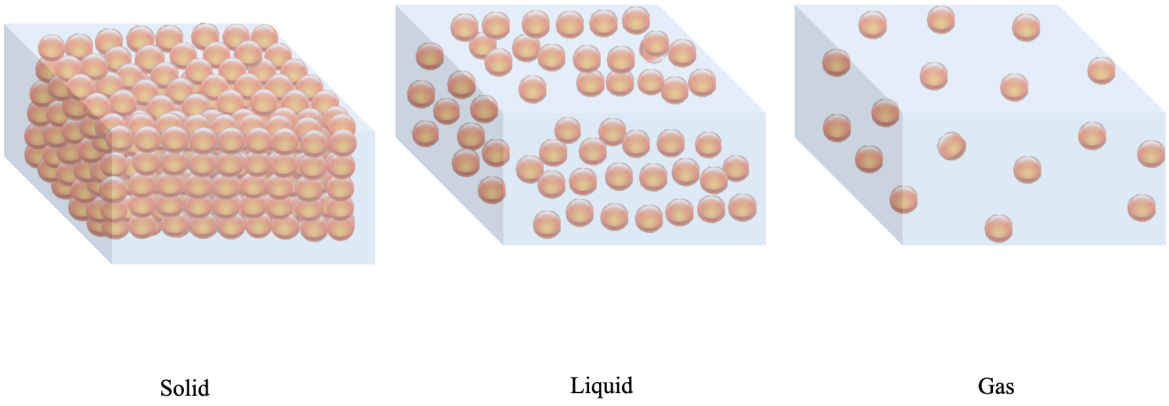

Figure 2.1: Schematic illustration of the degree of molecular arrangements in solid, liquid and gas states.

In gases, repulsive forces between the constituent molecules are much larger than attractive forces. Therefore, the gas molecules move freely to maximize their relative distance from each other, uniformly filling the storage container. The average intermolecular distance in liquids does not change; while in the gas phase, it is mainly the number of molecules and the size of container [28].

The LC state of matter lies between isotropic liquids and the crystalline solids, as shown schematically in Figure 2.2. The physical properties of LCs are intermediate to those of the solid and liquid phases. In addition to LC, this phase is also referred to as the

intermediate phase or mesophase. LCs share some properties similar to those of liquids, including coalescence of droplets, fluidity, and the inability to withstand shear forces. Also, LCs possess crystal-like properties, such as anisotropy in their optical, electrical, and magnetic behaviours. LCs have found many applications in photonics [6], bio-sensing [68], and display devices[120]. The main classes of LCs are lyotropic and thermotropic. Thermotropic LCs are obtained by melting a crystalline solid within specific temperature and pressure ranges. Lyotropic LCs, on the other hand, are based on colloidal solutions and polymers, and are formed under specific concentration and temperature ranges. LCs have also been found to occur naturally in a number of organic compounds.

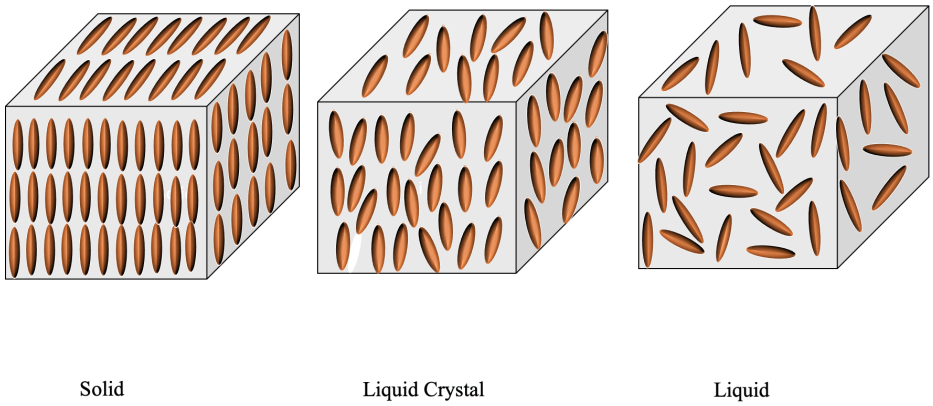

Figure 2.2: An illustration of the fundamental structural differences between crystalline solid, liquid crystal and isotropic liquid. Solid crystal has positional order and orientational order. Moreover, liquid crystal has orientational order but no positional order. On the other hand, isotropic liquid has no positional order nor orientational order.

The LC molecules usually have an extended flat segment with benzene rings. Such molecules commonly contain double bonds in an elongated direction. The molecular structure of the para-azoxyanisole (PAA) and the p-methoxy benzilidene p-n-butylaniline (MBBA), for example, are shown in Figure 2.3.

The LC molecules have strong electric dipoles and can easily be polarized [108, 79], which makes the thermotropic LCs suitable for application in the electro-optic display and sensing devices. On other hand, the lyotropic LCs have been found in many biological

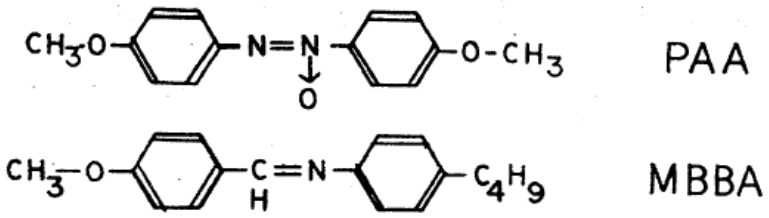

Figure 2.3: The structure of molecular para-azoxyanisole (PAA) and p-methoxy benzilidene p-n-butylaniline (MBBA) [79].

applications. Based on the orientation and order, LCs can be classified into three main classes: nematic, smectic, chiral nematic (cholesteric) LCs. Detailed descriptions of these three classes of LCs are presented in Section 2.8.

2.2 History of LC materials

During his experiments in 1990 to evaluate the purity of crystals by measuring their melting temperature, Friedrich Reinitzer saw that at a specific temperature, solid materials transform into a cloudy liquid, and then into a clear liquid [92]. This observation suggests that the cloudy liquid was partially ordered and that the transparent phase was the prevalent disordered state of liquids. After this discovery, the cloudy liquid state, which is a phase between solid and liquid, was recognized as a new state of matter and was named LC. The key features of LC materials are: (1) the existence of two melting points and (2) the ability to react to a polarized light. After this discovery, Lehmann continued to study LCs employing crystallography and microscopy techniques [92]. During themid-1990s, Orsay's studies enhanced the understanding of LCs [92]. Gilles de Gennes developed the mathematical models to explain how molecules under specific conditions can form ordered states[92]. For his extensive studies in developing mathematical models in the field of LC, Pierre Gilles de Gennes received the Nobel Prize in Physics from the Royal Swedish Academy in 1991.

In 1960s, the RCA laboratories significantly improved the manufacturing technologies

for flat panel displays based on LCs and proved that the LCs can function at a broad range of temperatures, including at room temperature[92]. This development led to a wide use of small LC displays (LCDs) in electronic displays and common household items, such as watches. The applications of LCs are not limited only to display devices, however. Their high sensitivities to spontaneous electrical polarization under mechanical stress make them suitable in sensing applications as well; today, LCs are used to fabricate sensors, actuators, and energy harvesters [92, 30].

2.3 The Physical Properties of Liquid Crystals

In this section we explain the physical properties of liquid crystals such as anisotropy, dielectric properties, and the effect of magnetic field.

2.3.1 Anisotropy

LCs have some common characteristics with liquids, including fluidity. Unlike liquids, however, their molecular orientations play an important role in determining the properties of LCs. The molecules in liquids are in random motions producing equal phases in all directions. That is, a liquid is considered to be an isotropic medium where its physical properties are the same in all directions. In isotropic media, any property measured in one direction will have the same value when measured in any other direction. For instance, the propagation loss of sound waves in liquid is independent of its propagation direction in liquid. Similarly, the isotropic phase refers to the case where the phase is the same in all directions. LC, however, molecules spend more time pointing in a specific direction than in other directions at a given point. As a longitudinal wave, sound travels along the direction of the LCs where the molecules lie along the direction of the propagation. In contrast, light, which is a transverse wave, travels in directions other than the direction

where the molecules are dominantly oriented. In other words, there exist an angle between the propagation direction of light and the molecular orientation in the LCs. Therefore, the response of the LC molecules to a sound wave travelling in the LC will depend on the propagation direction of the sound waves. For instance, the intensity loss of a sound wave traveling along the director is larger compared to the sound wave traveling in any other direction. This feature indicates the anisotropic properties of the LCs, which is the most important property shared between solids and LCs. According to Otto Lehmann, the interaction of light, as an EM wave, with the LC material is anisotropic, and it strongly depends on its propagation direction and the LC director [28]. The anisotropy in LCs is also evident in the phase response of an LC to an applied external field, which is a function of the angle between the applied field and the director of the LC.

2.3.2 Dielectric Properties

A dielectric material is an insulator which can be polarized by an external electrical field. When an electric field is applied to a dielectric material, the positive and negative charges will displace, which resulting in the formation of a local electric dipole moment. The constitutive relation of Maxwell's equations related to the displacement electric field $\vec{D}$ is given by

$$\vec{D} = \varepsilon_r \, \varepsilon_o \vec{E} + \vec{P}, \tag{2.1}$$

where $\vec{P}$ is the polarization density, ε_r is the material permittivity, and ε_o is free space permittivity. Permittivity is a measure of a material's ability to become polarized in the presence of an external electric field. The internal polarization partially cancels out the electric field inside the material. In LCs composed of non-polar molecules, the induced polarization consists of electronic and ionic polarization components. In LCs with polar molecules, the existing permanent dipoles tend to orient themselves parallel to the applied external field giving rise to an additional polarization component [92, 101].

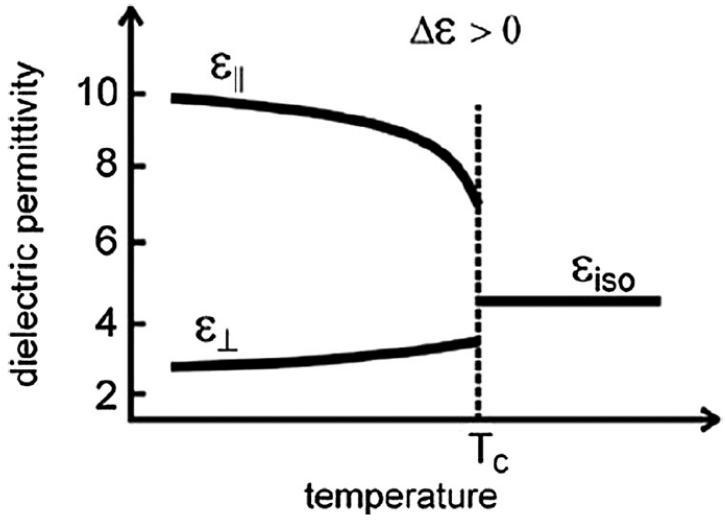

Figure 2.4: The dielectric permittivities of liquid crystals are dependent on temperature. ε_{iso} represents permittivity of anisotropic liquid and T_c represents the clearing temperature. Due to the temperature dependency, and due to anisotropy, dielectric permittivity will also depend on LC orientation as shown in the figure. Component one is parallel measured and other is perpendicular [92].

The constitutive relation of Maxwell's equations related to the displacement electric field D is given by

In the case of the uniaxial LCs with the director n parallel to the z-axis, the polarization vector will have two components: one is parallel ($\varepsilon_{\parallel} = \varepsilon_{zz}$) and the other perpendicular ($\varepsilon_{\perp} = (\varepsilon_{xx} + \varepsilon_{yy})/2$) to the director. This leads to a dielectric anisotropy given by $\Delta\varepsilon = \varepsilon_{\parallel} - \varepsilon_{\perp}$, which could exhibit positive or negative values. The dielectric permittivity for a typical LC depends on the temperature, as shown in Figure 2.4. In LCs composed of polar molecules, the polarization due to the permanent dipoles of the molecules can be expressed by the Maier-Meier theory, which is given by [92]

$$\Delta\varepsilon \propto \left[\Delta\alpha + \frac{\mu^2 F}{2K_B T}\left(3\cos^2\beta - 1\right)\right], \tag{2.2}$$

where $\Delta\alpha$, μ and F represent the polarizability anisotropy, the molecular dipole moment, and the reaction field factor, respectively. T presents the temperature, K_B is the Boltzmann

constant, and β is the angle between the molecular dipole moment μ and the molecular axis. LCs with a larger anisotropy are commercially desirable as they require a smaller field to manipulate it [92].

The LC sample will behave like a large electric dipole when an electric field is applied along its molecular axis. This is because the electric dipoles the long axis of the molecules add up and reinforce each other. For instance, for a collection of rod-like molecules pointing evenly up (positively charged end) and down (negatively charged end), the positive charge at the top and the negative charge at the bottom of the LC sample will act as a large electric dipole. In general, in LCs, the permanent molecular electric dipole moment or the induced electric dipole moment may align along the director or perpendicular to the director. This implies that the electric polarization along the director is different from that polarization perpendicular to the director. The strength of the electric polarization depends on the relative strength of the electric dipole along or perpendicular to the molecule's long axis. In an LC sample with a locked director direction, when an external electric field is applied perpendicular to the molecular axis, the electric dipoles perpendicular to the long axis of the molecules will add up to produce an electric polarization parallel to the external field. In the case where the direction of the director is not locked, when an LC sample is placed in an external electric field, the director will realign such that the net dipole moment vector will be positioned parallel to the external electric field. Therefore, if the dipole moment is parallel (perpendicular) to the director, the molecules will rotate such that the director will become parallel (perpendicular) to the applied external electric field. The greater the difference between the parallel and perpendicular polarization components, the smaller the electric field required to orient the LC. In general, the polarization increases with increasing applied external electric field. However, the ratio of polarization to applied field is usually constant and is commonly referred to as the electric susceptibility. In other words, the electric susceptibility is a measure of how easily the material is polarized by an external electric field [92].

2.3.3 Effect of Magnetic Field

The negative electron charge orbiting around the nucleus of an atom (in the semi-classical model) acts like a tiny loop of moving charge. In some atoms the sum of the nucleus spin, the electron spin, and the orbital spin result in a permanent magnet. Such atoms behave like permanent magnetic dipoles. These atoms within the LC molecules are not usually magnetic. However, when an external electric field or a magnetic field is applied to these LC molecules, some of the charges within the LC molecules start behaving like tiny loops of moving charges. Once this occurs, the molecules have an induced magnetic dipole, and this dipole tends to orient itself along the magnetic field. The magnetic dipole moments in LC molecules are different from one molecule to the next molecule. The magnetic dipole will be either parallel or perpendicular to long axis. Depending on the orientation of the magnetic dipoles, the LC molecules will be forced to align along the magnetic field, either parallel or perpendicular to the long axis.

The amount of magnetization difference depends on how magnetic field is applied. For instance, the magnetic field applied parallel to the molecular axis induces a certain amount of magnetization than the magnetic field applied perpendicular to the director. This is simply another example of LC anisotropy, which originates from the various magnetic dipoles induced along or perpendicular to the molecule's long axis. If no other force restricts the director, the LC will tend to orient such that the higher magnetization (corresponding to the larger molecular magnetic dipole) is parallel to the applied field. The director can change fields if it is not locked in place relative to its container. This leads to the complete alignment of the director for magnetic fields of comparatively low strength. The higher the magnetization anisotropy in the LC, the lower the magnetic field required to align the director. The magnetic susceptibilities for LC director in either a parallel or perpendicular direction. Similarly, a higher magnetic field strength achieves a higher magnetization [28].

Magnetic susceptibility is the ratio of the magnetization induced within the LC due to

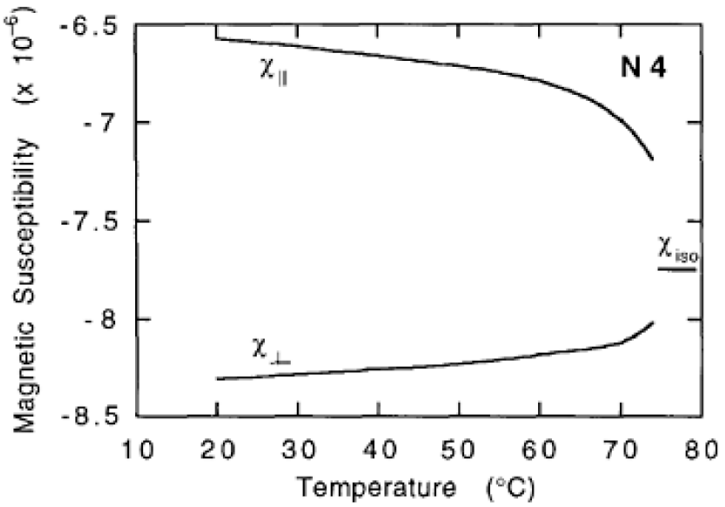

Figure 2.5: The image represents the magnetic susceptibility for nematic LC molecules and isotropic phase. It is showing that one component is parallelly measured and the other component is perpendicularly [30].

the applied magnetic field and depends on the temperature and how the order parameter (defined in Section 2.6 below) changes with temperature. This is illustrated in Figure 2.5. It can be inferred from this graph that the magnetic susceptibility of LC is negative and is on the order of 106 [28, 30].

2.4 Deformation of Liquid Crystals

Although the director in the LC is often is free to point in any direction, there are examples where this is not the case. When one places a material in contact with a LC sample, the director will be forced to point in a specific direction. For instance, if a glass surface is placed near the LC molecules, the glass will force the LC molecules to orient parallel to the glass surface. The director will remain parallel to the surface, even when an electric or magnetic field is applied. However, the LC molecules away from the surface will respond to the electric or magnetic field. The effects of the surface and the electric or magnetic field compete to induce a deformation in the LC. LCs deform by applying an external field,

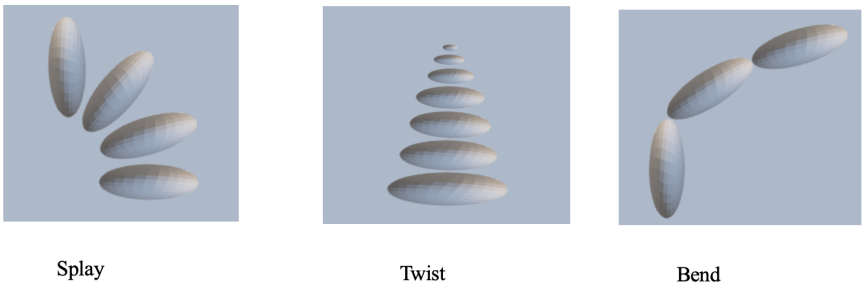

Figure 2.6: Three basic types of deformations in LCs.

with the director parallel to the surface near the surface and perpendicular to the surface far from the surface. In a deformed LC, the director changes its direction from one point to another point. In contrast, in an undeformed LC, the director points in the same direction throughout the sample.

There are three basic types of LC deformations: splay, twist, and bend, as demonstrated schematically in Figure 2.6. In these basic deformations, the orientation of the director does not change moving into or out of the page, as schematically shown in Figure 2.6. The deformation of LC needs energy which is referred to as the free energy F_v. The free energy of the non-chiral nematic LC per unit volume can be calculated according to the equation given below[29]

$$F_v = \frac{1}{2}K_1 \left|\vec{\nabla}\cdot\vec{n}\right|^2 + \frac{1}{2}K_2 \left|\vec{n}(\vec{\nabla}\times\vec{n})\right|^2 + \frac{1}{2}K_3 \left|\vec{n}\times(\vec{\nabla}\times\vec{n})\right|^2, \tag{2.3}$$

where K_1, K_2 and K_3 are the elastic constants of splay, twist, and bend respectively [92, 29].

2.5 Freedericksz Transition

In an undeformed LC, the director points in the same direction throughout the LC, while in a deformed LC, the director changes from one point to another. This deformation does not happen gradually as the strength of the field is increased, however; for field strengths below a specific value, the LC remains undeformed, a homogeneous mixture. As the strength of the applied field exceeds this threshold, the deformation starts. The transition from an undeformed structure to a deformed structure due to the applied field is called the Freedericksz transition.

The anisotropy of the LC sample in orienting the directors is a measure of the response to an external electric or magnetic field; the greater the LC anisotropy, the smaller the value of the threshold field required for transition. In contrast, a greater value for the threshold field (smaller LC anisotropy), the greater the force required to deform the LC. The LC varies the magnitude of the force needed to deform it. Since the deformation occurs throughout the thickness of the LC film, the thicker the film, the smaller the deformation. The value of the threshold for the field will be smaller in thicker samples due to the same alignment of the director in the center of the film which means smaller deformation in thicker films.

When there is no electric or magnetic field applied, the director of LC is in an undeformed configuration, and is oriented perpendicular to the surface. Figure 2.7 shows the case where there is no electric or magnetic field applied and is called homeotropic texture. It also and shows a case where an electric or magnetic field is applied parallel to the glass surfaces, forcing the LC molecules in the middle to orient parallel to the surfaces. This type of deformation is called bend. The twist deformation is a configuration that occurs when a field has been applied into or out of the page. The glass surfaces are treated to produce parallel alignment of the director. The molecules of LC in the middle of the film tend to orient in or out of the page with the field. This type of deformation state is called

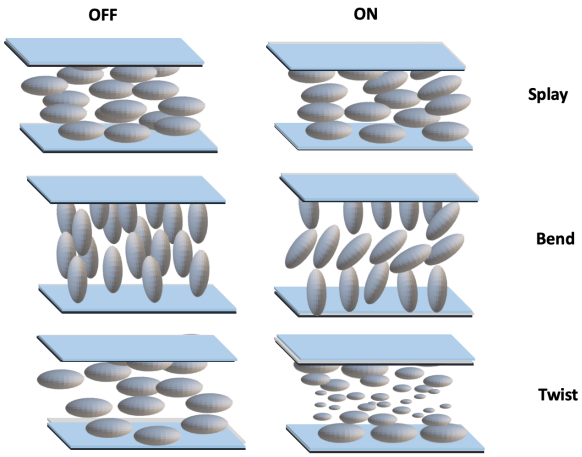

Figure 2.7: The basic types of deformations of liquid crystal molecules. The left side exhibits the absence of applying an electric or a magnetic field and right side shows the molecules at the point they are exposed to an electric or a magnetic field.

twist deformation, as schematically shown in Figure 2.7. The electric field threshold is approximately 400 V/cm, and the threshold of the magnetic field is approximately 0.2 Tesla for a 25 micron thick film [28].

When no electric or magnetic field is applied, the director of the LC is in an undeformed configuration, and is oriented perpendicular to the surface; this homeotrophic texture is depicted in the left column of Figure 2.7. The right column of Figure 2.7 shows the case where an electric or magnetic field is applied, causing deformation. In the bend deformation, a field applied parallel to the glass surface forces the LC molecules in the middle to orient parallel to the surfaces. The twist deformation occurs when a field is applied into or out of the page. The glass surfaces are treated to produce parallel alignment of the director. The molecules of LC in the middle of the film tend to orient in or out of the page with the field. For a 25 micron thick film, the thresholds for the electric and magnetic fields are approximately 400 V/cm and 0.2 Tesla, respectively.

LCs are frequently used in thin layers sandwiched between two confining layers of glass. The interior LC layer is transparent and an electrode is placed on the internal surface which is electrically conductive. To set the angle between the LC molecule director and some

reference vector, an external control is required; otherwise, the LC director may point at any angle. Placing the polymer coating between the electrode and LC material can help control the director. Using a piece of cloth to rub the polymer chains coating will slightly align them, as the LC molecules are forced alter. Although there are numerous ways to achieve alignment techniques, the interaction between the surface and the LC molecules is essential to align the LC. There are three alignment technique: rubbing technique, the oblique evaporation technique, and physio-chemical technique.

The first one is rubbing technique. Mechanical surface rubbing is the oldest technique used to create anisotropy of the physical characteristics of the surface. It is a direct contact with the substrate surface, which is achieved by rubbing the surface to achieve an alignment of the LC molecules at the surface. During the rubbing technique, the glass substrate surface is rubbed unidirectionally using a particular type of cloth, or by hand.

Another technique is called the oblique evaporative method which is an indirect technique in which there is no direct mechanical contact with the sample surface. In this technique, the sample is blasted with an evaporation beam of oxides, such as SiO or GeO, at a certain incident angle. The evaporation parameters which control the surface structure include temperature, pressure, and the incident angle.

The last technique is the physico-chemical method. In this method, LC alignment can be obtained using surface coupling agents, which are either mixed with the LC material or deposited on top of the glass substrate. The surface coupling agent has hydrophilic and hydrophobic components and the main mechanisms involved are steric forces and polar interactions. Based on their specific properties and the agents' surface density, they have homeotropic or homogeneous (planar) alignment when deposited on the inner substrate surface. In homeotropic alignment, the molecules are aligned perpendicular to the substrates, while in the planar arrangement, molecules are parallel with the substrate [92].

2.6 Order Parameter

A second rank symmetric tensor, called the order parameter, is used to define a nematic liquid crystal's orientation. However, a scalar order parameter is used to describe the orientation of uniaxial nematic liquid crystals, including of the mesophase. This scalar parameter given by

$$S = \langle P_2(\cos\theta)\rangle = \langle\left(\frac{3\cos^2\theta - 1}{2}\right)\rangle, \tag{2.4}$$

where P_2 is the second order Legendre polynomial, θ is the angle between the molecular axis and the director, and $\langle\cdot\rangle$ indicates the temporal and spatial average (Figure 2.8) [92].

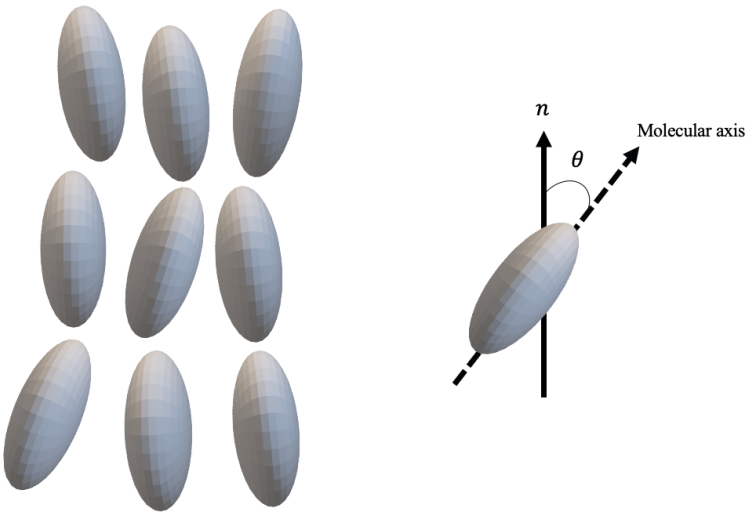

Figure 2.8: The figure demonstrates the relationship between the director n and the molecular axis, which is the angle between them identified as θ for liquid crystal.

The equation shows that a high ordered LC is achieved by decreasing the average angle from the director. An order parameter of 1, when θ is equal to zero, indicates a high degree of organizational order for all molecules. Figure 2.9 shows that with increasing temperature, the order parameter decreases, eventually goes to zero at the clearing temperature during the transition to the isotropic phase. Order parameter of most LCs range between 0.3 and 0.9 [86]; in an LC test subject, if the scalar order parameter value is zero, the liquid will

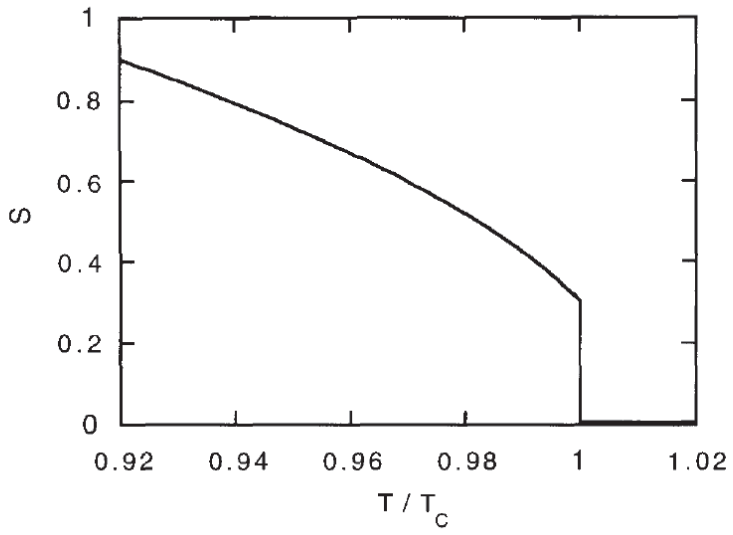

Figure 2.9: The image shows the relationship between order parameters and temperature. As the value of order parameter increasing S decreases to a sudden fall in order parameter to the point T/T_c reaches zero, which leads to the transition towards an isotropic phase [30].

.

be isotropic and if the value is one, the molecules will be impeccably arranged [92].

Under the assumption the nematic or cholesteric liquid crystal molecules are having rodlike in shape, then the unit vector $V^{(i)}$ can be introduced along an axis. The unit vector describes the orientation of the ith molecules along the axis. As noted above, the order parameter is usually described as a second-order rank tensor given by

$$S_{\alpha\beta}(r) = \frac{1}{N}\sum_{i}\left(v_{\alpha}^{i}v_{\beta}^{i} - \frac{1}{3}\delta_{\alpha\beta}\right), \tag{2.5}$$

where the sum is over all the N molecules in a macroscopic volume contained within a radius r, and $\delta_{\alpha\beta}$ is the Kronecker delta. Here coefficients $\alpha\beta$ represents the matrix component/element which is associated with S matrix (second rank tensor). The V_{α} is a set of laboratory fixed axes. S has five independent components and is the form of an asymmetric traceless second-order tensor. Once the molecules reach random orientation

at the isotropic state, the second order tensor $S_{\alpha\beta}$ vanishes.

Describing the nonlinear rigid molecules order parameter requires presenting a Cartesian coordinate system that has x', y', and z' as fixed axes in the molecules. Then, the order parameter for a tensor in an uniaxial LC is given by

$$S_{\alpha'\beta'}(r) = \langle \cos\theta_{\alpha'} \cos\theta_{\beta'} - \frac{1}{3}\delta_{\alpha'\beta'} \rangle, \tag{2.6}$$

where θ is the angle between the molecule's axis α and the optic axis or the preferred direction, and the brackets are average over the molecules in a macroscopic volume. Equations (2.5) as well as, (2.6) has closely comparable molecules, whether they are linear or have well defined long axis. In real LC samples, different parts of an individual molecule are described by different of values of $S_{\alpha\beta}$ tensors because that the order of the molecules is flexible. The order parameter will be described by a macroscopic property such as anisotropic magnetic susceptibility, i.e.,

$$Q_{\alpha\beta} = \chi_{\alpha\beta} - \frac{1}{3}\delta_{\alpha\beta}\chi_{\gamma\gamma}, \tag{2.7}$$

where $Q_{\alpha\beta}$ take the form of an asymmetric traceless second-order tensor, and $\chi_{\alpha\beta}$ are the tensor elements of the magnetic susceptibility. Due to the small interaction between molecules, the magnetic susceptibility can be approximated by the sum of the magnetic susceptibilities of individual molecules. With this approximation, the interaction term is omitted and $Q_{\alpha\beta}$ is directly related to $\chi_{\alpha\beta}$. Let's assume that the principal susceptibilities of a molecule are given by $\chi_1^{(0)}$, $\chi_2^{(0)}$, $\chi_3^{(0)}$, and selected fix axes for the molecules x',y', and z' to coincide with the principal axes of the susceptibility. Then, it easy to show for uniaxial LCs [108]

$$Q_{xx} = Q_{yy} = 2N\left((S_{y'y'} + S_{z'z'})\,\chi_1^{(0)} + (S_{z'z'} + S_{x'x'})\,\chi_2^{(0)} + (S_{x'x'} + S_{y'y'})\,\chi_3^{(0)}\right), \quad (2.8)$$

$$Q_{zz} = N\left(\chi_{x'x'}X_1^{(0)} + S_{y'y'}X_2^{(0)} + S_{z'z'}, X_3^{(0)}\right), \quad (2.9)$$

where N is the number of LC molecules per unit volume. In the presence of an axial symmetry, the susceptibility is given by [108]

$$Q_{\alpha\beta} = N_{X_a^{(0)}}\,S_{\alpha\beta}, \quad (2.10)$$

where $X_a^{(0)}$ is defined as the anisotropy in the susceptibility, for example, $X_a^{(0)} = \chi_{\parallel}^{(0)} - \chi_{\perp}^{(0)}$. $\chi_{\parallel}^{(0)}$ and $\chi_{\perp}^{(0)}$ correspond to the susceptibilities along and perpendicular to the axis, respectively.

2.7 Applications of Liquid Crystals in Technology

Liquid crystal technology has been widely adopted; devices utilizing liquid crystal properties, mostly in the form of digital displays, are very popular. These devices use advanced techniques that control light to produce images with very high resolution and in many colours. Liquid crystal display technology has contributed to the growth of mobile computing and the worldwide spread of smartphones[92]. There are several other applications of liquid crystal technology. Liquid crystals can be processed into sheets of plastic, which change colour when absorbing infrared radiation within their sensitivity range of 25 to 32 C[92]. Liquid crystal technology is also used to develop chemical sensors by placing receptors that can align a thin liquid crystal film within the film. If a target molecule is present, the receptor modifies the alignment of the liquid crystal film, and the alignment alteration can be optically detected. Using this method, a number of different applications, including

DNA sequencing, can be extended. Tunable LC filters can allow just a specific wavelength of light to pass through, excluding all other wavelengths. These filters are mostly utilized in multispectral and hyperspectral imagers; due to their lightweight and tunable nature, they are a good option for spaceborne imagers and scientific imaging cameras. In addition, smart films made of LCs dispersed in polymers can alter light transmission from a transparent state to a blurred state by applying a voltage[92].

LCs have also been found in useful in building material in energy-saving applications. The LCs' thermal property can be utilized to make a plastic strip thermometer, where the temperature and colour of the LC changes with temperature. These devices not only measure the temperature, but also show the migration of heat in a system. Large-footprint radiation discoveries utilize polymer-dispersed liquid crystals that act as a light valve. Liquid crystal systems have been suggested for the development of foveated images that utilize a spatial light modulator to give aberration rectification in a small area of the image [92].

2.8 Liquid Crystal Phases

Based on their molecular order, liquid crystals (LCs) can be divided into three main classes: nematic, smectic, and chiral nematic (cholesteric) LCs, as shown schematically in Figure 2.10. The nematic phase is the simplest LC phase. The name nematic comes from a Greek word which means thread. Nematic LCs have various applications such as in LC displays [120], image processing devices [42], and optical modulators [63].

The molecules in nematic LCs have their center of mass positions distributed relatively randomly, while they have a high degree of order in their molecular orientations, as shown schematically in Figure 2.10 A. Since the molecules in nematic LCs have no long-range positional order, no distinct Bragg peak can be found in their X-ray diffraction patterns. Most nematic crystals have a single long axis and are elliptical in shape. The molecules

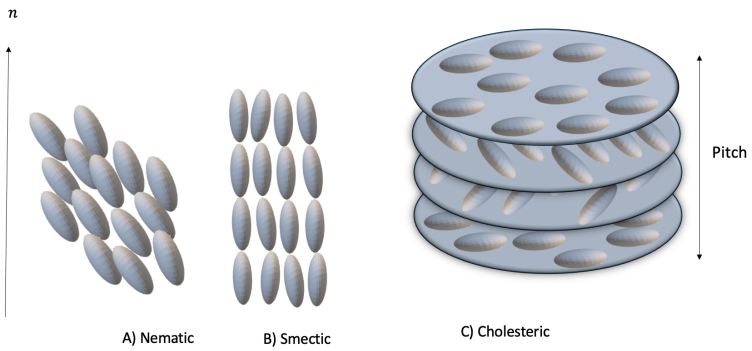

Figure 2.10: Illustration of Nematic, Smectic, and Cholesteric phases of LCs. A) Nematic, is a random position yet has an orientational order.B) Smectic, has position and has orientational order in layer. C) Cholesteric has position and has orientational in layer with respect to molecules in an accumulated vertical fashion (from top to bottom).

of nematic LCs self-align to achieve a long-range directional order with their long axes roughly parallel. This preferred direction is often described in terms of a unit vector n referred to as the director. This preferred alignment axis determines the phase symmetry axis and the nematic axis.

In contrast to the nematic phase, the smectic phase molecules are arranged in planes or layers. The name smectic comes from a Greek word meaning soap-like. The smectic phase forms at a lower temperature than the nematic phase. Due to the well-defined layer structure of the smectic LCs (Figure 2.10) B, their inter-layer spacing can be measured by X-ray diffraction analysis. In 1969 Sackmann and Demus categorized smectic LCs into different classes based on their range of the positional order within the layers. Smectic LCs were divided into smectic A and smectic C which have a short-range and long-range order, respectively, as shown schematically in Figure 2.11. In smectic A (short-range), the direction of the long axes are perpendicular to the layering, while in smectic C (long-range), the direction of the long axes are not perpendicular to the layering. There are several smectic LC phases in which the molecules form a layered structure (B, I, F). For instance, the molecules of smectic B form a layered structure, however, the molecules inside the layers are rotationally fixed and are not able to rotate around their axes [35, 88].

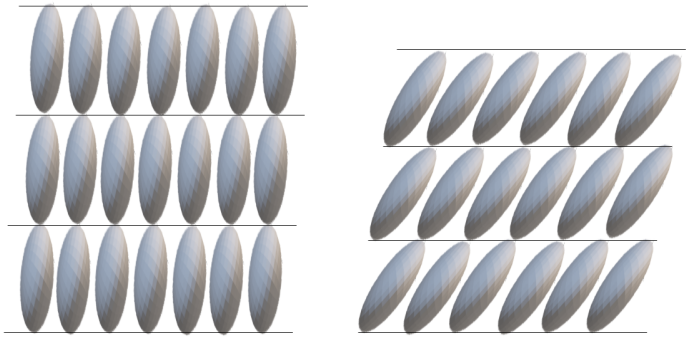

Figure 2.11: Schematic diagrams for smectic A and smectic C liquid crystal phases. A is perpendicular to axis and C is not in comparison to the axis in each smectic.

A chiral nematic (cholesteric) LC phase is formed when a chiral molecule is dissolved in a nematic LC. This effectively twists the nematic phase molecules into a helical phase with the directors forming a helical pattern [35, 88]. The cholesteric phase and the nematic phase both have long- range orientational order and they both lack a long-range positional order in their molecules. However, the cholesteric phase differs from the nematic phase in that the director varies in the direction across the medium. As the molecules in a cholesteric phase twist, the director and the Fresnel ellipsoid are seen to rotate. In addition, the long axes of the molecules align along a single preferred direction perpendicular to the twist axis. The helical structure of cholesteric LCs is characterized by two parameters: the direction of the rotation and its pitch. The pitch,p, is a measure of the distance taken for the director to rotate one full circle around the twist axis. The periodicity length L of the cholesteric LC is equal to one-half of the pitch $p/2$ since n and $-n$ are identical, as illustrated in Figure 2.10 C.

The pitch of cholesteric domain is of the several thousand angstroms order; therefore, it is equivalent to the visible light wavelength. The pitch is sensitive to external stimuli, including chemical composition and applied magnetic or electric fields. The cholesteric

LCs‘ molecules helical arrangement, is accountable for their characteristic colors upon light reflection and optical rotatory's high power [108, 35].

2.9 Light Scattering and Liquid Crystals

The light scattering property of LCs has various electro-optical applications. Caused by fluctuations in the director axis of the molecules upon interaction with applied EM waves, light scattering from LCs can be improved by adding polymer composites to the LC. The extent of the light scattering is determined by the cell thickness and geometry, boundary conditions, external field, and wavelength of the scattered light. Thus light scattering in LCs can effectively be controlled by applying an external electric field to modify the refractive index by re-orienting the LC molecules.

The refractive index of LCs can be measured by placing it in a thin wedge cell with a thin glass or in a prism-shaped cell. The refractive index of LCs is then determined by measuring the minimum angle of deviation which passes through a prism. The minimum angle of deviation is calculated using Snell's law with paraxial approximation(i.e. α is small for thin prism). The angular displacement is calculated using Snell's law

$$\theta_d = (n-1)\alpha, \tag{2.11}$$

where θ_d is the deviation produced by the insertion of the prism. The refractive index of LCs can also be measured using an Abbe refractometer, wherein the refractometer measures the total internal reflection [92]. The Rayleigh scattering from small LC particles has extensively been studied using a monochromatic plane light wave. Three factors affect the light scattering from a particle: 1) the particle's size relative to the wavelength of the incident light, 2) the refractive index of the particle relative to the refractive index of the nearby medium, and 3) the shape of the particle. If the particle's radius is less than the

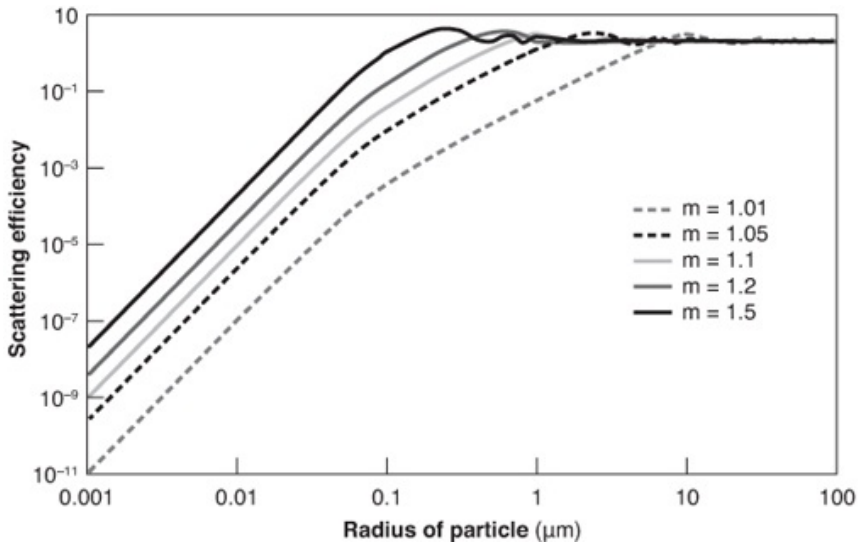

Figure 2.12: Shows scattering efficacy q of different spherical particles related to refractive index m indicated as a function of their radii. The wavelength of incoming beams is 500 nm in vacuum. When the size of spherical particles radius is close to wavelength of incoming beam, the scattering efficacy will be low then gradually increases to the peak then it will oscillate around value of 2 [59].

wavelength of light by a factor of 10 or more, the incident light is scattered by all parts of the particle [59]. The scattering efficiency of the LC particles is proportional to the fourth power of the particle's radius.

Generally, the scattering efficiency of a particle increases with size; however, as the particle size increases, the light scattering mechanism becomes complicated. When the radius of the particles is more than $1/10^{\text{th}}$ of the wavelength of the incident light, the incident light is distorted by the particle's movement, and the scattering becomes too complex to analyze. This is schematically shown in Figure 2.12. As the particle size increases, the Rayleigh scattering becomes invalid, and more detailed theory is needed to explain the light scattering for LCs. In 1908, Gustav Mie proposed a method to study light scattering from spherical particles of any size. Figure 2.13 shows the transition from the Rayleigh scattering to Gustav Mie scattering as the particle size increases [59].

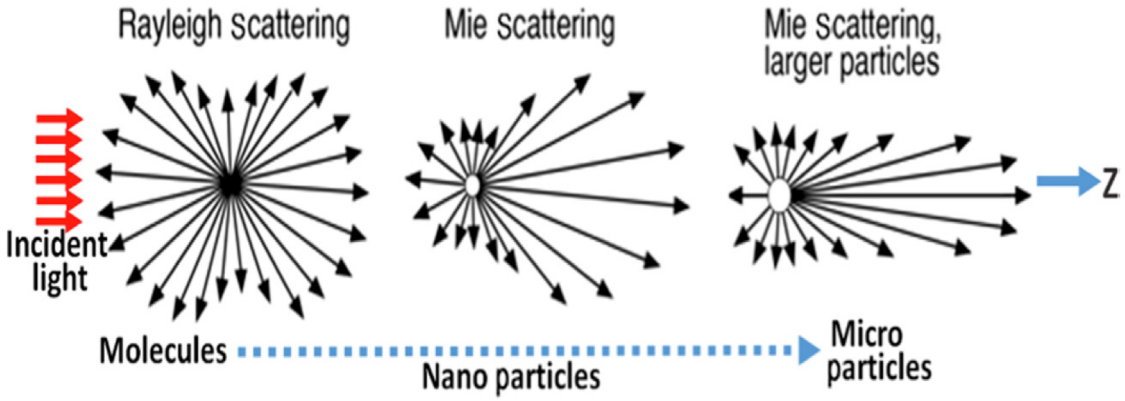

Figure 2.13: The image shows different type of scattering. Light scattering from LC particles with different sizes. Rayleigh scattering occurs when the size of particle is smaller than wavelength and Mie scattering occurs when the size of particle is bigger than wavelength. For larger particles, it shows more forward directed scattering due to the size of particle is much bigger than wavelength then the radiation will be asymmetric along the direction of propagation of electromagnetic field and it will have more radiation [84].

2.10 Polarization and Birefringence in Liquid Crystal Devices

An important feature of LC molecules is their ability to manipulate the polarization of an incoming light beam. Polarized light is an EM wave with mutually orthogonal oscillating electric and magnetic fields, which are perpendicular to the propagation direction. When two polarizing filters (polarizers) are arranged such that their planes of polarization are perpendicular to each other, light cannot pass through the second polarizing filter. However, if an LC is placed at a 45 degree angle with respect to the crossed polarizing filters, light partially passes through the second polarizing filter. This indicates that the LCs are effective in manipulating the polarization state of the EM waves. Indeed, LCs have a birefringence property due to their molecular anisotropy. When light passes through a birefringent material, it will split into two components referred to as the ordinary ray and the extraordinary ray, as shown in Figure 2.14. The ordinary ray corresponds to the polarization parallel to the director of the LC, while the extraordinary ray corresponds to the

light with its polarization direction perpendicular to the director. These two components have different refractive indices, and therefore travel with different (phase and group) velocities. Therefore, the two components will experience a phase shift as they travel through the LC sample. Due to this phase difference, when they recombine after passing through the LC sample, a change in the polarization state will occur.

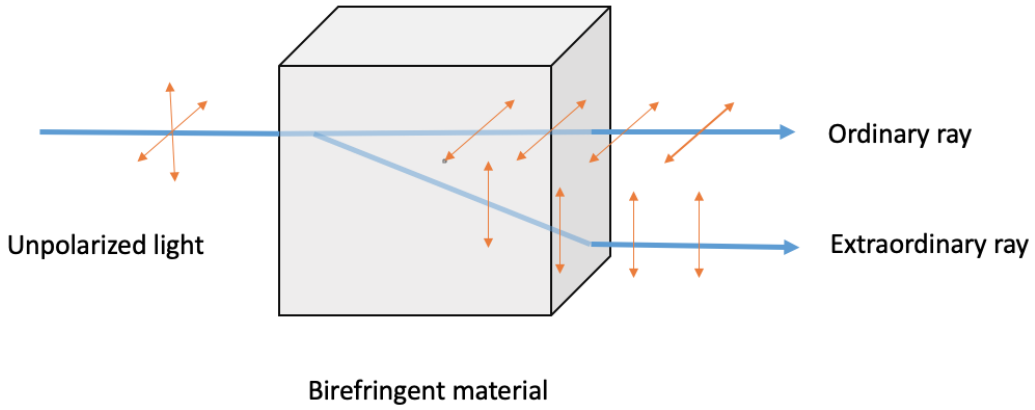

Figure 2.14: Schematic representation of the birefringence property of LCs. An unpolarized light splits into ordinary and extraordinary polarized rays upon passing through the LC sample.

Birefringence is defined by the difference between the ordinary refractive index n_o and the extraordinary refractive index n_e [79], i.e.,

$$\Delta n = n_e - n_o, \tag{2.12}$$

where $n_e = c/v_{\parallel}$ and $n_o = c/v_{\perp}$, where n_e is refractive index parallel to the director, n_o refractive index perpendicular to director, c is speed of light in vacuum, $v_{\perp}$and $v_{\parallel}$ are the velocity of light that travel perpendicular and parallel to the director, respectively [57].

2.11 Twisted Nematic Liquid Crystals : Optical Properties

A twisted nematic LC acts locally as a uniaxial crystal with anisotropic optical characteristics. The optical properties of the twisted nematic LCs are commonly studied by placing a thin layer of the LC material between two glass plates. In this setup, the twist axis of the LC material is perpendicular to the glass plates. Figure 2.15 shows a case where the

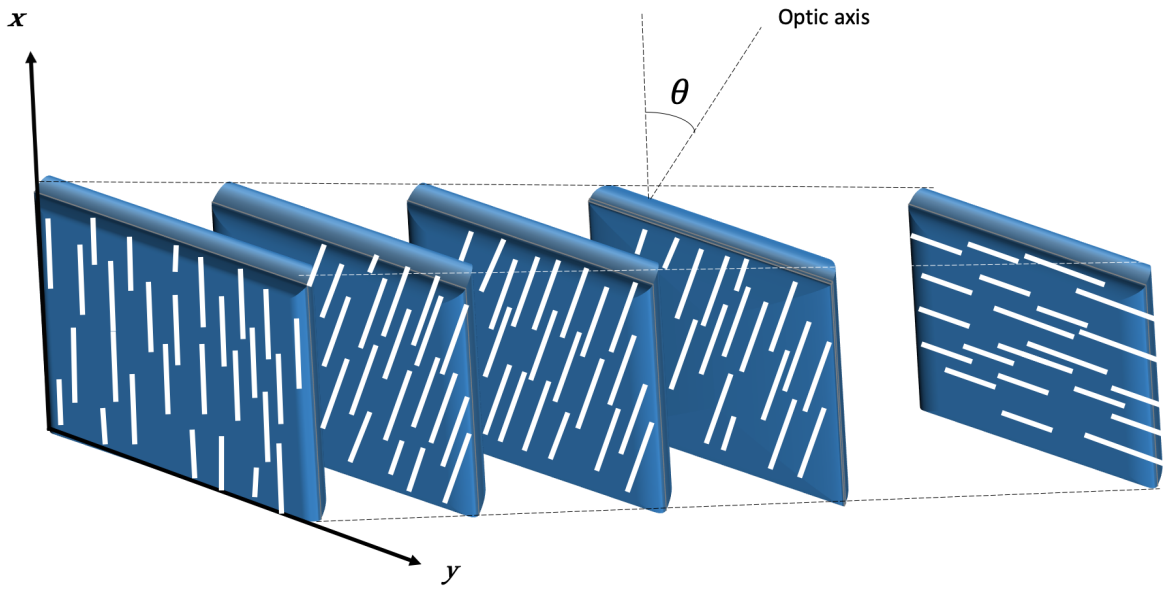

Figure 2.15: The twisted nematic LC cell drawing exemplifies molecules alignment in every plane, as the figure shows the 90-degree alignment shifts from left to right.

light traveling through a twisted nematic LC cell undergoes a twist angle of 90 degree. The incident wave at $z = 0$ is linearly polarized along the x-axis, and as the light propagates through the cell, it maintains its linear polarization. However, the polarization plane rotates in alignment with the twist of the molecular, which is given by

$$\theta = \alpha z, \tag{2.13}$$

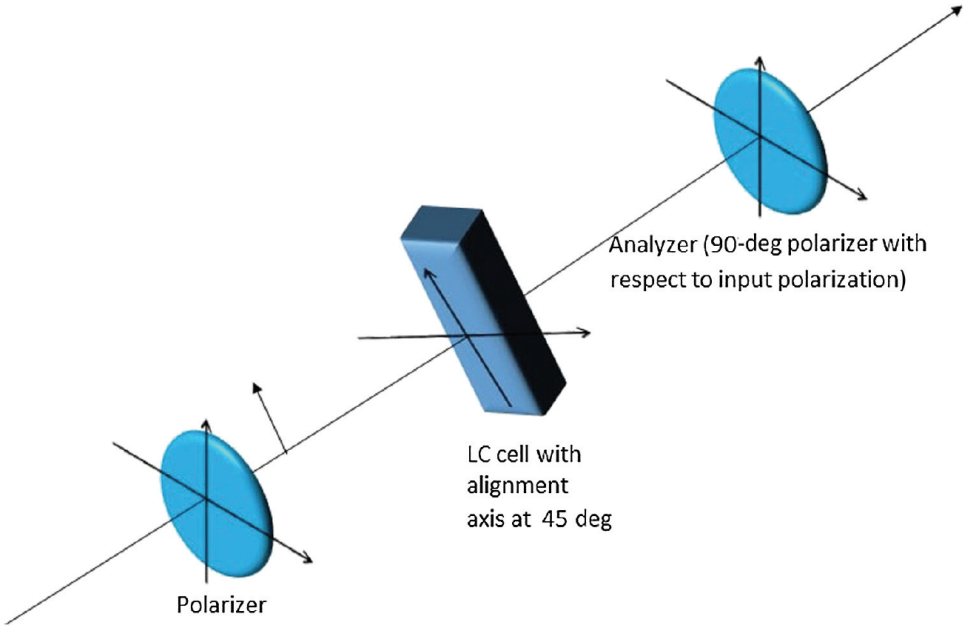

Figure 2.16: The liquid crystal cell once positioned between two polarizers in a perpendicular order. Opposing each other once they are aligned at the same point, the light will not pass [92].

where α is the twist coefficient. In this case, the liquid crystal cell works as a polarization rotator with a capacity of z. The optic axis is parallel to the x, y plane associated with making an angle θ in the direction of x. The phase-retardation coefficient is given by

$$\beta = (n_e - n_o)\, k_o, \tag{2.14}$$

where k_o is the beam wavenumber. For a positive birefringence LC, n_e is greater than n_o, this is because many cycles of phase-retardation are inserted before the optic axis rotates. To effectively measure polarization in a twisted nematic LC cell, two polarizers of known state are used: a polarizer and an analyzer. These polarizers are placed at a cross angle to each other as shown in Figure 2.16. When a light wave travels through an LC cell that is placed between the polarizer and an analyzer and aligned at an angle of 45 to the polarizer, the x and y polarization components in the outgoing light will experience a phase shift due to the difference in the optical path in the liquid crystal. The analyzer records the

intensity of the light passing through it as a function of the voltage applied to the thin layer of the LC cell.

As noted above, birefringence is measured as the difference in the indices of refraction of the polarization component. Birefringence in twisted nematic LCs can be measured using: Babinet-Soleil compensator, polarimetry, or beam modulation [47]. The Babinet-Soleil compensator measures birefringence by using a continuous variable wave-plate. A wave-plate or retarder is an optical device that changes the polarization of light by inducing a phase shift between two perpendicular polarizers. The Babinet-Soleil compensator consists of two birefringent crystal wedges, one of which is moveable, and the other is fixed to a compensator plate. Depending on the wedges' angle, the obtained phase retardance of the light that travels through the compensator ranges from one to several light wavelengths [56].

Polarimetry uses a polarizing beam splitter to split incident light into two orthogonal polarizations, called the x and y components. The polarization is measured by comparing the intensity of the two components, which are defined by

$$E_x = E_0 \cos\left(\omega t - \frac{\delta}{2}\right), \tag{2.15}$$

$$E_y = E_0 \sin\left(\omega t - \frac{\delta}{2}\right), \tag{2.16}$$

where δ is the angle between the components. The emerging beam intensity is measured using an optical sensor such as a photodiode or a power meter.

Beam modulation requires the use of a variable phase shifter, such as a pockels cell. The pockels cell is made of nonlinear optical crystals, such as KDP (KH_2PO_4) or ADP ($NH_4H_2PO_4$). The pockels cell induces a phase shift that is proportional to the applied voltage. In this process, phase modulation can be induced by passing a high DC voltage of a few of kilo-volts and a modulating signal of a lower voltage through the pockels cell.

The phase shift of the beam is given by the equation

$$\delta = \delta_0 - \delta_m \sin(\omega_m t), \tag{2.17}$$

where δ is called the total phase shift, δ_0 is the shift because of the DC voltage, and $\delta_m \sin(\omega_m t)$ is the shift because to the AC voltage with a frequency of $\omega_m/2$. After expanding this equation, the constant term is proportional to $\sin^2(\omega_m t)$ which oscillates at twice the modulation frequency. The linear part of the angular frequency ω_m, in terms of the intensity measurement I_m, is given by

$$I_m = -\frac{1}{2} I_0 (\delta_0 - \delta_m) \sin(\omega_m t). \tag{2.18}$$

The amplitude is measured using a lock-in amplifier. In the mid- 1980s, Wu, Efron, and Hess developed a relatively simple and versatile technique to measure the magnitude and wavelength dependence of the birefringence in LCs [92, 118].

The beam modulation technique overcomes some of the disadvantages of the other techniques, including the need for reference data, and difficulties in operating in the infrared spectral range. In this technique, measurement of the phase shift requires the voltage-dependent optical transmission of the cell in both perpendicular and parallel polarization directions to be measured and analyzed [92]. This technique is also used to tune the birefringence value in an LC cell by applying an external voltage to achieve arbitrary phase retardation in the range of 0 to 2π.

Chapter 3

Liquid Crystal Devices for Optical Phase Control

This chapter presents the principles of spatial light modulator (SLM) and q-plate and their fabrication.

3.1 Spatial Light Modulator(SLM)

Liquid crystals (LCs) have been successfully integrated into visual display devices, proving their commercial viability and standardizing them in our daily life applications. A popular example of LC based devices that is widely used in optic laboratory is the spatial light modulator (SLM). It has been considered a formidable tool based on LC technology for the alternation of both phase and polarization of the laser beam occurrences. SLM technology is continuously improving, not to mention, that new devices with improved functionality are being introduced at surprisingly growing rate. In comparison with it initiation, they were applied in optical computing, through time they have become popular in many research fields, for instance, wavefront correction, spatial beam shaping (SBS) [36, 53, 69].

3.2 Operation of Spatial Light Modulators

Spatial light modulators are devices that can be utilized to manipulate the phase and amplitude of an optical beam. These devices are divided in two basic types: refection or transmission. The SLM that we used in our research, can be used to modify the phase and the intensity of the incident light. This is presented in Figure 3.1, where a simple liquid crystal SLM is shown altering an incident beam [92].

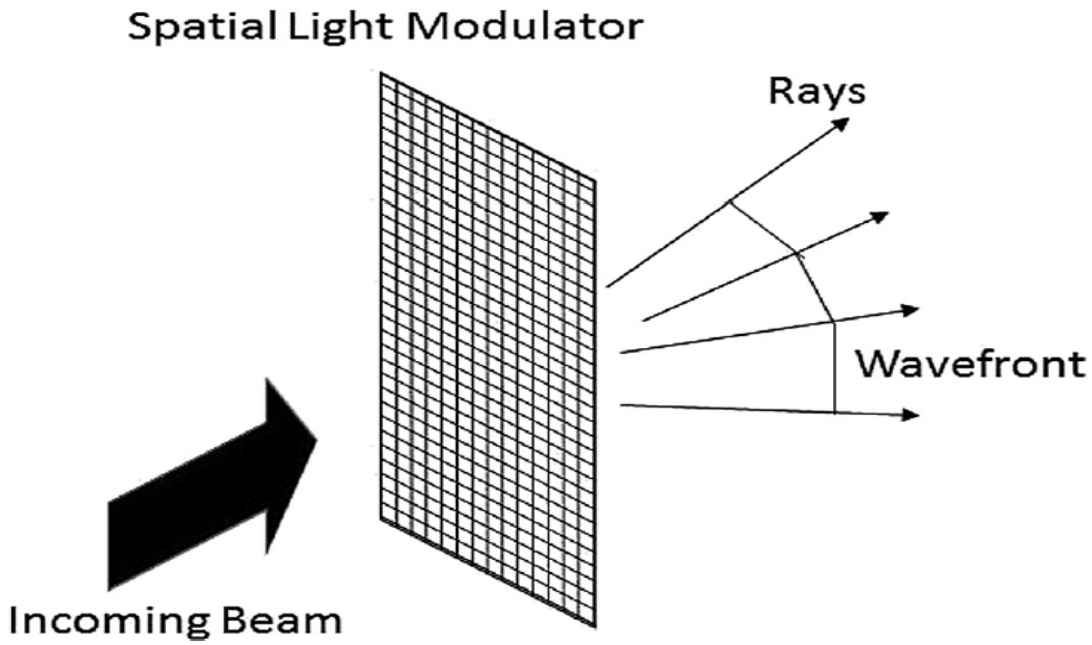

Figure 3.1: Illustration of spatial light modulator action on an incident beam in transmission [92]. The wavefront for the incident beam is modified by the SLM, and thus the outgoing beam is diffracted into different orders.

.

Spatial light modulators are based on the same technology as liquid crystal displays; therefore, they are mostly organized into rectangular arrays of pixels, with electric contacts that are made from transparent conducting materials[92]. SLM pixel density can be very high, reaching 1920 by 1080 resolution for high definition device requirements, having an active area of approximately 20 mm with pixel pitches of less than 10 μm each. The

operating principle of SLM depends on the type of liquid crystals material they are made of, in particularly, the ability of liquid crystals to control the polarization of light. The most straightforward application is using a twisted nematic liquid-crystal based spatial light modulator made with two linear polarizers on each side. The light entering the SLM is first polarized linearly using a polarizer and exits through a linear polarizer with an orientation of 90 degrees to the first. The second polarizer works as an analyzer and is desired for light intensity modulation application of a SLM.

3.3 Control of SLMs

SLMs can be divided into two subcategories based on the type and nature of the signal used to control their optical properties: electrically addressed SLMs and optically addressed SLMs. As is clear from their names, they are respectively controlled by applying an external electric field and optical beams onto the back and front surface [34].

3.4 Electrically Addressed SLMs

Spatial light modulators are widely used in displays and projection systems, which mostly comprise of output devices used for computer, therefore, they can be controlled by electrical signals similar to those used for computer outputs.

When there is no electrical signal provided to a transmissive SLM, the twisted nematic liquid crystal controls the light polarization from its state referenced at 90 degrees from the incident state, hence, the incident light can pass through both polarizers, which are perpendicular to each other. When an electric field is applied, it will change the orientation of the liquid crystal molecules, thus the polarization of light is rotated by 90 degrees and the light does not pass through a crossed polarizer. The entire transverse phase profile of

the beam that passes through the SLM can be controlled by changing the voltages applied to the pixels [92].

When a voltage is applied to the transparent electrodes, it generates an electric field between it, and thus forms a parallel-plate capacitor, as represented in Figure 3.2. In a parallel plate capacitor, the voltage and the electric field are related by the following

$$\text{Electric Field} = \frac{V}{d}, \tag{3.1}$$

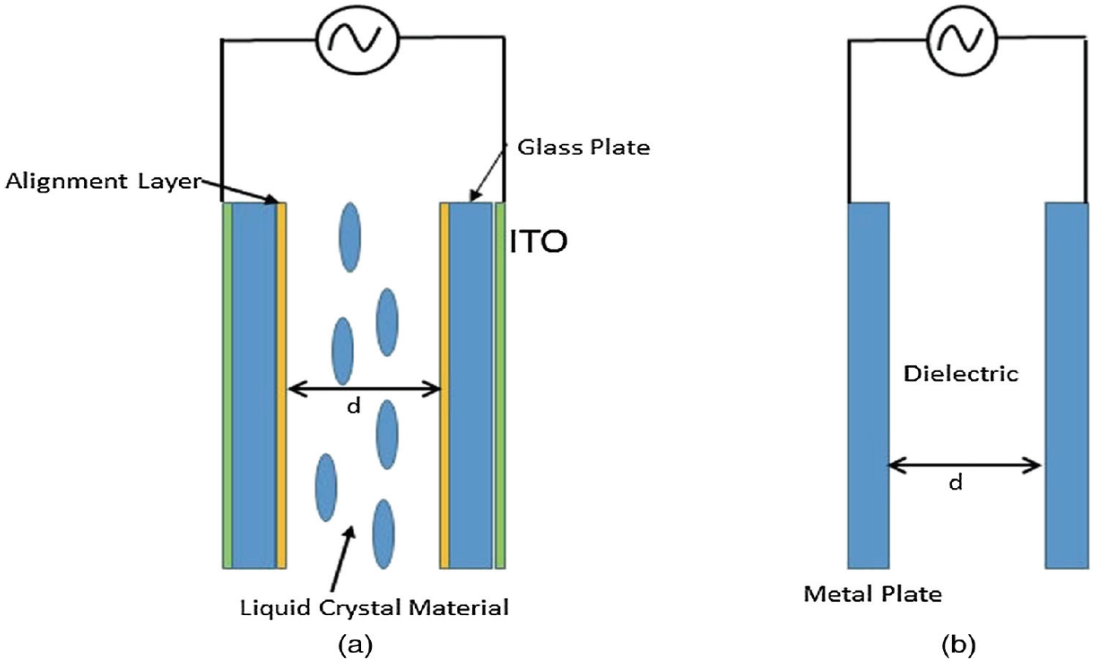

Figure 3.2: The image compares between (a) electrically-addressed liquid crystal cell and (b) parallel-plate capacitor. The two configurations, apart from the optically active material (liquid crystals), are similar [92].

.

where V is the voltage applied to the plate and d is the plate separation. When the voltage increases or the plate separation decreases, the electric field is amplified. As a result, thinner devices will be easier to drive eclectically. Nevertheless, the capacitance is

inversely proportional to the plate separation and is expressed as

$$C = \varepsilon_r \varepsilon_0 \frac{A}{d}, \tag{3.2}$$

where A is the area of the plate of a dielectric material, ε_r is the permittivity of a dielectric, and ε_0 is the free-space permittivity.

The capacitance effect is significant by considering its effect on the time it takes to make alteration in electrical field. This time is referred to as the RC time constant, which is the product of resistance and capacitance. This effect is what makes thicker devices appreciable as more capacitance is in the system; and the more slower the device can be changed. The energy stored in the capacitor is written by

$$E = \frac{1}{2} c v^2. \tag{3.3}$$

As we seen equations (3.2) and (3.3), show the challenge in producing liquid crystal devices is that it can be designed to work at low voltages as well with quick response time. The measurement for capacitance is a necessary quantity in SLM devices. On the other hand, the relaxation dynamics of the liquid crystal material governs the optical response time of the liquid crystal cell, not the RC time constant.

If a thicker device is required, it means the presence of a slow device with a huge capacitor, in other words, a higher capacitance will be desirable.

.

3.5 Optically Addressed SLMs

Optically addressed SLMs use an optical signal to control the dynamics of liquid crystal. The schematic of an optically addressed SLM is shown in Figure 3.3. The light incident on

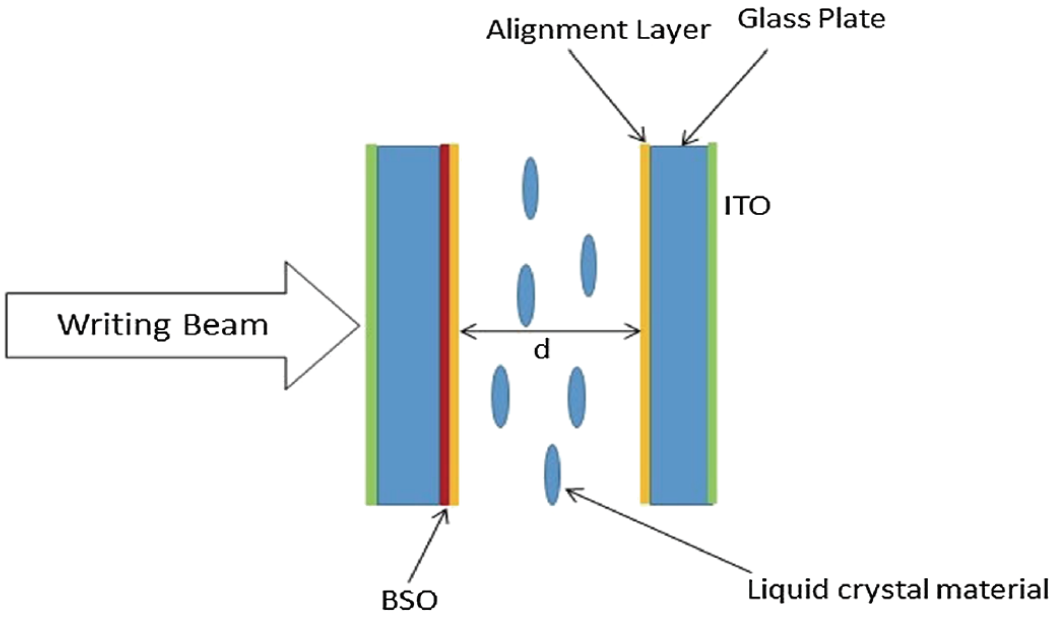

Figure 3.3: The image shows the configuration of an optically-addressed liquid crystal cell. The optically active material used in this device is a thin layer of Bismuth Silicon Oxide – $Bi_{12}SiO_{20}$ (BSO) [92].

the photosensor side obtains an image projected onto it. Bismuth silicon oxide ($Bi_{12}SiO_{20}$) or BSO is a photosensor material used in such devices. The light incident on the BSO photosensor is converted into a proportional amount of charge which then modifies the potential on each pixel based on the intensity of light. The image will remain so long as the SLM remains powered and is not refreshed [92, 34].

3.6 Basics SLM Application

Since the invention of SLM, its application is ever increasing, and the technology is getting more sophisticated by the day. Though it is generally thought in terms of higher pixel densities in a device, this is not necessarily true. In many cases, the ability to use special geometries for electrical elements, can be as significant as the number of pixels or optical elements in a device. For example, in case of simple shutter, it is possible that it only

requires a single electrical element, but the ability to use several shapes for this element can enhance the performance of the system optically.

3.6.1 Optical Switching for Telecommunications

In advanced telecommunications, the standard for transferring information from one place to another is fibre optics. This is primarily due to very high data transmission speeds as well as the broadband property of optic fibres. Techniques like wavelength-division multiplexing is employed to increase the data carrying capacity of fibre by using parallel channels in the fibre, where each channel is associated with a specific wavelength of light. Wavelength-division multiplexers and a demultiplexer (in principle spectrometers) are used in the transition at the receiving sites to carry out multiplexing techniques. Multiplexing and demultiplexing in wavelength division multiplexing are mostly carried out using arrayed waveguide gratings [92].

3.6.2 The Digitally Tunable Optical Filter

In multispectral imaging and hyperspectral applications, optically tunable filter are highly preferred, since these techniques capture images that may comprise of a variety of color bands [42]. In some instances, it is possible to acquire bands that have wavelengths slightly separated from each other. Further, the techniques make use of many images that are similar in various color bands to help detect diverse difference- wavelength-sensitive topology. The end goal here is to obtain several images that are closely related, and therefore, the time between collecting the different color bands should be short, hence such requirement renders the simple filter wheels, which simply switch between filters, useless. Lyot filters that are constructed from birefringent plates are commonly used to make the tunable optical filters.

When various such filters are stacked together, hence a multiplate filter, each plate is

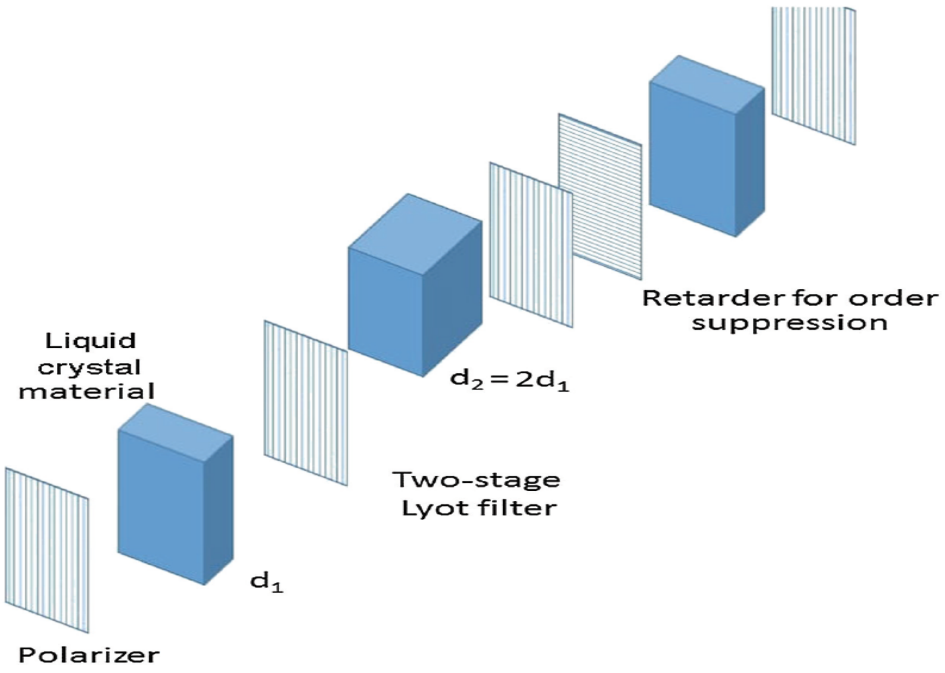

Figure 3.4: Optical design for tunable filter liquid crystal. The thickness of the second liquid crystal cell (d_2) is twice of the first and the third ones (d_1), i.e. $d_2 = 2d_1$.

designed such that it is half the size of the original plate in terms of its thickness, as shown in Figure 3.4. Birefringent plates are used to adjust the quantity of light that passes through the plates to become either ordinary or extraordinary, and this is dependent on incident light polarization such that plates rotation alters the transmission peak wavelengths. These devices characterize the bandpass spectrum/region which is dependent on the birefringent characteristics of the material. To avoid the manual rotation of the plates, birefringent plates can be replaced by liquid crystal devices which can to control the state of polarization when a voltage is applied to them. Several wavelengths passed by the liquid crystal devices are used to digitally map a input for digitally tunable filters. The main disadvantage of such array of polarizing elements is that they effectively decrease the intensity of transmitted beam, mainly because of the collective transmission of polarizing elements. To avoid this, wider bandpass windows can be used.

Presently liquid crystal tunable optical filters cover wavelengths approximately ranging between 400 nm and more than 2300 nm, and they can refresh/switch filters at a rate of

around 100 ms. In terms of their operation, they are very stable, and they can remain effectively operational for many years. They are largely applied in spaceborne instruments because of their requirement demanding very few moving parts to introduce inertial change and vastly low power requirement as compared to other devices used for similar purposes [92].

3.6.3 Fabry–Pérot Tunable Filter

Fabry–Pérot tunable filters are interferometers simply constructed from two partially reflecting optical glass flats, which are in close proximity to one another. The optical flats are illuminated by a collimating lens with an extended diffused light source, and this results in multiple reflections being formed between the two optical flat surfaces. The light that emerges is then refocused onto a screen, and this results in the formation of an interference pattern with multiple rings, resembling Newton rings, called Tolansky fringes.

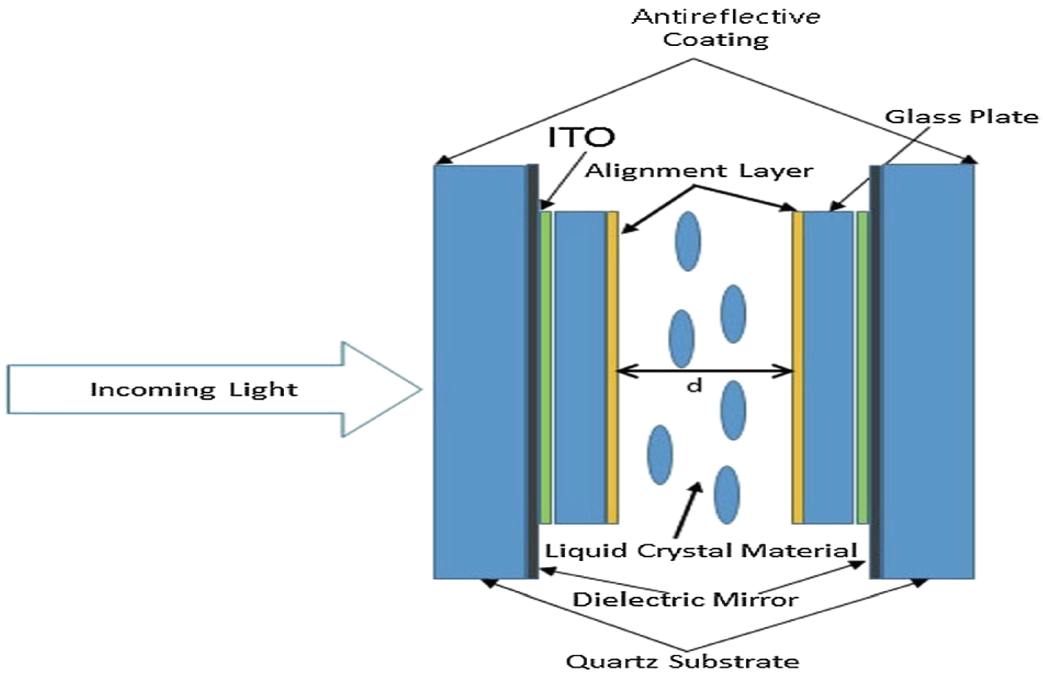

Figure 3.5: Liquid crystal cell inside a Fabry–Pérot cavity works as a tunable optical filter [92].

.

This filter can be fabricated from liquid crystal devices where on the liquid crystal device, optical flats are used as windows. In this case, the working range of wavelength for the interferometer is determined by the refraction index of the liquid crystal and the separation between the plates [52]. The configuration of the liquid crystal Fabry–Pérot tunable filter is shown in Figure 3.5.

As etalons, these filters can also be made from a single piece of optical glass flat. In such case, the two surfaces of the glass flats lay out the two reflecting surfaces that are parallel to one another, and the thin glass region separating them. Fabry–Pérot tunable etalons are mostly found in applications applied in thin-film optical filters, optical resonators, spectrometers as well as telecommunications [72].

A multilayer Fabry–Pérot tunable filter can be constructed by compiling a sequence of thin-film layers onto a planar substrate, the result is narrow-bandwidth transmission optical filters. In order to fabricate induced transmission filters with high signal-to-noise ratios, it is important to carefully manage the dielectric layer separation between the thin metal layers. .

Widespread application of optical etalons can be owed to its flexible characteristics, as they are easily tunable, and they also have a light output response of a "comb" structure. Multiple reflections and transmissions in the resonant cavity, as depicted in Figure 3.6, defines its tunable properties. The free spectral range or the wavelength separation between the adjacent transmission peaks, i.e. $\Delta\lambda$, is given by

$$\Delta\lambda = \frac{\lambda_0}{2nl\cos\theta}, \tag{3.4}$$

where λ is the central wavelength, and l is the thickness of the sample as Figure 3.6 shows. The $\Delta\lambda$ represents the full-width-half-maximum FWHM of the transmission peak. The free spectral range to the FWHM (ratio) is defined as the finesse [92].

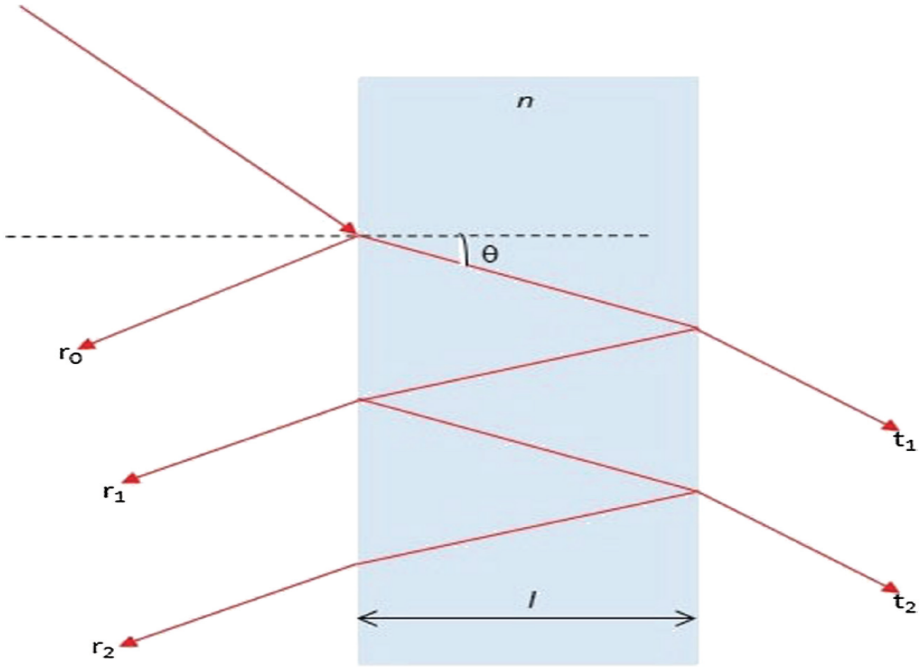

Figure 3.6: The image represents the multiple reflection in Fabry–Pérot etalon [92]. r_i and t_i indicate the ith reflection and transmittance coefficients, respectively.

3.7 q-Plates

In this section, we explain the operation of q-plate, q-plate fabrication, and some application of q-plate.

3.7.1 Operation of q-plate

q-plates which were introduced by Marucci et al .[2006], are devices that are based on the concept of Pancharatnam–Berry (PB) phases [16] which is a totally different approach as compared to the holographic techniques or variable optical path length based techniques. The Pancharatnam–Berry phase can be defined as a geometric phase shift with respects to the polarization of light. When the beam of light with uniform polarization travels along a closed defined loop on the Poincaré sphere (PS), the initial state acquires a phase factor; hence the final state differs by factor equal to half of the area circumvented by the loop on the Poincaré sphere (PS).

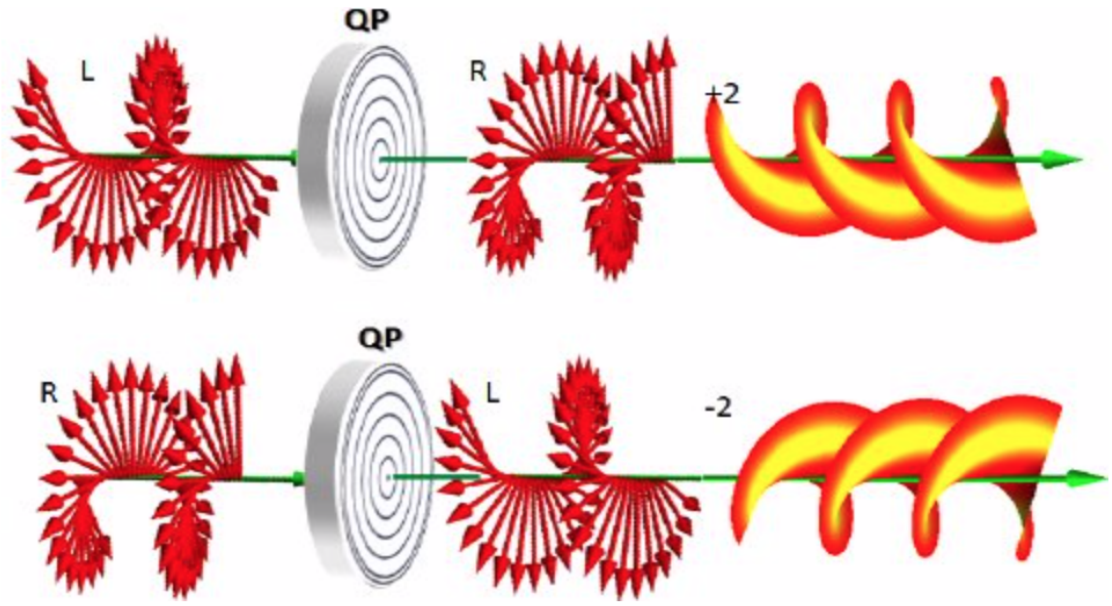

Figure 3.7: The schematic representation of q-plate. The handedness is flipped after passing the q-plate. For upper panels input left circular polarization invert to right circular polarization and *vice versa* for lower panels [76].

A q-plate is made of birefringent materials like liquid crystal (LC) film, LC film is sandwiched between two indium-tin oxide (ITO) coated glass plates. q-plates are defined with parameter such as phase retardation δ and transverse optical axis pattern with topological charge q [76]. Molecular director (n), defined as the average molecular orientation in anisotropic LC cell, are oriented in the specific azimuthal pattern for q-plate. In general the angle between fixed central axis (defined with respect to azimuthal coordinate) and n in the cell plane, represented by α, is a linear function of the azimuthal angle φ defined by the following equation in the cell plane. The optical axis in the polar coordinate (r,φ) that can be written as the following

$$\alpha(\varphi) = q\varphi + \alpha_0\,, \tag{3.5}$$

where q is the topological charge of q-plate, α_0 is a constant angle, φ is the azimuthal angle of the polar coordinates. The incident beam after passing through a q-plate is separated based on the polarization of the incident light. Then the relative phase of these two components will be delayed with respect to each other. When these beam couple at the output, it has the form of a vortex beam carrying OAM. The working principle of a q-plate can be described in terms Jones matrices. It manipulates an optical field at a given transverse position r and φ is given by

$$M(\varphi) = \cos\left(\frac{\delta}{2}\right)\begin{pmatrix}1 & 0\\ 0 & 1\end{pmatrix} + i\sin\left(\frac{\delta}{2}\right)\begin{pmatrix}\cos\left(2q\varphi + 2\alpha_0\right) & \sin\left(2q\varphi + 2\alpha_0\right)\\ \sin\left(2q\varphi + 2\alpha_0\right) & -\cos\left(2q\varphi + 2\alpha_0\right)\end{pmatrix} \tag{3.6}$$

where δ is the optical retardation of the plate. The action of a q-plate on a circularly polarized input light, $E_{in} = E_0(r)(1 \ \pm i)^T$, can be determined by $M(\varphi)\cdot E_{in}$, where $E_0(r)$ is the input beam radial profile. The $+$ and $-$ signs stand for the left and right circular polarizations, respectively. The output of a q-plate can be expressed by the following equation

$$\begin{aligned} E_{out}(r,\varphi) &= E_0(r)M(\varphi)\cdot\begin{pmatrix}1\\ \pm i\end{pmatrix}, \\ &= E_0(r)\cos\left(\frac{\delta}{2}\right)\begin{pmatrix}1\\ \pm i\end{pmatrix} + iE_0(r)\sin\left(\frac{\delta}{2}\right)\begin{pmatrix}1\\ \mp i\end{pmatrix}e^{\pm 2i(q\varphi+\alpha_0)}. \end{aligned} \tag{3.7}$$

The action of $q = 1$ plate when its optical retardation is $\delta = \pi$ in the circular polarization bases is shown in Figure 3.7 [75]. When the q-plates are tuned they convert the right circular polarization to left circular polarization or vice versa and, due to the topological structure of birefringent liquid crystal in the transverse plane, gain a positive or negative helical phase front $\exp\left(\pm 2iq\varphi\right)$. In the quantum mechanical formalism, when the SAM and OAM states are respectively given by $|\pm 1\rangle_\pi$, ± 1, and they stand for left and right-handed

polarization, and $|\ell\rangle_o$, the q-plate action is

$$|+1\rangle_\pi \otimes |\ell\rangle \xrightarrow{q-\text{plate}} |-1\rangle_\pi \otimes |\ell + 2q\rangle \tag{3.8}$$

$$|-1\rangle_\pi \otimes |\ell\rangle \xrightarrow{q-\text{plate}} |+1\rangle_\pi \otimes |\ell - 2q\rangle \,. \tag{3.9}$$

q-plate acts as a spin-to-orbit coupler and thus converts an incoming light with spin angular momentum +1 into a beam with a spin angular momentum of -1 and an OAM value of $+2q$. Here, q is the q-plate topological charge. On the other hand, if the incoming beam possesses spin angular momentum of -1, the q-plate will flip the polarization value into +1 and decrease the OAM value by -2q. The q=1-plate is cylindrically symmetric and thus conserved the total optical angular momentum. Therefore, it is not expected to change the optical angular momentum as long as the direction reading is z. To illustrate, if an incoming spin angular momentum (+1), a left circular polarization with an OAM, the result would be for the initial state, $\ell + S = \ell + 1$ in the unit of $\hbar$, moreover, the final state optical angular momentum will be after passing through the q-plate, $\ell + S = \ell + 2 - 1 = \ell + 1$ in the unit of $\hbar$, after that, the total angular momentum conserved.

3.7.2 q-Plate Fabrication

In this section, we explain the fabrication of q-plate in our laboratory. This q-plate has been used on QKD which is chapter 5, followed by characterization of q-plate.

Two indium-tin oxide(ITO) coated glass substrates were prepared by spin coated with a photon-sensitive polymer(ex. azo-dye) on each side of the glass, then they were subsequently heated for 5 minutes at 120 ° C until evaporating the solvents. Spacer-grade silica microspheres which have a diameters that are below 4.8 μm are placed between two coated ITO plates. Then, the plates were fixed to each other using epoxy glue. Liquid crystals were filled between the empty space, after aligning the polymer, in the final stage.

The next step is to print the phase pattern (any desired structures) in the plate (glass substrate) over the polymer layer. The polymer was aligned using the photoalignment method. A specific pattern was printed that has been pre-designed using computer generated holography. Now, the plate (glass) that has a phase pattern was uploaded onto the imprinting setup, which is comprised of a UV laser, a half-wave plate, a 4-f system, and a digital micromirror device (DMD) as represent in Figure 3.8. For the photoalignment, the sample was illuminated with a UV light (wavelength 405 nm) onto the half-wave plate, a cylindrical 4-f system with DMD, subsequently reflected to the second cylindrical 4-f system then sample. An Iris was used to select the brightest diffraction orders that go to the sample (plate), omitting the spatial grating effect of the DMD. When we illuminate with a UV light, point by point illumination aligns these polymers by the end "pixel by pixel" on the right side of the screen. Therefore, the polymer can be oriented in a specific topology as we rotate the polarization that corresponds to a different phase. The polarization will define which orientation of the polymer will take $q = \pm 1, \pm\frac{1}{2}$ (topological charge). As the next step, liquid crystals were injected between the two glass substrates, the liquid crystal follows the alignment of the polymer. Afterwards, an external electric field (from an AC function generator) was applied across the (plate) bias of glass, and LC started aligning at a different voltage.

3.7.3 Tuning Voltage

The q-plate was fine tuned by changing the phase retardation with an externally applied voltage from a function generator. By varying the voltage, sinusoidal with a frequency between 4 kHz to 10 kHz, the phase retardation of q-plate can be controlled. In this section, we demonstrate the characterization of the q-plate as the function of the applied voltage; namely determining the part of the beam that gains the phase (converted part) and the part that has not been affected by the q-plate (unconverted part). In this experiment, we used a diode laser with a wavelength of 635 nm to characterize the q-plate. The schematic

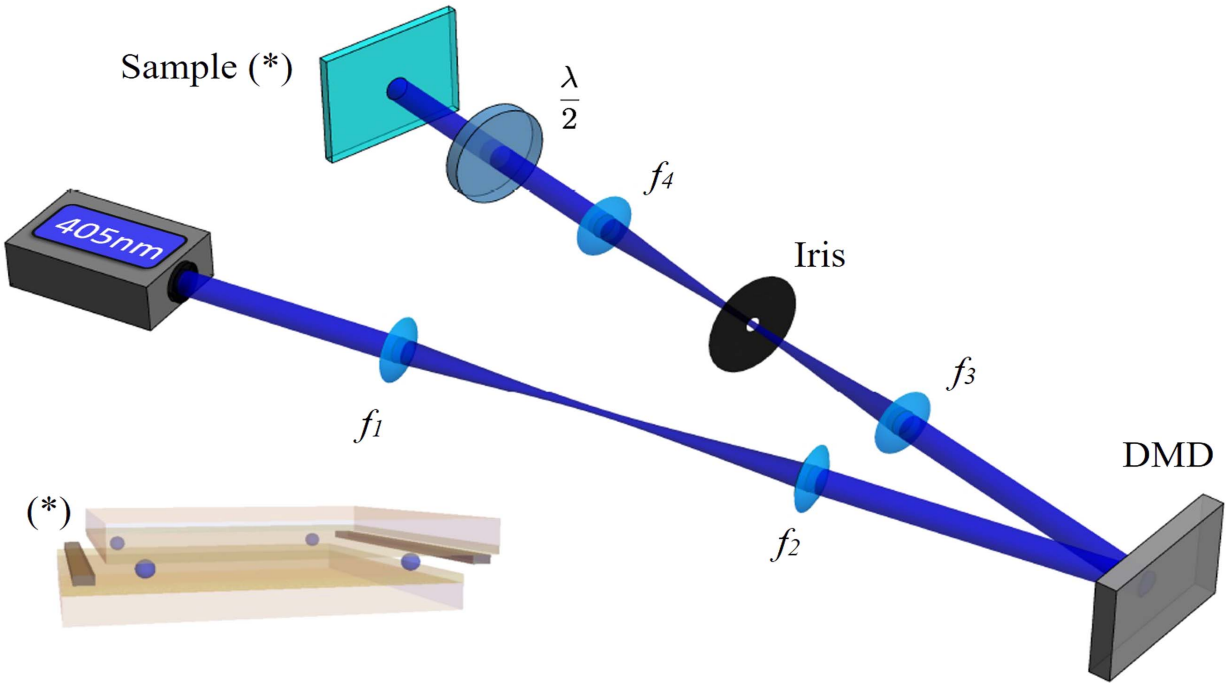

Figure 3.8: The schematic representing the setup for liquid crystal fabrication. The laser (405nm) travels through a 4 -f system to a DMD mirror, after that light is reflected from DMD mirror to second 4-f system, the iris in middle to select the first order of diffraction then project on the sample. This image reveals an anatomic constructional delineation located at the lower-left section of the drawing[66].

.

of the setup used to characterize a q-plate and measure both converted and unconverted part of the beam (as well as the transmission efficiency) is illustrated in Figure 3.9. The linearly polarized beam from the diode laser is converted to a circular polarization after passing through the first quarter-wave plate (QWP), oriented at 45 degrees. The circularly polarized beam traverses through the q-plate.

If the optical retardation of the q-plate is set to π, the handedness of the input circular polarization is filliped (e.g. from left to right). However, in other cases, both handedness of circular polarization states exists at the output beam: one part with opposite handedness gains the phase (converted part), and the unconverted part has the same handedness as the input beam. The converted and unconverted parts of the beam can be selected and sent into two different power meters by means of a QWP (set at 45 degrees) and a polarizing

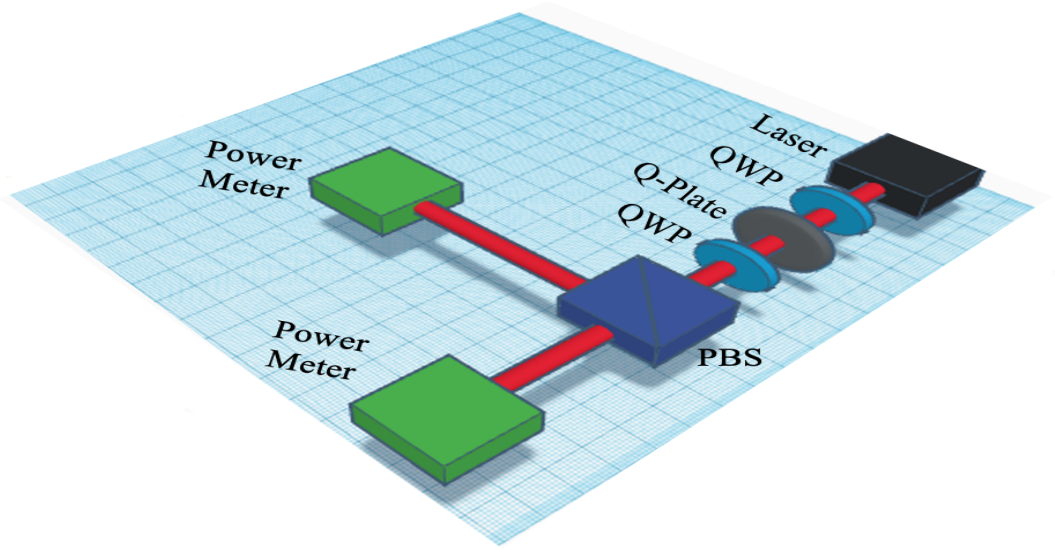

Figure 3.9: The schematic representing the experimental setup used to characterize q-plates. The experiment contains QW: quarter - wave plate, q-plate, and polarizing beam splitter (PBS). Both sides used power mater to measure the converted and unconverted beams as a function of external voltage.

.

beam splitter (PBS). It is noted that the incident beam was converted to the left circular polarization by the first QWP, then converted to right circular by a q-plate, and to a linear by the second QWP and finally split apart by the PBS. We are measuring both the reflected and transmitted beam simultaneously. Experimental results for measuring the power of both converted and unconverted beams as a function of external voltage are shown in Figure 3.10. As can be seen, the q-plate retardation is close to π when an external voltage of 3.7 V has applied to the substrates.

Using q-plate, we can produce OAM with a value of $\pm 2q$, q is the plate topological charge. When the q-plate is electrically tuned, it converts an incoming Gaussian beam into a beam carrying orbital angular momentum or a space-varying polarized beam. These beams possess a phase singularity at the center, and we will have an intensity profile resembles of a doughnut-shape.

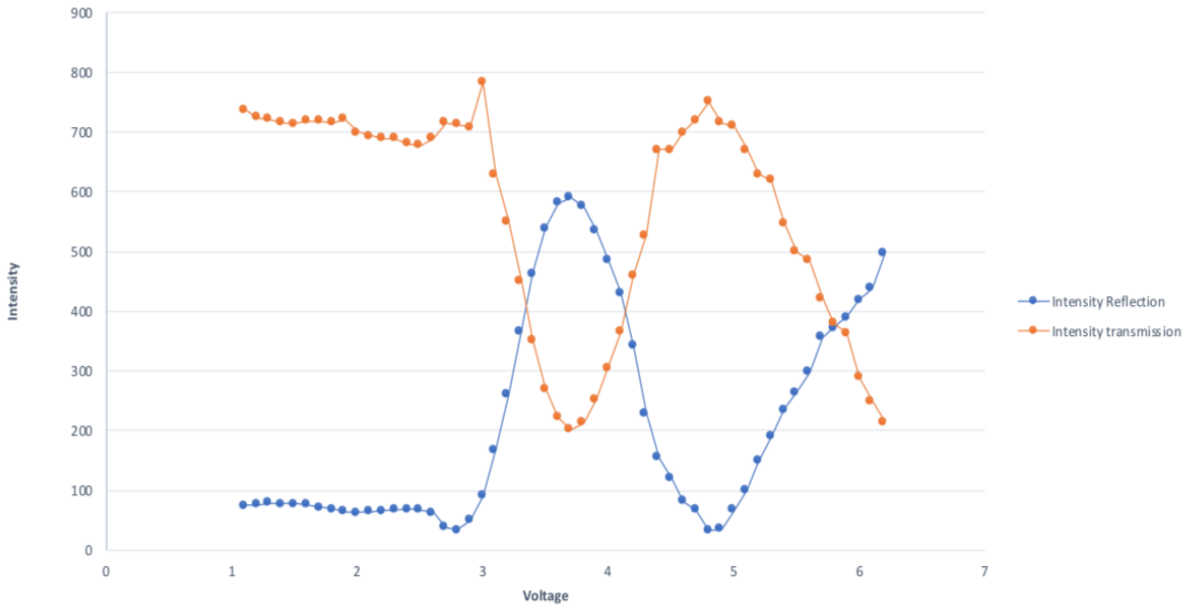

Figure 3.10: Measured power of the converted and unconverted parts of the outgoing beam from a q-plate as a function of the applied voltage.

3.7.4 Application Q-plate

The q-plate offers several technological advantages in comparison to the other contemporary techniques for the generation of structured light beams. Following points describe few out of many:

(i) As one of the primary functions of the q -plate is SAM to OAM conversion. The conversion efficiency of any optical device indicates its efficacy; with the help of anti-reflective coating efficiencies of up to 96% are commonly achieved. (ii) For q-plates SAM to OAM conversion is the function of its birefringent optical retardation δ, which depends upon birefringence of liquid crystals (LC) and LC film thickness. Major advantage of q-plate is in electrical modulation of the phase retardation factor i.e.,δ can be electrically controlled. Direct consequence of such control is that q-plate can be literally turned on/off with minimal change to any other optical parameter.

(iii) Robust and instant control of optical retardation permits the generation of super-

position of SAM/ OAM or OAM-OAM states without using any standard interferometry techniques.

(iv) In order to access higher OAM values, multiple q-plates can be arranged in cascaded geometry to address such needs with optimal efficiency.

(v) For any optical device factors like aberrations (for eg. astigmatism) limits its effectiveness as a technology. Unlike holographic techniques, q-plates are not based on the principle of diffraction. Usage of deflected beams in other methods introduce astigmatism in the beam; hence q-plates does not introduce astigmatism.

(vi) q-plate are primarily based on the transmission geometries which fundamentally makes such devices free of many optical alignment issues.

(vii) q-plates can be designed to work with wide-band of frequencies and can also work with the intense ultra-fast lasers.

(viii) q-plate are significantly cheaper than SLMs and are also very compact, stable with minimal maintenance[95].

Such advantages has led to the application of q-plates in fields like classical[95], quantum communication[60], quantum cryptography[[102], spatially controlled nano-structuring of matter[89], STED nanoscopy[119], generating vector beams etc.

Chapter 4

Magic Mirror

This chapter demonstrates our work with magic mirrors. We also present some background on previous studies of magic mirrors, followed by our experimental methods and results.

4.1 Background of Magic Mirror

Ancient Japan and China have cast and polished bronze mirrors with very interesting properties that had been seen as magical for a long time [13]. An example of an ornamental design embossed on the back surface of these mirrors is presented in Figure 4.2. In these oriental magic mirrors, relief undetectable by the naked eye can cause the mirror (4.1) surface to reflect incoming light to create a distinct pattern onto a screen as shown in Figure 4.3. The aim of this section is to explain how the theory of these unusual relics can be modified to create a magic window, a seemingly undistinguished transparent glass sheet whose invisible topology can be observed through a refracted light beam on a screen, with the light intensity replicating the invisible topological pattern. The theory emanates from the fundamentals of geometrical optics, wherein the surface topology features only partially focuses the light rays, therefore altering the light intensity without forming a bright envelope before the focus, as seen in caustics. The theory is simple, basically the

Laplacian of the surface relief is defined by the intensity on the screen, therefore determining the relief necessary to generate the desired picture [14, 27, 99].

Figure 4.1: The image present the magic mirror convex reflecting face[13].

.

Figure 4.2: The image exhibits an ornament embossed on the back surface of the mirror. Image depicted from [13].

.

Figure 4.3: The amplified magic-mirror picture is shown onto an interface by the lighted front face. Image depicted from [13].

The light reflection mechanism, not only explains the way of manifesting a portrait through unlit patterns on an illuminated surface, but also it justifies the portrait's sharpness that it displays at any point on the interface. However, the portrait magnifies as the space grows between it and the interface as shown in Figure 4.4. Also, the thicker its components in width are, the more the mirror lays out that allow the appearance of bright areas on the interface. On the other hand, if the components are thinner and narrower, more unlit parts will be shown on the display as demonstrated in Figure 4.5. Such mechanism illuminates the dark lines appearance on a bright background from a patterned image carved in the back of a mirror (Figure 4.4) [73].

Several interpretations have been offered to explain the variance curvature on the reflecting surface. The mirror is made by casting Bronze into a template that has the bottom of the mirror configurations; however the surface semblance is pounded and refined to a convex surface shape. In 1992, Swison proposed that the buffed surfaces (the slimmer parts of the mirror) curved marginally internally, and thus exposed to slightly less focused pressure and rubbing exertion. He indicates that the forging outcome, is a polished cor-

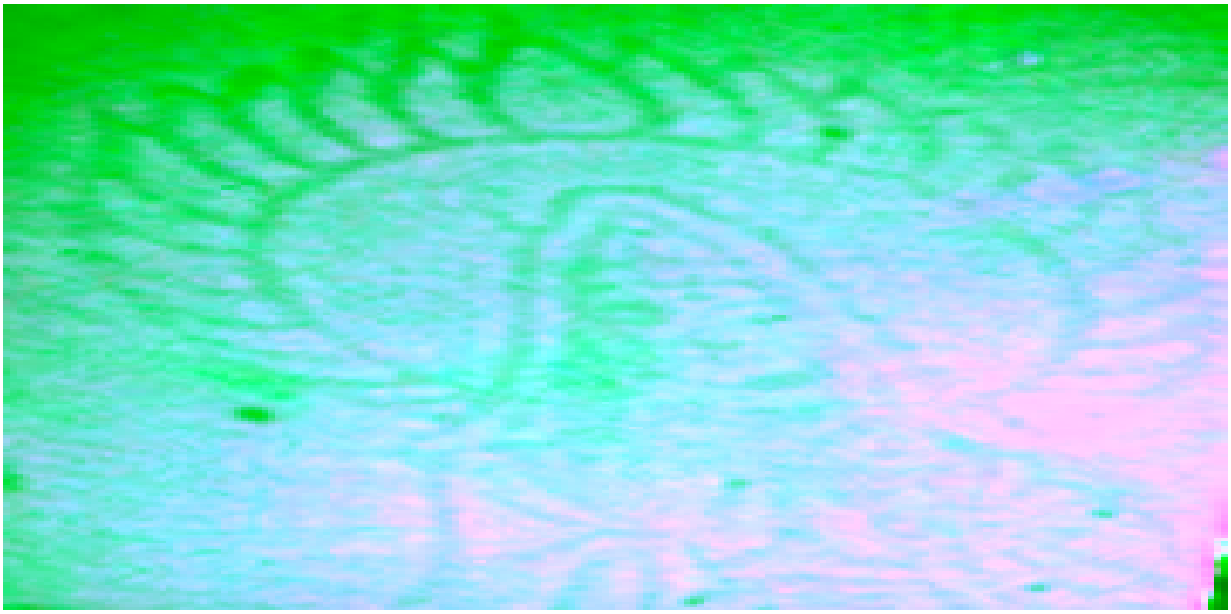

Figure 4.4: The image represent the projection pattern of the mirror[73]

tex which contains, on the below side, repetitive configurations with delicate protrusions. Nevertheless, a study by Yan suggested in the same year that while the liquefied bronze hardens, the finer part of a mirror loses heat therefore turns into a solid form more rapidly in comparison to wider part, which leads to the formation of the delicate protrusions on the reflecting surface[73]. The display pattern does not result from the focusing efficiency of standard imagery formation due to its sharpness independence of distance and the slightly convex shape of magic mirrors. It is ancient to the extent that the effects resulting from the lights projection variations by undulations on the reflecting exterior, generated during the crafting sequence, are difficult to sight clearly while reproducing a much stronger imprint embossed on the back end.

Makyoh imaging, which is the Japanese nomenclature for the marvelous mirror, has been applied to discover meager engravings on partially semiconductor surfaces [65].

Sir Michael Berry portrays the physics behind magic mirrors and windows in 2006 and 2017, respectively. We have created a 'flat' version of the magic mirror (window) in our work. To understand its action, the intensity pattern of the reflected beam is recorded at

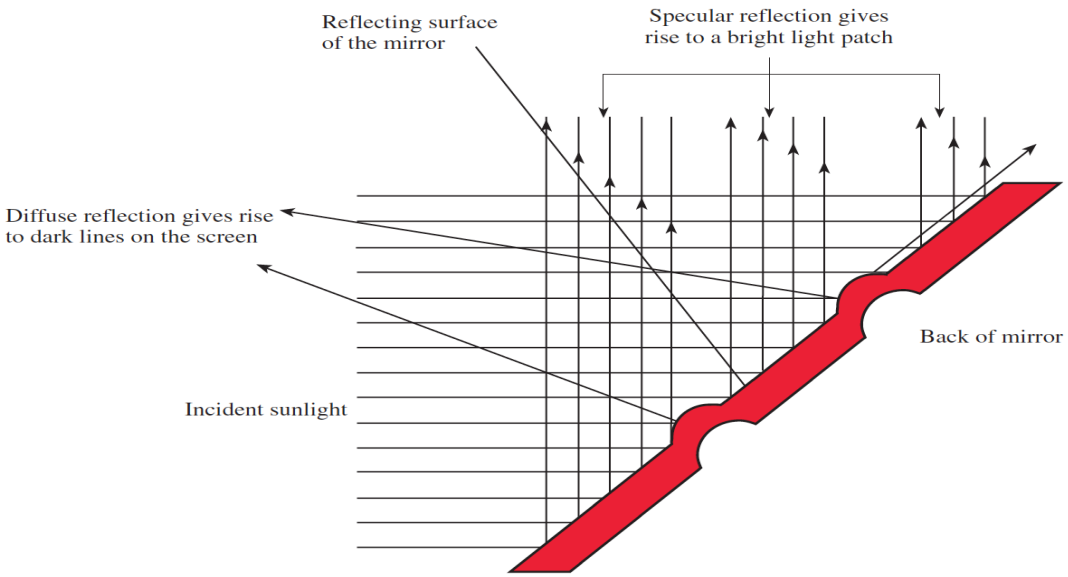

Figure 4.5: The image represent the explanation magic mirror The bright area on the screen are created by the thicker parts of the mirror lay - out while the dark area created by the thinner parts[73].

different planes, proving that such a mirror/window can be manufactured with flat optics.

Since the interior optics of magic mirrors is known, it has not been focused on, neither by qualitative interpretations nor thorough geometrical-optics anatomy[109, 93], the purpose is to shed some light on the optical regime relevant to magic mirrors, the image intensity determination based on the height function of the $h(r)$ the relief on the reflected surface, by the Laplacian $\nabla^2 h(r)$ is the position in the mirror plane: $r(x, y)$. A more detailed explanation of the geometrical optics is included below.

4.2 Geometrical Optics and the Laplacian Image

In this section, we explain the geometrical optics for the Laplacian image.

The light reflected from a mirror's surface (r'), which possesses a gentle variation $h(r')$, forms the image in the observation plane r as shown in Figure 4.6. The calculation of the deviation of the surface undulations from a convex mirror is given by

$$\eta(\acute{r}) = -\frac{\acute{r}^2}{2R_0} + h(\acute{r}), \tag{4.1}$$

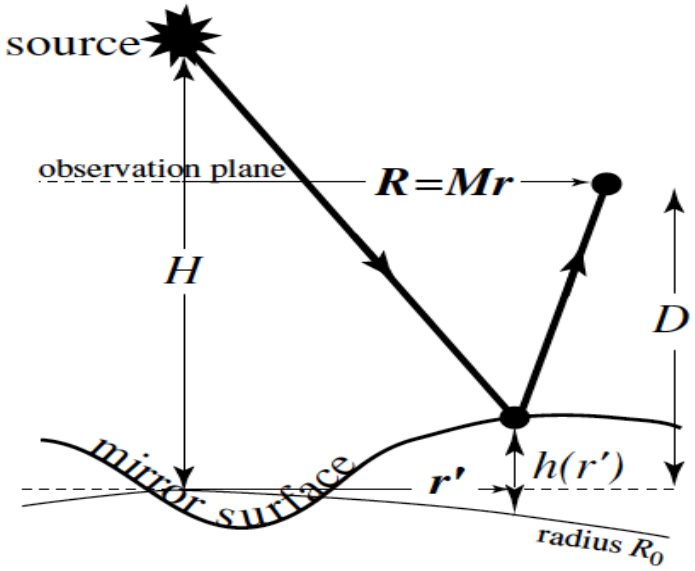

Figure 4.6: The image illustrates geometry optic an formation of the magic mirror. H is distance from source to reference plane and D is distance from reference plane to position R on screen range. Image depicted from [13].

where R_0 is the radius of curvature and h is the surface height profile. Michael Beery [13] found the variation of thickness of the surface height profile given by first-order approximation by the Laplacian that is a link to the intensity of the image and given by this equation

$$I_{Laplacian}(r, Z) = 1 + Z\nabla^2 h(r), \tag{4.2}$$

where $\nabla^2 h$ is Laplacian of variation of thickens of surface height profile, Z is reduce distance as light propagation given by $Z = \frac{2D}{M}$, $M = 1 + \frac{D}{H} + \frac{2D}{R_0}$, and $r = \frac{R}{M}$. Where R is the position on observation plane, M is magnification factor of the convex mirror, H is distance from the source and D is distance from the mirror.

4.3 Numerical Simulation of Laplacian Image

In this section, we explain the numerical simulation that leads later to forming the theoretical image (4.15 - 4.16).

The numerical simulation is used to study the production of the magic image. We take a picture in a BMP format and calculate Laplace transform. Upon propagation, the image will form within different distances. First, we need to compute the phase for the window for the image using discrete sine transform (DST). When the Laplacian image based on refractive index of window written as following [14]

$$I_{Laplacian}(R, z) = 1 - z(n-1)\nabla^2 h(R) \tag{4.3}$$

In the magic mirror, we did not change the surface height profile; however, we did change point by point the refractive index of the window. Then, equation (4.2) becomes in terms of refractive index as follows [55]

$$I_{Laplacian}(R, z) = 1 - hz\nabla^2 n(R), \tag{4.4}$$

Where z is the distance between the image plane and the window, and (R) is the transverse plane based on refractive index. In the numerical simulation, we should use the discrete sine transform (DST) in order to solve the Laplacian equation. Solving the Laplacian equation (4.3) using DST with Dirichlet boundary conditions to get phase for the windows for the image. Solving equation (4.3) by discretized intensity function in terms of $I(R, r)$ is used to solve for $h(r)$, where $h(r)$ is the surface height profile. In our numerical simulation we consider the experimental factors such as wavelength of the light, i.e., 633×10^{-6} mm and the wavevector which is given by $2\pi/\lambda$. The image intensity is determined at different distances by using the propagation. The propagation was calculated based on the assumption that we have a uniform beam * phase window that we did calculated then

let it propagate using Fresnel propagation. If we want to look at intensity of phase, we have to take field of power 2 or look for window at different distance.

4.4 Experimental Method

The setup for this study is shown in Figure 4.7. With this setup, intensity patterns are created and characterized by the phase modulation of the SLM. The SLM used in this experiment (X13138 - Hamamatsu) is a device based on liquid-crystal technology for modulation of a light beam's wavefront. There are two types of SLMs: transmissive and reflective SLMs. In this study, we use a reflective LC SLM.

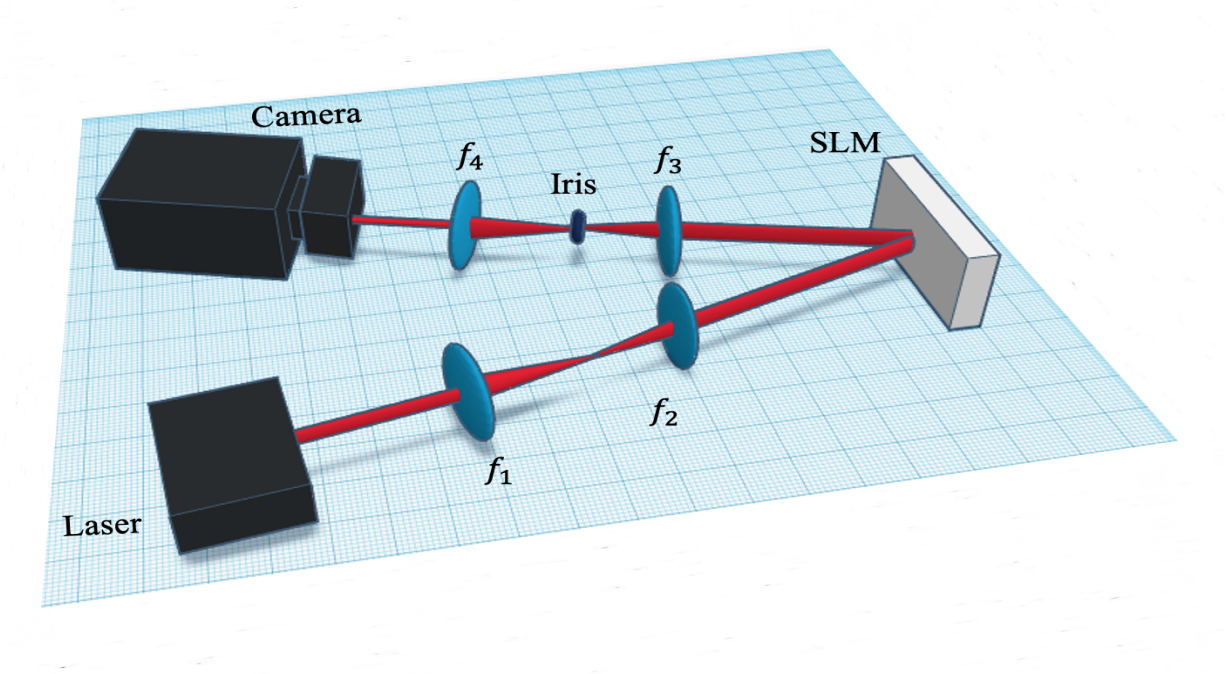

Figure 4.7: A 636 nm linearly polarized light beam is going through a cylindrical $4-f$ system to SLM. The reflected light from the SLM. goes through the second $4-f$ system pass through an iris between the two lenses blocks the other diffraction orders. After this, the beams go to record by camera.

The middle area on the figure 4.8 represents the liquid crystal on silicon (LCOS) chip. The LCOS chip is parallel nematic liquid crystal aligned layer, that has a pixelated two-dimension structural layout of transparent electrodes. The bottom side of the figure shows

the CMOS silicon backplane, which also has a pixelated two-dimension electrodes. Then the signal is sent from computer via CMOS backplane and DVI signals to electrodes. Once the signal is received, the required voltage is applied onto each of the pixels to create an electric field E. Under each voltage, the liquid crystal starts to rotate at certain angle, resulting in a refractive index change. Then, the phase of the incident light is modulated. The specifications of the SLM(X13138 - Hamamatsu) are as follows: pixel pitch is 12.5 μm, spatial resolution max is 40 lp/mm, number of pixel is 1272 $\times$ 1024 pixels, and light utilization efficiency is 79%.

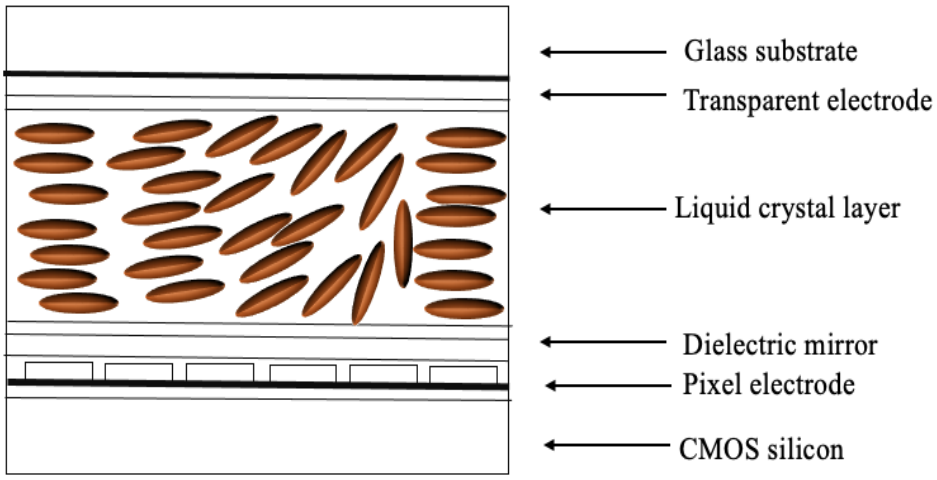

Figure 4.8: Schematically shows the basic structure of the LCOS- SLM. The LCOC- SLM consists of the glass substrate, a transparent electrode, normally made of indium tin oxide (ITO), dielectric mirror liquid crystal, CMOS silicon (complementary metal oxide semiconductor).

A laser beam (635 nm) magnified by a 4-f lens system, with focal length $f_1 = 50$mm and $f_2 = 300$mm, onto a SLM. A second 4-f lens system, with focal lengths $f_3 = 400$mm and $f_4 = 125$mm is used after the SLM to demagnify the modulated beam onto a camera. An iris is placed in the focus of lens f_3 to select the first diffraction order of the beam from the SLM. The image of the imprinted phase topology will only be seen on the camera when

the camera is placed at 125mm from lens f_4.

For a 4-f system, two identical lenses are utilized. The distance between them is $2f$, therefore, if anything is placed in-front of the object plane [O (x, y)], it will appear identical in the image plane [I (-x, - y)], including the phase and intensity. The entire distance is $f + f + 2f = 4f$, which explains calling it the 4-f systems. Even for two different lenses of f_1 and f_2, if they are placed in the following configuration as shown in figure 4.7 the label 4-f system would still be used.

4-f systems can be built with different lenses, give the same results, in comparison to the identical lenses-based system. In the set up that is used on our work, f_3 is larger than f_4, the distance between them is (f_3 + f_4). The entire system is [2(f_3 + f_4)], therefore, it also labelled as a 4-f system despite that one lens is different from the other. In case, the

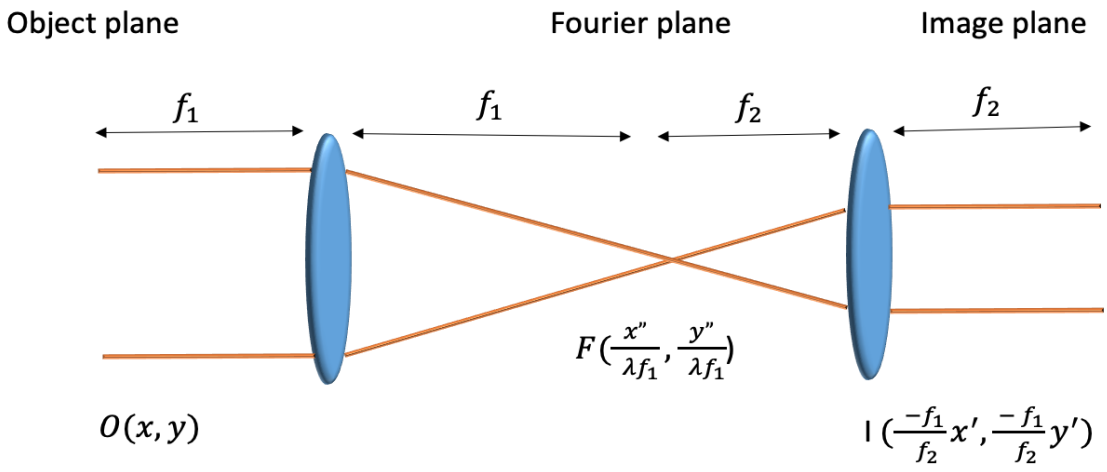

Figure 4.9: The image represents 4-f system.

object plane O (x, y) and image plane I (x, y) are identical, to the Fourier transform, which has no scaling factor; however, if the lenses are different, the Fourier transform of object will show different scaling factors by $F(\frac{x''}{\lambda f_1}, \frac{y''}{\lambda f_1})$ and the image plane given by$I(\frac{-f_1 x'}{f_2}, \frac{-f_1 y'}{f_2})$ as shown in Figure 4.9 . In summary, the pattern on object plane is scaled to $(\frac{f_1}{f_2})$ in the

image plane, which is similar to the concept in telescope systems, as it has been used in this project, to show that such a system reduces the beam value.

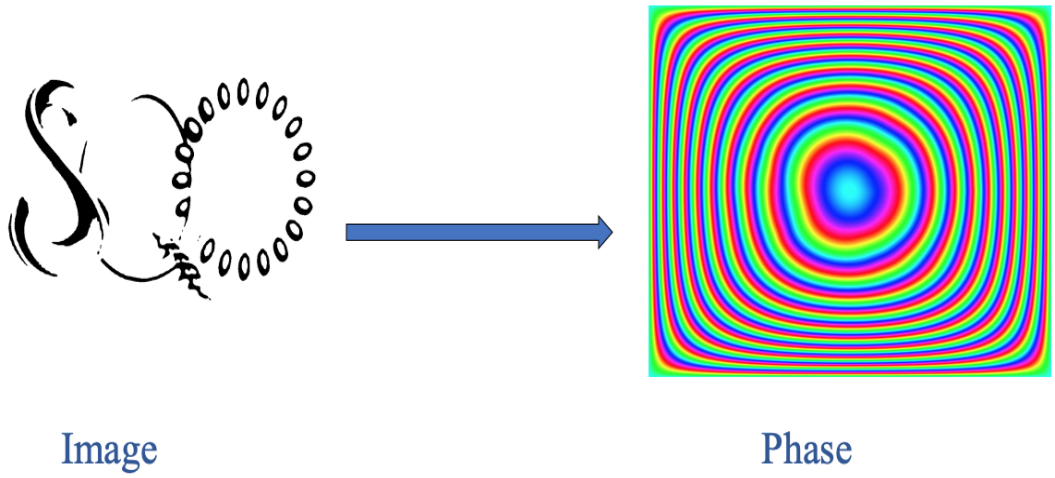

Figure 4.10: Calculated phase for an image of the SQO group using the Laplace transforms.

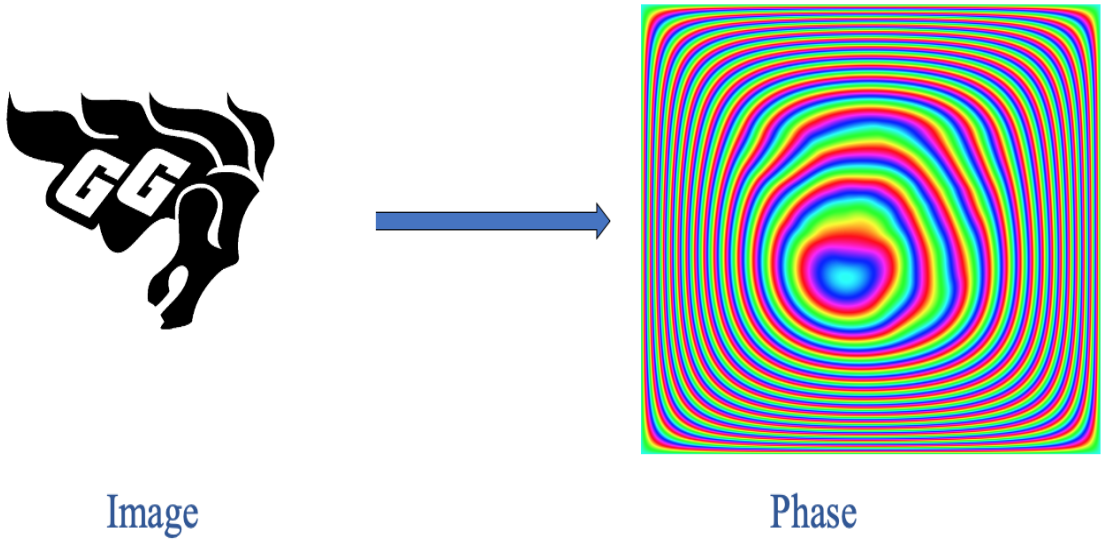

Figure 4.11: Calculated phase for generating the image of Gee-Gees logo in magic mirror.

In Figures 4.10 and 4.11, we plot the calculated phase pattern using Laplace transformations for the image of our research group logo SQO and Gee-Gees logo of the University

of Ottawa. We then loaded the phase patterns on the SLM and recorded images of the beam at different propagation distances by means of a translation stage and a CCD camera. The translation stage, which has only one direction of motion, was connected to the motion controller (XPS-C8, Newport) and a personal computer and was controlled with a LabView program. The LabView program is designed to record the image at the first position and then moved to the consecutive position, and so on. This entire process is automated through our Labview program. The images recorded are compiled as a video that included 191 frames. Only a small subset of the recorded images is presented in the results section.

This section discusses the stages of design and adjustments as the project proceeded. We spend time calculating the proper phase for our experiment. We want to test the adequate distance to see the image in a volume and not in a given plane. We experimented with lenses with different focal lengths to determine which lens would produce a good image resolution as we moved the camera on an automatic translational stage. Also, during the experiment, Santec SLM was used, and the data were collected, but this attempt was unsuccessful due to the poor resolutions; it has a lot of unwanted fringes. Additionally, we tried to observe the image without grating, which is seen only in 20% of signal images and 80% of noise. Grating on top of the image sent the deformed beam in a specific direction. Then, we planned to put a phase pattern and add grating on top of it. This was conducted because we had astigmatisms on SLM, and astigmatisms distort the intensity patterns.

4.5 Results

Figures 4.14 and 4.15 show the intensity images recorded by the CCD camera at different propagation distances for the SQO group and Gee-Gees logos, respectively. Intensity patterns at different distances were recorded and observed. The distance between each image is 250 microns. When the camera is moved away from the focus, due to the diffraction

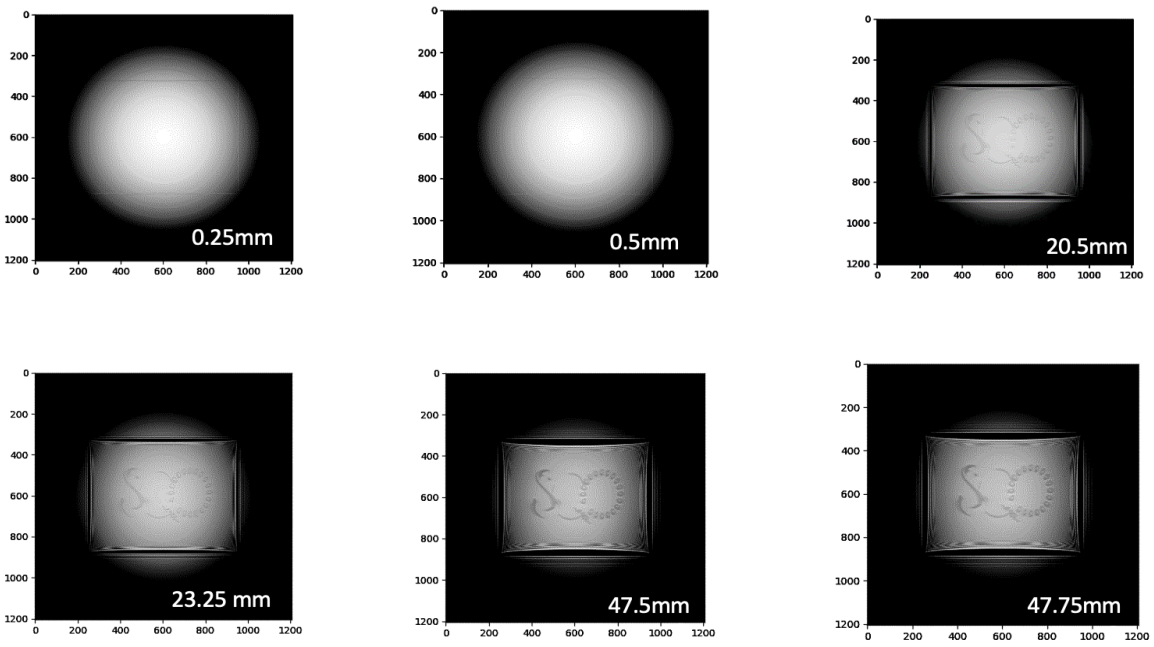

Figure 4.12: Numerical simulation of the SQO group logo image generated by the Laplace transform of the pattern phase.

of light, the image becomes less sharp, but still recognizable, which can be explained in terms of the Fresnel propagator. Diffraction grating is used in the setup, and was added on top of the magic mirror phase in order to sift the unwanted imperfection in the phase modulation. The use of grating causes the desired beam (magic pattern) to be diffracted at the first order of diffraction.

Figures 4.12 and 4.13 shows the theoretical results based on numerical simulation shown in section (4.3). Figures 4.14 and 4.15 shows the experimental results.

The image is recorded at various planes, once the light reflects from a SLM to go through a pinhole behind a 4-f system. The intensity is recorded from the minimum point of Z (first image on figure 4.13-4.14) to its maximum (last image on figure 4.13-4.14). It is noted that in all Z readings, the image appears to have generated phase patterns on a computer, which showed that the image was very sharp at a plane, and less sharp at another one. In essence, the image will still exist within the volume of sight range from 0.25 mm up to 0.47 mm.

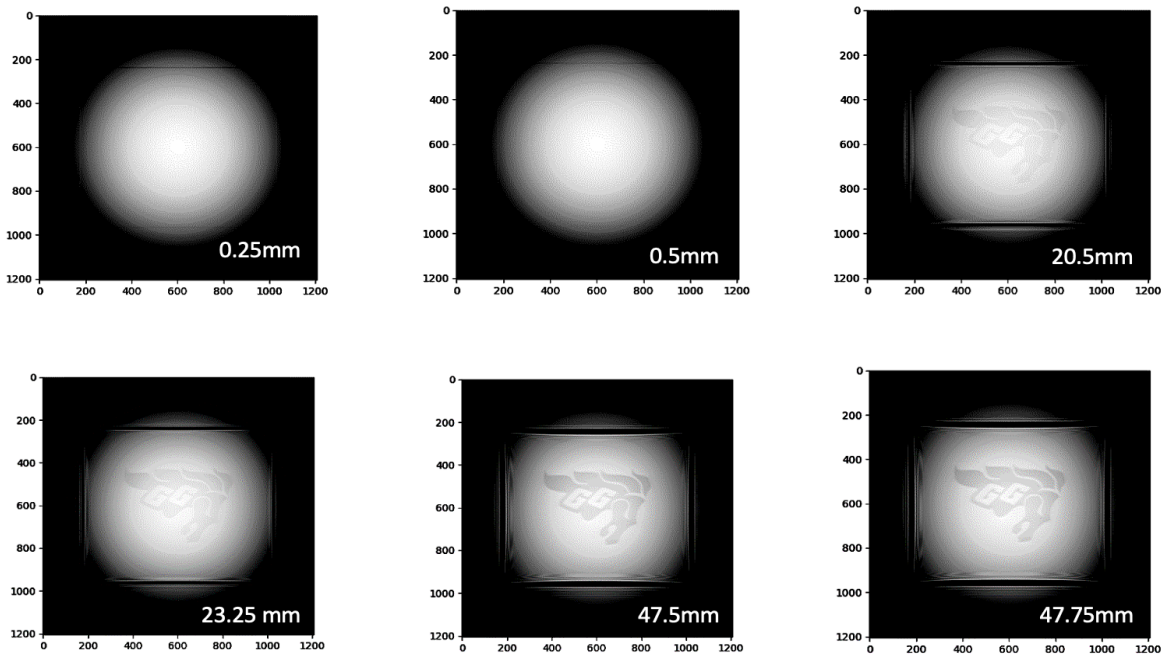

Figure 4.13: Numerical simulation of Gee-Gees logo generated by the Laplace transform of the pattern phase.

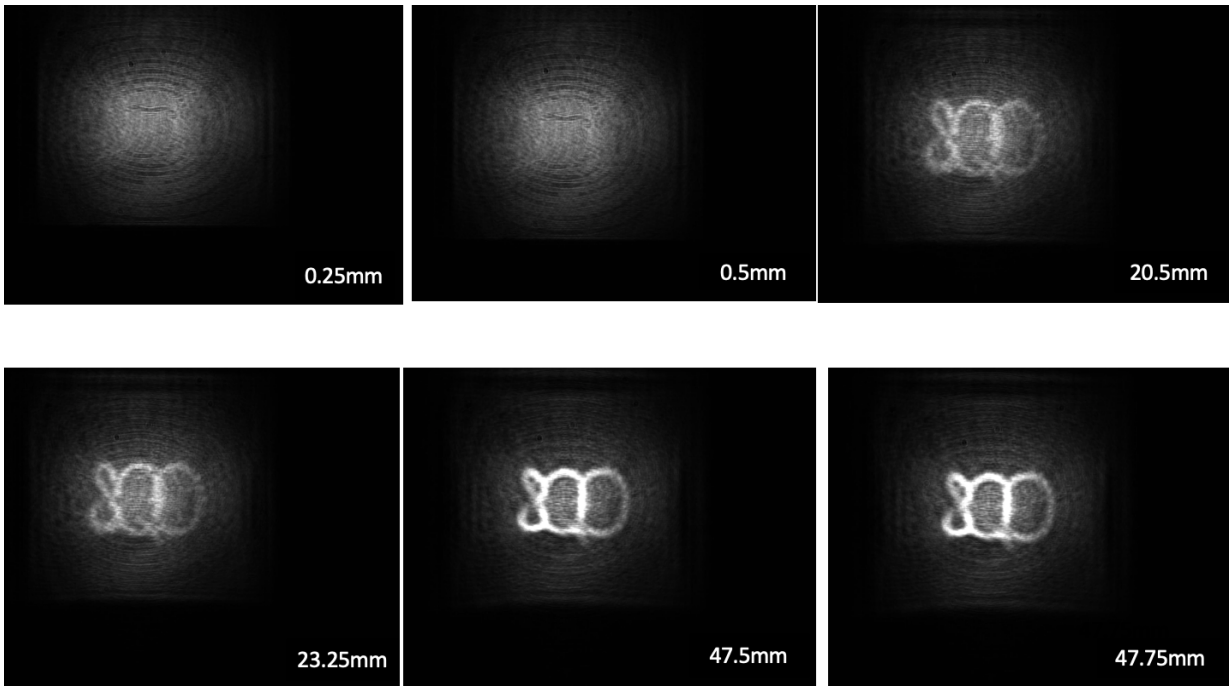

Figure 4.14: Experimental results for the SQO logo. Images were taken at different distances from the CCD camera. As shown, the image appears immediately, and is not (significantly) affected by the free-space propagation.

.

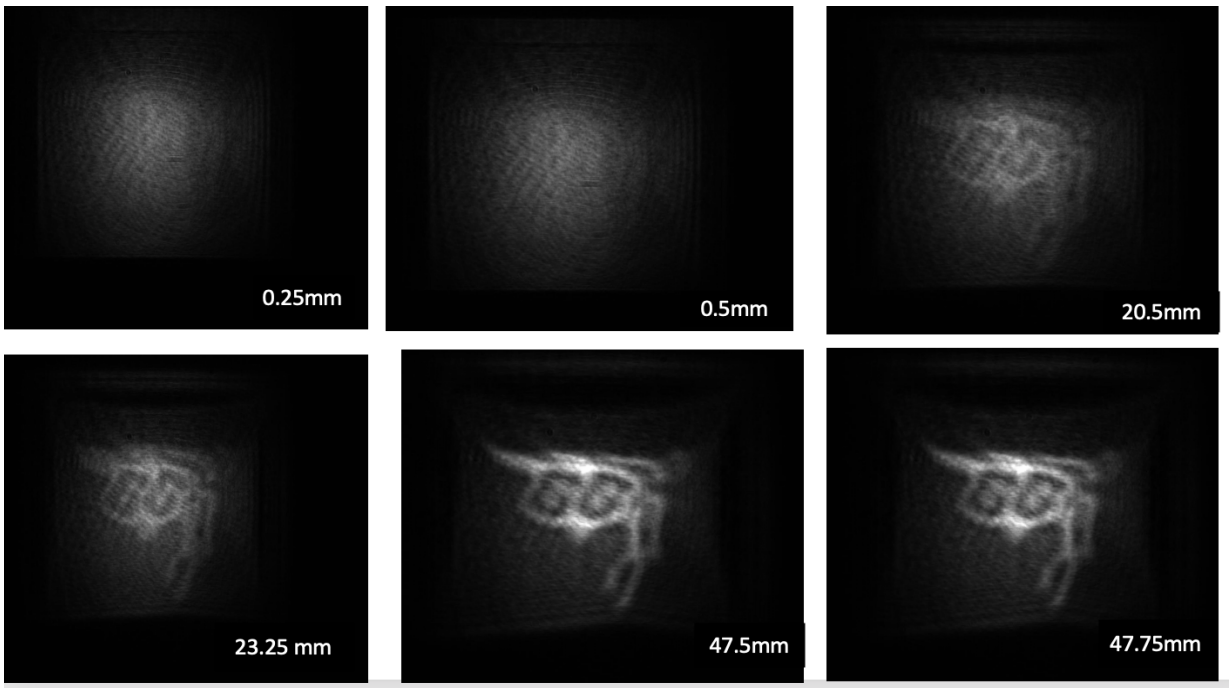

Figure 4.15: Experimental results for the Gee-Gees logo. Images were taken at different distances from the CCD camera. The image appears immediately, and is not significantly affected by the free-space propagation.

Caustics are the ray of reflection or transmission from a surved surface that has patterns. When we have a surved surface, and the light comes and gets reflected, finally, we will see a pattern. Then, we will have an envelope of rays tracing it and these rays are called caustics. In this research, the aperture is not used to reduce caustics. Due to the gentle nature of phase variation, the deviation of rays is minimal, and the caustics are minimized. Such a result took place spontaneously with Sir Michael Berry, who founded and pointed out this issue in his papers [13].

The fabrication of the magic plate, which is part of the next steps following this project, had multiple challenges. We have already made some attempts to the fabrication of the magic plate, however, we still face many challenges. These challenges mainly revolve around redesigning the hologram of the phase pattern to accommodate for the physical changes resulting from using a different type of LC device. These changes include changes in resolution and diffraction of light when propagating through the magic plate. All of

these will introduce imperfections in the formed image.

Chapter 5

Quantum Communication through a Vortex Fibre

In this chapter, we explore the application of the q-plate in quantum communication. In our experiment, we performed a proof-of-principle experiment to investigate the simultaneous use of a photon's SAM and OAM, generated using a q-plate, in QKD using the BB84 protocol through an OAM maintaining vortex fibre. We also present our method and results.

5.1 Quantum Key Distribution

To have a perfectly clear, and a secure quantum cryptography broadcast of information among multiple stations, it is fundamental to assume the full appliance of quantum physics. [43]. Ostensibly, until today, it is taken that quantum key distribution (QKD)[10] is the far-most dissected quantum cryptographic protocol, as it has being utilized in several areas such as quantum currency [117] and quantum secret sharing [18, 51].

Cryptography is the practice of encrypting and decrypting data sent between two nodes and forms the basis of modern information security. The key principles of cryptography

are encryption and decryption, entity authentication, and message authentication. Current encryption techniques are based on solving complex mathematical problems (e.g., finding large prime numbers). These classical encryption/decryption methods are not secure in the face of quantum computers. Quantum computers speed up computational tasks by orders of magnitude, dramatically outperforming classical computers. Thus, a novel cryptography technique is needed; quantum cryptography, which is based on the laws of quantum physics, has been proposed as the solution. Quantum cryptography, which allows users to share secure keys through quantum channels, it will be used in feature for commercial applications of quantum communication.

According to Wiesner [117], classical physics is not able to match the achievements of quantum physics, such as, bank notes production, as they contain unique serial numbers and each one of them has isolated two state. Therefore, bank has two bases and each bases has two states. At the bank registered all polarization and related serial number will print then on the bank note will print the serial number but the polarization remains hidden[115]. In 1984, Charles Bennet and Gilles Brassard, following Wiesner's Conjugate Coding idea, published the first protocol, referred to as BB84 for quantum key distribution. Currently, quantum cryptography has many applications in theoretical and experimental physics, as well as in mathematics and computer science [122].

One example of the quantum cryptography is Quantum Key Distribution (QKD) [9]. It is a secure communication method that is based on the laws of quantum mechanics to establish encrypted keys sharing between two parties, commonly referred to as Alice and Bob [31, 71]. Quantum Key Distribution (QKD) can be carried out via different protocols such as the BB84 [9], the Eckert 91 [37], and the Singapore protocols [38]. Alice and Bob transmit quantum information via various channels in these protocols, e.g., through fibre networks [111], free-space [82, 24, 91, 102], or ground-to-satellite links [121, 20]. Third parties that try to get access to quantum channel, and consequently the secure key, are called eavesdroppers (Eve). Eve is an attacker that attempts to access the quantum channel

and tries to measure the state which will introduce noise to the quantum channel, and it is about to be clear that the message has been intercepted. Therefore, the theory of the quantum mechanics is very useful to make the key very secure. In communication, and particularly in quantum communication, photons, the quanta of light, are used for communication. Alice encodes the information onto photon's state and sends it to Bob. Any attempt to read the photon quantum state, will change the quantum state and thus will introduce errors onto the encoded information. Within a certain error threshold, which depends on the used protocols, Alice and Bob can use privacy amplification and share secure information [11, 18].

Quantum channels are the ones that are used to transmit quantum information. In our case, the vortex fibre is the quantum channel, when we assume quantum channel in theory identity matrix, if a quantum state sends through the vortex fibre, it will not be affected by the quantum channel. Also, vortex fibres are designed to be polarization and OAM maintaining and thus are not very sensitive to stresses in the fiber caused by bending or temperature changes. Any small changes in the transmitted mode due to stress or imperfections in the fiber will just increase the QKD error rate.

Utilizing the vortex fibre as a quantum channel is different from the standard step-index fibre. The vortex fibre is a unique fibre having a ring of higher refractive index towards the edge in its transverse profile, which preserves the photon's OAM, as its profile imitates the OAM mimics modes. Our colleagues from Boston University have manufactured this vortex fibre, and we have performed the experiment in our laboratory. The unique property of this vortex fibre is that it supports OAM $\ell = \pm 1$. Also, its ability to separates the effective refractive index of the vector modes. Not only, it is very important to separate the mode to reduce the crosstalk between the mode and to reduce the high error rate, but also, that mode imperatively should be coherent with propagation considering the mode‘s superposition. Thus, a standard step-index fibre is not recommended for quantum transmitting, the various modes will be disjoined during propagation. Also, quantum channels, are just like

classical channels, as they face certain challenges, such as, limited capacity of transmitting information. Photons have a different degree of freedom, such as polarization, time-bin, frequency, and orbital angular momentum (OAM) that can be used to encode information. The OAM degree of freedom is used, since it has the advantage of its unbounded thereby, allowing more information encoding per photon. In addition, upon the encoding occurrence in higher dimensions, the OKD noise tolerance increases[102]. Moreover, the combination of OAM and polarization thus performs an imperative function in quantum communication enhancing both the security threshold in quantum key distribution and the amount of information encoded.

It has become a pressing matter to develop secure quantum communication infrastructures since the world has ranked information, communication, and confidentiality, of supreme privacy values. However, most quantum cryptographic systems generated are based on dual-dimensional encoding designs, parallel to classical bits, identified as (qubits). The classical bits have a state of ones or zeros, while quantum bit (qubit) has superposition one and zero. Qubits, as a physical application, can take various shapes, such as photon polarization [8], light orbital angular momentum [20], and several physical quantities. This research will utilize the quantum key distribution using the BB84 protocol, in which the photon's orbital angular momentum and polarization are used as the qubits. Here, in this chapter, we experimentally investigate the use of photon's spin and orbital angular momenta in encoding information sent through a fibre channel. Clearly, using these photonic degrees of freedom together would expand the communication alphabet, consequently, allowing to share more information per carrier, encroaching a bit of information per carrier. For instance, spatially structured photons, photons that are in coherent superposition of different spin angular momentum (SAM) and (OAM) degrees of freedom, can be used for high-dimensional quantum encryption techniques[103, 96].

5.2 BB84 Protocol

The BB84 protocol has been introduced by Bennett and Brassard in 1984 [9]. In the original BB84 protocol polarization of a single photon was suggested to encode information. Photon polarization can be in superposition of two independent states, and thus it can be described by the SU(2) group representation. For instance, the eigenstates of σ_x stands for horizontal and vertical linear polarization, the eigenstates of σ_y stands for diagonal and antidiagonal linear polarization. Alice randomly picks up one of these operators, and prepares one of their eigenstates. So, she either selects σ_x and generates a photon state with horizontal or vertical polarization $\{|H\rangle, |V\rangle\}$, or states σ_y and generates a photon with diagonal or antidiagonal polarization states $\{|A\rangle, |D\rangle\}$. Alice assigns a bit of information to these eigenstates, i.e. 0 to horizontal and 1 to vertical, and 0 diagonal and 1 to antidiagonal state, respectively. Certain polarization basis is randomly selected from any of these two bases, i.e., horizontal - vertical or diagonal - anti-diagonal. The photons are then sent to Bob through a quantum channel. Bob without knowing the Alice's choice of basis and the encoded bit (he does not know which basis σ_x and σ_y and which polarization states are chosen by Alice) randomly selects the polarization basis and performs a measurement on the polarization state. Whenever Bob chooses the correct base (σ_x or σ_y) the outcome of the measurement is what Alice had chosen, and whenever Bob's choice of measurement base is wrong the probabilistic nature of the quantum state dictates a 50-50 chances for the detection of eigenstates, i.e., encoded information. Note that Eve, the eavesdropper, has access to the quantum channel all time. After Bob's measurements, using a reliable public channel, Bob and Alice discuss the basis which each one of them selected. If they have the same basis, without revealing the measurement outcome, they will keep the information otherwise they discard the information. Alice and Bob do the above procedure for a very long set of photons, and thus the probability of Bob choosing the correct base of measurement is 50%. This means that half of the photons'

information, due to the lack of base knowledge by Bob will be discarded. This is known as sifting. In practice, all laboratory experiments have errors, which might arise from the imperfection in generation and detection techniques. Therefore, even when Bob choice of basis is correct the outcome of the measurement might not be what Alice had chosen. In order to account for this and knowing the amount of error in the quantum communication channel, Alice and Bob publicly share the outcome of their measurements for a portion of their sifted photons. This will give the error introduced to the channel, which is known as Quantum Bit Error Rate, and follow a classical procedure to account and correct for the introduced for the error, known as privacy amplification. Privacy amplification which can be defined an increase in the security of communications and reduction in the error rate. The secret key rate is R for high-dimensional QKD system is $R = \log_2(d) - 2\,h(e_b)$. Here e_b is the quantum bit error rate (QBER), d is the dimensional e.g: 2, 4,....etc, $h(x)$ is the Shannon entropy (for high-dimensional space), which calculated through the following formula $h(x) = -x\log_2(\frac{x}{d-1}) - (1-x)\log_2(1-x)$. The Shannon entropy is detected if it is doing enough state measurement work and less error registration, but it is also defined by mutual information on the system (between Alice-Bob and Alice-Eve). The threshold is dependent on the dimensionality of space in a positive correlation. In other words, as the communication space dimension increases, the error threshold increases. Only then, it is conceivable to send more information and tolerate more errors. The security proof is derived from the amount of information that Eve and Alice must share is higher than the amount of information that Bob and Alice must share. Information willing to be shared by Alice-Eve is being monitored, due to Eve's attacking the channel, and due to the portion of information Eve will capture, once Alice shares with Bob. In due course, inspection shifts towards information available with Alice-Bob to assess if the amount is higher than the amount Alice and Eve have or not, signifying whether the channel is secure or not.

Note that for a two dimensional quantum state, qubit encryption, this error cannot be higher than 11%. The number of secret key bits per sifted photon, described as the secret

key rate R, is indicated by the following expression [18]

$$R = 1 - 2\,h(e_b), \tag{5.1}$$

where e_b is the quantum bit error rate (QBER), $h(x)$ is the Shannon entropy and is $h(x) = -x\log_2(x) - (1-x)\log_2(1-x)$. Shannon entropy is important as apart of the sifting process. The secret key rate for QBER higher than 0.11, i.e. $e_b > 0.11$, is negative, which is the threshold on the error for two dimensional BB84 protocol that we have just mentioned. The secret key rate for QBER lower than 0.11, i.e. $e_b < 0.11$, is positive, which is below the security threshold for the BB84 protocol in 2 dimensions.

Alice and Bob after the sifting process check the QBER. Any errors, even due to experimental imperfections, is assigned to the presence of an eavesdropper. If the QBER is large, and in the case of two-dimensional QKD higher than 0.11, it then means that Eve attacked in the channel and the information is not secure (no positive secret key). Thus, it means that Alice and Bob must start the procedure from the scratch. If the QBER is low, classical privacy amplification is used to remove the noise, and then they can establish a secure key [18, 71].

5.3 QKD through Quantum Channel: Vortex Fibre

Optical fibres, single and multimode fibres, are optical elements that have different refractive indices across their cross section. The light propagates through the fibre core that has a slightly higher refractive index compared to the cladding. In both single-mode and multimode optical fibres, the core is a very long cylinder (reaches to several kilometers) with a radius of a few (or tenths) of micrometers (for visible light). In contrast, the vortex fibre, which is a special fibre, has a ring of higher refractive index towards the edge in its transverse profile. The radial change in the refractive index of the vortex fibre allows it

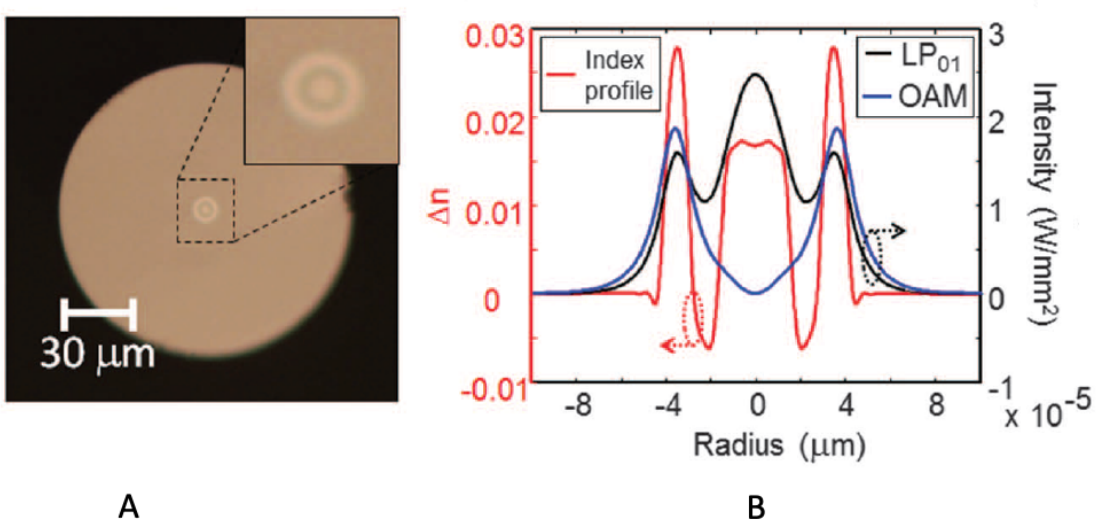

Figure 5.1: A) Introduces a microscopic 30 micrometer scale photo of the vortex fibre. B) Shows refractive index profile of the vortex fibre matching the OAM refractive index profile shape.The core radius is 3 micrometer and outer ring is 125 micrometer [22].

to support desired optical modes. The distance from the center of the fibre (in the fibre cross section) which the refractive index is changed and becomes higher than the center and the periphery corresponds to the intensity profile of the OAM supported by the fibre. In other words, the key idea of this fibre is the difference of refractive index, which makes OAM-carrying beams propagate stable, as seen in Figure 5.1.

The vortex fibre is designed to support the propagation of optical vortex modes that have been created with the underlying assumption that free-space OAM-carrying beams are adequate for fibre coupling. This assumption has traditionally been justified because of the similarity in mode amplitude, polarization and phase distribution between free-space OAM modes and their corresponding fibre modes. However, some crucial distinctions between the two can prevent the creation of the required fibre modes from free-space OAM modes. One such distinction is the existence of vortex modes as degenerate pairs in a fibre which can get mixed very easily despite the fibre being designed for stable propagation of the separate OAM orders. A device that can create an arbitrary linear combination of

any pair of degenerate states and allow for the dynamic high-speed manipulation of this combination, which can solve this issue as this will disentangle the birefringence induced OAM mixing effects in the fibre. The work by Gregg *et al.*(2015) establishes that q-plate devices for free space vortex mode creation in conjunction with polarization controllers and a pair of quarter-wave plates offer this functionality. The eigenmodes of a fibre can be represented by the combination of a radial function, a helical phase term containing the OAM (ℓ) carried by the photon mode and the polarization state ($\hat{\sigma}^{\pm} = (x \pm iy)/\sqrt{2}$). The modes with orbital and spin angular momentum along the same direction are degenerate in wave vector with each other, and so are the modes where the orbital and spin angular momentua along opposite directions. But, in contrast to the free-space modes, these two sets of modes are not degenerate with each other. Two immediate exceptions to this criterion are available. One is in the case of the fundamental $\ell = 0$ mode, which has only two degenerate polarization modes. The second is in the case of the $|\ell| = 1$ mode where linear combination of TE and TM modes exist instead of the anti-aligned spin and angular momentum modes with a total angular momentum of 0. These TE and TM modes are not degenerate with each other. In the case of $|\ell| = 1$, the available modes can therefore be written as following

$$\begin{aligned}
\mathrm{OAM}^{\pm}_{1m} &= (\hat{\sigma}^{\pm}\, e^{\pm i\varphi})\, F_m(r) e^{i\beta_{\mathrm{OAM}}\, z}, \\
\mathrm{TE}_{0m} &= (\hat{\sigma}^{+}\, e^{-i\varphi} - \hat{\sigma}^{-}\, e^{+i\varphi})\, \frac{F_m(r)}{i\sqrt{2}} e^{i\beta_{\mathrm{TE}}\, z}, \\
\mathrm{TM}_{0m} &= (\hat{\sigma}^{+}\, e^{-i\varphi} + \hat{\sigma}^{-}\, e^{+i\varphi})\, \frac{F_m(r)}{\sqrt{2}} e^{i\beta_{\mathrm{TE}}\, z}.
\end{aligned} \tag{5.2}$$

Here, F_m denotes the radial field distribution and m denotes the radial mode order. Fibres that support OAM are very different from the conventional fibres because they allow adequate wave vector, β, splitting. This is important in allowing propagation of the three modes classes shown above in a stable manner. For the fibre used in this case, $m = 1$ everywhere. It is important to note that the modes of $\mathrm{OAM}^{\pm}$ are degenerate, and therefore

when linearly combined they will remain as modes and form an OAM$^{\pm}$ subspace which is similar to the elliptical polarizations subspace for free space or fibre with the ℓ=0 mode. It has also been proven that for ℓ=0, mode can be made from birefringence by fibre loops. Nevertheless, while on one hand simple free-space wave plates are capable of offering a similar functionality for the fundamental mode, other techniques used in OAM-based fibre experiments such as spiral phase plates are not capable of enabling straightforward production of general linear combinations for fibre OAM states. In such a case, the functionality can be provided by q-plates which facilitate the coupling of the spin and orbital angular momenta. The linear transformation performed by a q-plate of topological charge q can be written as

$$q\text{-plate} \cdot (A\,\hat{\sigma}^{+} + B\,\hat{\sigma}^{-}) = A\,\hat{\sigma}^{-}\,e^{2iq\varphi} + B\,\hat{\sigma}^{+}\,e^{-2iq\varphi}. \tag{5.3}$$

This means that the OAM imparted by the q-plate is $2q$, and its sign dependent on the incoming beam's polarization state. With the right choice of A and B along with a $q = -1/2$, any state that is the linear combination of the OAM$^{\pm}$ modes can be created. A $q = 1/2$ plate followed by a half-wave plate with a linear polarization as the input can be used to create a TE/TM mode. The latter can also be achieved using a combination of $q = -1/2$ plate and a half-wave plate. Lastly, turning the q-plates bias to obtain λ retardation can help achieve fundamental mode excitation. This means that two wave plates and a q-pate are sufficient to generate all the linear combinations $|\ell|$=0,1 fibre modes.

Gregg *et al.*(2015) used a laser beam that is passed through a commercial in-fibre electronic polcon(polarization controller) to generate the input polarization state that is required for the q-plate. A 50/50 beam splitter is used to sample the light for interference measurements to obtain the phase of the output beams. A combination of two quarter-wave plates was used to create a half-wave plate whose state can be changed by aligning or crossing the axes of the constituent wave plates. The output of this is then fed through a 300 m long fibre, the length of which was chosen to enable time domain measurements.

Two types of measurements were performed on the output of the fibre. One measurement is the interference of the beam after sorting for the circular polarization with the reference beam to reveal the phase and the other is direct detection using a high bandwidth detector to enable time domain measurements.

The polarization sorting and interference measurements performed on the CW laser can be summarized as follows: for the $\ell = 0$ mode, the interference patterns look the same regardless of the polarization. For the OAM$^{\pm}$ states on the $|\ell|$=0 mode, the expected bright ring on one of the polarizations is obtained. Also, the TE/TM modes show two equally bright rings for each of the polarizations as predicted. The phase structure of the OAM$^{\pm}$ shows a one-armed spiral structure with the handedness expected from the polarization. The TE/TM phase structure also are in the form of one-armed spirals anti-aligned with the polarizations. The constituent OAMs in TE mode are π out of phase as expected from the predictions in the above forms.

To investigate this effect further, they have used a pulsed 1530 nm laser was used as the source and performed measurements in time-domain. Since the modes listed above (except for the degenerate modes) differ in their group velocities, the delay in their propagation through the fibre can be measured using a fast detector. All possible modes of the fibre can be excited with an intentional misalignment of the fibre but, when the fibre is aligned, select modes can be excited and the multi-path interference can be calculated as follows

$$\mathrm{MPI} = 100 \log_{10} \left(\frac{P_{\mathrm{peak,j}} - P_{\mathrm{noise}}}{P_{\mathrm{peak,k}} - P_{\mathrm{noise}}} \right), \tag{5.4}$$

where the expression uses the peak power in the mode $P_{\mathrm{peak,k}}$ and the average noise power P_{noise}. Measurement of MPI shows a purity of at least -18dB for the different modes excited in the fibre. This shows that any of the modes in equations (5.2) can be excited in the fibre with high fidelity using the scheme. When a circular polarization is fed to the input of the of a $q = -1/2$-plate (a $q = -1/2$-plate followed by a half-wave plate), and then

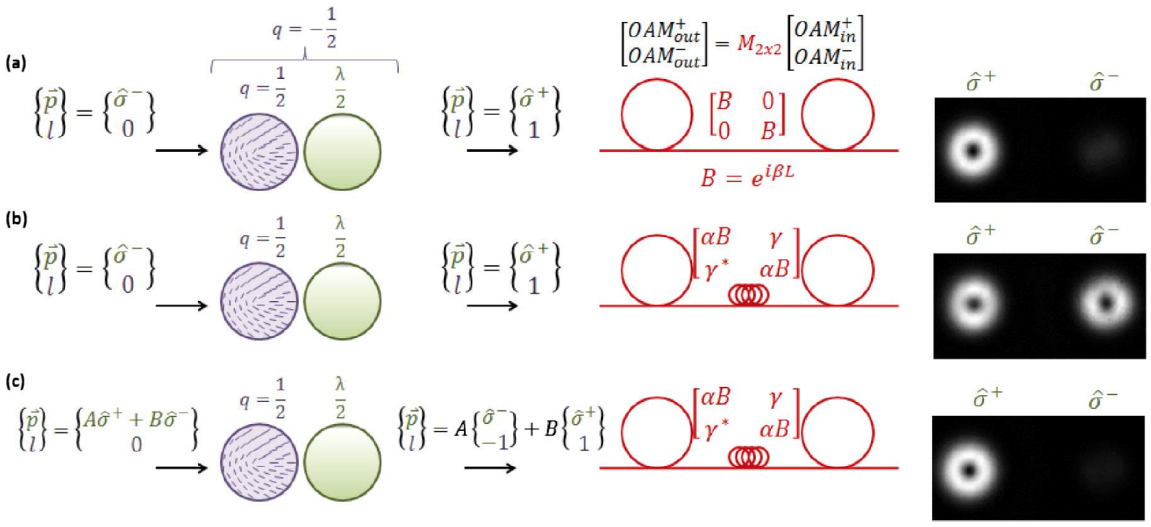

Figure 5.2: The image present generation of OAM carrying beams, using q-plate and half wave plate, and their propagation through vortex fibres. a) Pure OAM states, b) combination of the OAM$^{\pm}$ states c) OAM states (tuning input polarization) [44].

coupled to an unperturbed fibre, it acts as a diagonal unitary matrix in the OAM$^{\pm}$ with no coupling between the OAM^{+} and OAM^{-} states giving a pure OAM state as the output as shown in Figure. 5.2 a. Perturbations such as bending or twisting of the fibre results in the matrix no longer remaining diagonal. This leads to the production of an arbitrary linear combination of the OAM$^{\pm}$ states at the output as shown in Figure 5.2 b. This linear combination can be controlled by the ellipticity of the input beam. Since both the fibre and the q-plate span the same OAM$^{\pm}$ subspace, feeding a specific elliptical polarization into the fibre will result in the creation of a pure OAM$^{\pm}$ state at the output. Equation (5.2) suggests that each of the OAM state is associated with its own handedness of the circular polarization, thus, the creation of a mixed or pure OAM$^{\pm}$ state can be verified by looking at the power in each of the $\hat{\sigma}^{\pm}$ circular polarizations as shown in Figure 5.2 c. In summary, the work has shown that a combination of a q plate and polarization controlling optics can create all of the first radial vortex modes and their linear combinations in a fibre [44].

5.4 Experimental Method

In this section, we explain the polarization tomography, Stokes parameters measurement, and QKD experiment.

5.4.1 Polarization Tomography

We are performing characterization of the vortex fibre using stokes parameters and polarization tomography in order to examine if the vortex fibre is a good channel and it supports vector vortex mode. Alice generates the vortex vector modes and before sending to Bob, she must check the quality of modes. Then, she sends the mode via fibre and polarization tomography is performed on Bob's side using a combination of half- wave plate (HWP), quarter- wave plate (QWP), and a polarizing beam splitter (PBS).

Let χ and ψ be the orientations of HWP and QWP. By rotating the angles χ and ψ, we can project into different polarization states, for instance, if χ and ψ values are zero, no changes are made to the polarization state and only H polarized photons are allowed to pass through the PBS, thus we project onto the H polarization. The table 5.1 lists the orientation of HWP and QWP in conjunction with their corresponding polarization states.

Generation the state	QWP(χ)	HWP(ψ)
$\|H\rangle$	0	0
$\|V\rangle$	0	45
$\|A\rangle$	0	-22.5
$\|D\rangle$	0	22.5
$\|R\rangle$	45	0
$\|L\rangle$	-45	0

Table 5.1: This table shows the orientation of HWP and QWP and their corresponding generation polarization states. HWP is half-wave plate and QWP is quarter-wave plate.

An image showing the intensity profile for each of the six polarization bases must first be taken using the same experimental conditions e.g., the same integration time. Thus the

ratio between the intensities of each pixel from the six images will give the contribution of each polarization at every pixel. The camera identifies the intensity profiles. For each pixel (i,j), there are intensity profiles. The Stokes parameters are calculated through the following equations for each pixel

$$\begin{aligned} S_1^{ij} &= I_H^{ij} - I_V^{ij}, \\ S_2^{ij} &= I_D^{ij} - I_A^{ij}, \\ S_3^{ij} &= I_L^{ij} - I_R^{ij}. \end{aligned} \tag{5.5}$$

From these profiles, in other words, a set of measurements, it is conceivable to plot the polarization ellipse point by point. Since there are six values (associated with six measurements) for each pixel, it is possible to drive the Stokes parameters for each pixel. At this point, it is conceivable to plot the polarization ellipse from each pixel point by point utilizing equations 1.22, 1.23, and 1.25. The orientation of the polarization ellipse and ellipticity for each pixel can be calculated from the Stokes parameters

$$\psi^{ij} = \frac{1}{2} tan^{-1}\left(\frac{S_1^{ij}}{S_1^{ij}}\right). \tag{5.6}$$

$$\chi^{ij} = \frac{1}{2} tan^{-1}\left(\frac{S_3^{ji}}{\sqrt{S^{ji}{}_1^2 + S^{ji}{}_2^2}}\right). \tag{5.7}$$

5.4.2 Spontaneous Parametric Down Conversion (SPDC)

The most common way to generate entangled photon pairs is through spontaneous parametric down conversion (SPDC). SPDC was experimentally initiated by Burnham and Weinberg in 1970 [23], and carried forward by several theoretical studies up to the 90s. The process can be elucidated as in the splitting of a high frequency pump photon into

two photons of lower frequency, called the signal and the idler and has the energy and momentum as shown in Figure 5.3. The energy and momentum conservation are referred to as the phase-matching condition

$$\omega_p = \omega_s + \omega_i, \tag{5.8}$$

$$\vec{\kappa}_p = \vec{\kappa}_s + \vec{\kappa}_i, \tag{5.9}$$

where ω_p, ω_s , ω_i, κ_p, κ_s, κ_i are the frequencies and wave vectors of the pump, signal and idler photons respectively. Due to the conservation laws many of the photon's degrees of freedom such as energy, time, position, momentum, SAM and OAM are either entangled or strongly correlated.

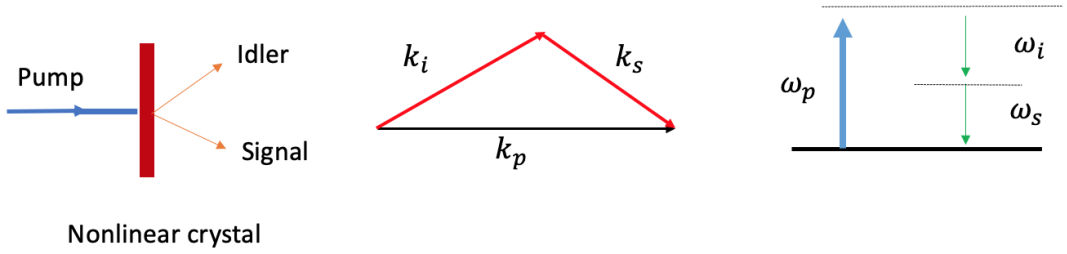

Figure 5.3: A) The image represents the SPDC process. When input pump laser pass thought nonlinear crystal, it will split the photon idler and signal. B) The drawing shows in this process, the energy and momentum conserved. C) The drawing shows one photon absorption and two photons creation at a lower frequency.

This phenomenon was coincidentally discovered during counting experiments, and in more recent times, the resolved correlation measurements of the same process have been detected. Hamiltonian that describes the SPDC process is written as

$$\hat{H}_{SPDC} = i\hbar k(\hat{a}_i\hat{a}_s\hat{a}_p{}^{\dagger}e^{i\Delta\vec{k}-i\Delta\omega.t} + \hat{a}_i{}^{\dagger}\hat{a}_s{}^{\dagger}\hat{a}_p e^{-i\Delta\vec{k}\vec{r}+i\Delta\omega.t}) \tag{5.10}$$

The first part of the Hamiltonian representing second harmonic generation occur under this condition $(\omega_i) = 2(\omega_s)$. At this point, two photons are absorbed, and one photon is created. These two photons have the same frequency with degenerate case. The output phone has twice frequency of incoming photon. The second part of the Hamiltonian representing SPDC, shows that one photon is absorbed, and two photons are created (ω_i) as well as (ω_s) at different frequency with non-degenerate case. The output photons has different frequency of incoming photon.

5.4.3 Avalanche Photodiodes Detector(APD)

The detector receives the photon and creates an electron. If an incident photon is an absorber, it will create an electron and produce an electrical signal (TTL). The electrical signal has a specific voltage and has specific a duration time of 40 ns. APD is sensitive to single photons and has a quantum efficiency between 50 % to 60 % depending on wavelength of the incoming light.

5.4.4 Experimental Setup

In our experiment, we demonstrate BB84 QKD protocol using heralded single-photon pairs with spin-orbit degrees of freedom. The aforementioned single-photon pairs are generated via the process of spontaneous parametric down-conversion (SPDC), which was achieved by pumping a periodically poled potassium titanyl phosphate (ppKTP) nonlinear χ^2 crystal using a 405 nm diode laser (200 mW) and a series of lenses(of the focal length f=5cm, f=15cm, and f=10cm), then pass to D-mirror as shown in Figure 5.4, the Alice part. The ppKTP crystal converts a pump photon of wavelength $\lambda_p = 405$ nm into two photons known as the signal and idler photon with the signal at $\lambda_s = 775$ nm and idler at $\lambda_i = 850$ nm,

obeying the conservation of energy such that

$$\omega_p = \omega_s + \omega_i = \omega_{775} + \omega_{850}, \tag{5.11}$$

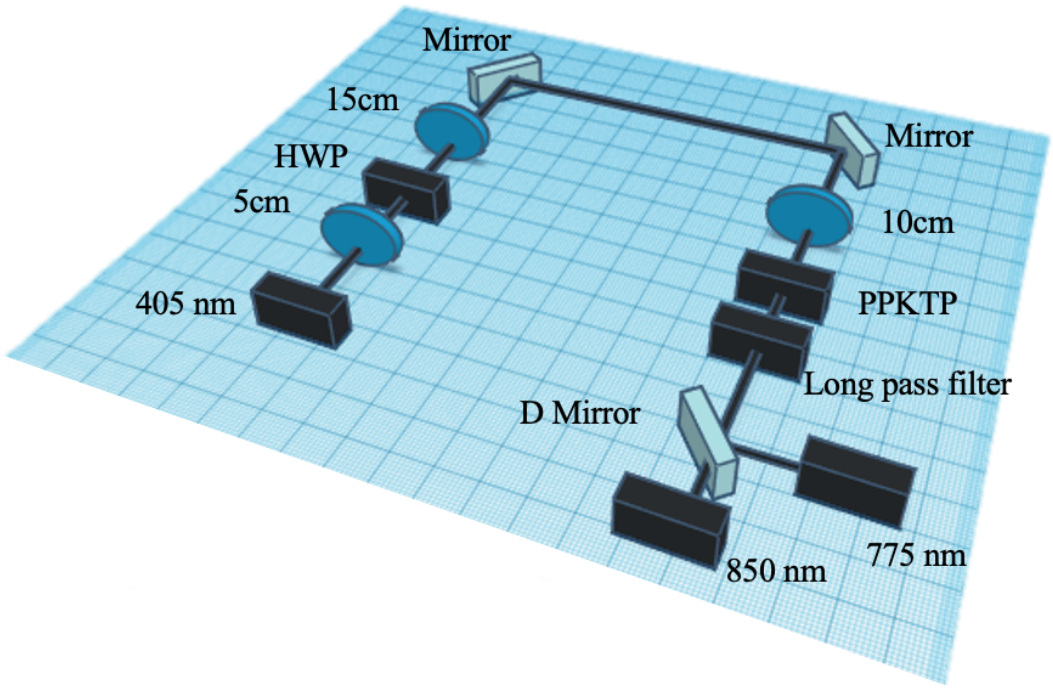

Figure 5.4: The image represent setup for spontaneous parametric down conversion (SPDC), pumping laser to periodically poled potassium titanyl phosphate (ppKTP) nonlinear χ^2 crystal using a 405 nm diode laser (200 mW) and series of lenses f=5cm, f=15cm, and f=10cm, then pass to D-mirror then one photon send to detector and another one send to Alice.

where ω_p, ω_s and ω_i are the frequencies of the pump, signal and idler photons respectively. The black line is a classical channel in which Alice and Bob share an idler photon. It will announce the proper moment to perform the measurement. The idler photon does not contain any piece of information. The correlations that are established through classical channels based on herald photons are defined as herald systems. The idler photon is sent to an avalanche photodiode detector (APD)- (D1) as shown in Figure 5.6, and it

is used to herald the detection of the signal photon by Bob. The Bob photon detected using avalanche photodiode detector (APD)-(D2) and it recorded the coincidence using a coincidence box to the coincidence counts (x mark). The counts are approximately 4500 coincidences per second, nevertheless, for a coincidence window is 5 ns and the dark count is less than 50 Hz.

The signal photons are then transmitted through a homemade monochromator, as shown in Figure 5.5. In the monochromator, using a combination of a diffraction grating and a lens (each with f=10cm), the spectrum of the signal photons is spatially separated at the focus of the lens. A moving slit with an adjustable slit width was used to select the appropriate wavelength and bandwidth required from the signal photons. Finally, the spectrum is recombined using a second lens followed by a diffraction grating. The signal photons are coupled into a single mode fibre (yellow line in Figure 5.6). The setup is then divided into three subsections. First is the generation stage, where Alice prepares the signal photons into "structured modes" (modes that are a combination of both OAM and SAM). In this experiment entangled photons were produced; however, they were not exploited in the entanglement measurement, only a single photon is used to trigger the others for measurement. Second is the quantum channel where the signal photons are transmitted through a vortex fibre, and lastly the detection stage where the signal photons are detected by Bob.

In the preparation stage, Alice prepares the photons randomly in one of the two mutually unbiased bases (MUBs). The two MUBs are

$$\begin{aligned} M_0 &= \{|L,1\rangle, |R,-1\rangle\} \\ M_1 &= \{(|L,1\rangle + |R,-1\rangle)/\sqrt{2},\ (|L,1\rangle - |R,-1\rangle)\sqrt{2}\}, \end{aligned} \tag{5.12}$$

where L and R corresponds to left- or right-handed circularly polarized states, respectively, and $\ell = \pm 1$ represents orbital angular momentum. These "structured modes" are generated

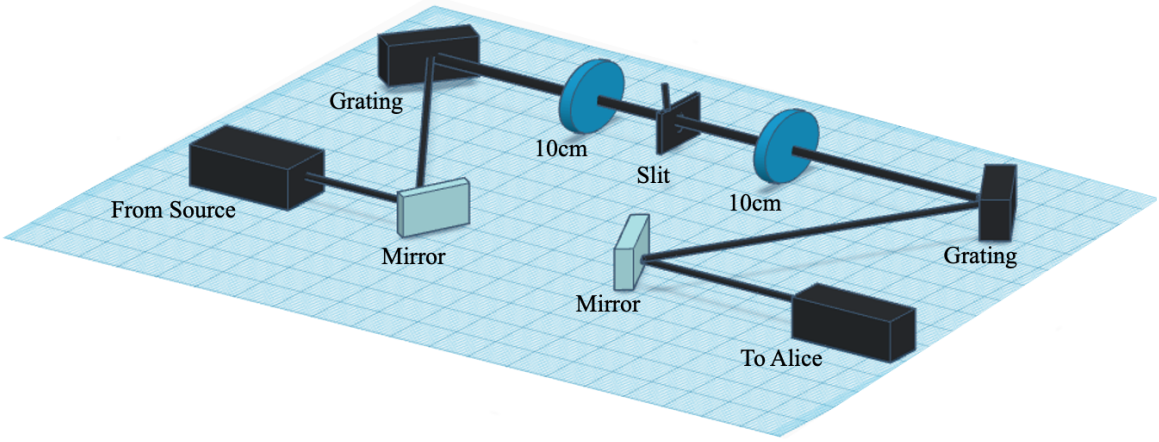

Figure 5.5: The image represents a homemade monochromator. The band pass filter has been built to consist of a laser that travels through the first grating. The spectrum of the signal photons, at this point, will be separated spatially at the focus of the lens(f=10cm). With an adjustable slight width, to determine the appropriate wavelength and bandwidth required from the signal photons, that spectrum, eventually, will be recombined through a second lens (f=10cm) followed by a diffraction grating.

using a combination of half wave plate (HWP), quarter wave plates(QWP), and q-plate. The table 5.2 represents the generation of four states and the orientation of the waveplates to generate each state for the MUBs that have been used in the laboratory. Adding the HWP at the end to create states that are aligned with SAM and OAM.

MUB	HWP	QWP	QP	HWP
M_0	45	45	QP	0
M_0	0	45	QP	0
M_1	0	0	QP	0
M_1	45	0	QP	0

Table 5.2: The experimental setup of generating the state for M_0 and M_1.

In our case, the quantum randomness (using random number generator) was not used since we studied the feasibility of performing a proof-of-principle QKD in a vortex fibre. In fact, this can be achieved by means of two random number generators and pockel cells,

which are commercially available. For instance, Bob can use a random number generator that provides two output signals. These signals can be used to control the bias of a pockel cell and turn the projection basis from H/V to A/D.

For example, on Alice side, the state is created either H, or V, and Bob performs the measurement on one of the states H or V. This setup will lead to the following scenarios. If Alice sends H, the wave plate orientation will be for H, and Bob will project on H, the orientation of the half wave plate and the quarter wave plate will be for H, indicating that Alice and Bob are at the same state, then the photon will pass through PBS producing a recordable photonic click on the D2 detector. If Alice sends H, the wave plate orientation will be for H, and Bob projects on V, the orientation of the half wave plate and the quarter wave plate will be for V, then the photon pass will not be through PBS, and will not produce a recordable photonic click on the D2 detector; therefore, no recording. If Alice sends H, the orientation of wave plate for H, and Bob projects on A, the orientation of the half wave plate and the quarter wave plate will be for A, then the photon will have the chance of a half probability to pass through PBS and produce a recordable photonic click on the D2 detector.

Alice sends the photon to the quantum channel. In the quantum channel, the transmitted modes in the vortex fibre is degenerated in time with respect to each other, if they have the same handedness for OAM and SAM, i.e., $|L, 1\rangle$ and $|R, -1\rangle$, else the states are temporally non-degenerate if they have opposite handedness, i.e. $|R, 1\rangle$ and $|L, -1\rangle$ [44], hence, why the above MUBs are used. The fibre coupling loss measurement is by placing the power meter at the fibre's facet and the end of it. Coupling losses into the vortex fibre are around 50%.

In the detection stage, Bob projected the single photons randomly between the two MUBs with another set of waveplates and q-plate mirroring Alice's setup. At the point when the MUB is selected by Bob, coinciding with the fact that it is send by Alice, perfect phase flattening was achieved. Phase flatting is a projection technique used to determine

the OAM value of an unknown beam. Perceived, that an OAM beam is with amplitude and phase $LG_{\ell p}e^{i\ell\varphi}$. The conjugate phase $e^{-i\ell\varphi}$ is imprinted onto the beam using q-plate and wave plate (or other OAM generation techniques). Thus, the phase of the incoming beam is flattened, and the state is $LG_{\ell p}$, which is coupled into a single-mode optical fibre. Acquiring all these elements, is through filling the density matrix with ensembled photons.

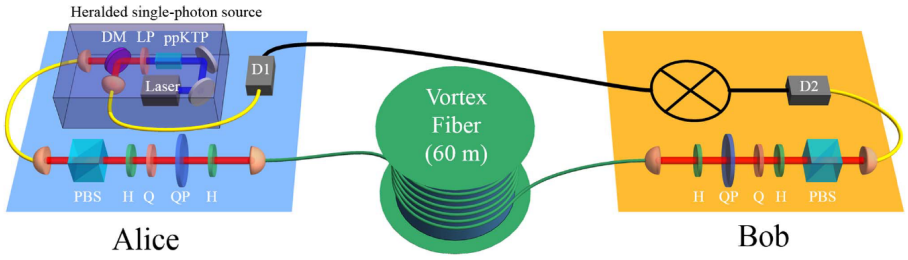

Figure 5.6: Experimental setup for performing quantum key distribution through a vortex fibre. Heralded single-photon pairs are generated through SPDC and are separated using a dichroic mirror (DM). The signal photon is then sent through a monochromator and to Alice's setup, where the single photon state is being prepared, and finally to Bob's setup where it is to be measured. The idler photon is sent to an avalanche photodiode (APD) and is used to herald the detection of the signal photon at Bob [103].

In calculation of the probability-of-detection matrix for an ideal BB84 for (d=2) as shown in the matrix 1.7, Alice sends the states, and Bob projects them, which satisfies the condition in equation(1.31). This has been recorded for a given time interval for all different states, and then the probability is plotted. For the theoretical density matrix, the diagonal and off-diagonal elements are respectively 1 and 0. However, in an experiment, due to imperfection in the generation and detection (or due to eavesdropping), these values are different. In particular, the off-diagonal terms (when Alice and Bob choose identical MUB) provide the cross-talk and the introduce noise. The quantum bit error rate (QBER) is calculated as 1 minus the on-diagonal elements of the probability-of-detection matrix.

The stages of design and adjustments as the project proceeded will be discussed. Initially, the research team attempted to use horizontal and vertical bases and anti-diagonal and diagonal. The third basis is left and right polarization; however, it did not help during the experiment since we faced a serious issue (spin-orbit coupling in our vortex fibre).

Coupling to vortex fibre is very challenging for the two bases, as it requires having the singularity that the q-plate has and the centre of the fibre aligned perfectly. Nonetheless, the two bases were enough to perform the QKD experiment with the BB84 protocol. Furthermore, it must align with the core of the vortex fibre. The bandpass filter (designed using gratings and a slit) took a considerable amount of time to be produced; such a difficulty led the team to create homemade filters to make it functional. The failure of the mentioned experiment and the homemade filter led to losing a significant number of photons. Working with two gratings, the bandpass filter caused the data flow channel to become lossy, indicating that the number of photons is low. Consequently, counting the number of photons is also considered challenging.

5.5 Results

Quantum state tomography on the states generated in Alice's setup, before and after propagating through the vortex fibre is illustrated in Figure 5.7 (b) and 5.7 (c). The red color represent the right handedness and the green color left handedness of polarization and the blue is the superposition of both polarization states. The arrow of orientation ellipse depends on the value of S_3 which will give the direction of arrow (polarization arrow). There are three case:

1 - When $S_3 > 0$, we have left handed elliptical polarization, thus the direction of arrow is clockwise on an ellipse.

2 - When $S_3 < 0$, we have right handed elliptical polarization, thus the direction of arrow is counter-clockwise on an ellipse.

3 - When $S_3 = 0$, we have linear polarization thus we have a straight line.

We simply used color instead of arrows to show the direction of the elliptical polarization with red, green and blue.

We calculate the theoretical distribution using the equation for a LG beam (Laguerre Gaussian beam equation 1.18), assuming $p = 0$ and $\ell = \pm 1$ as shown in Figure[5.7 (a)], then, we have following equation

$$LG_{0,1}\hat{e_L} \tag{5.13}$$

$$LG_{0,-1}\hat{e_R} \tag{5.14}$$

$$LG_{0,-1}\hat{e_R} \pm LG_{0,1}\hat{e_L} = (LG_{0,1} + LG_{0,-1})\hat{e_H} \pm i(LG_{0,1} + LG_{0,-1})\hat{e_V} \tag{5.15}$$

where $\hat{e}_L$ is left polarization, $\hat{e}_R$ is right polarization, $\hat{e}_H$ is horizontal polarization and $\hat{e}_V$ is vertical polarization.

The quality of the channel is quantified through a factor called fidelity. Fidelity compares the similarity between two quantum states, and is given by $(\mathrm{Tr}[\sqrt{\sqrt{\rho_{th}}\,\rho_{exp}\,\sqrt{\rho_{th}}}])^2$. Here, ρ_{th} is the theoretical density matrix operator and ρ_{exp} is the experimental density matrix operator. The experimentally measured average mode fidelity before and after the fibre is (98.8 $\pm$ 0.3)% and (93$\pm$2)% respectively illustrating good mode preservation in the fibre. Any deviation from 100 % mode fidelity will contribute as errors in the QKD channel, as long as the total error from all sources is below the error threshold. Main issue with 10s of km of fibre is losses, the light 800 nm was used for this experiment which is not the most efficient wavelength for fibers so losses can be high and likely very little light will emerge after 10 km. Best way to make this more practical is to move to a wavelength that can propagate more efficiently in fibers, this is generally around 1550 nm.

The intensity profiles at the single photon regime were obtained using a single photon sensitive camera, where each detected photon is registered as an event on a camera pixel. In the single photon regime, the vector vortex modes intensity profile gives the probability

of detecting a photon at a particular position, so by having Alice and Bob keeping the mode that is sent and the measurement basis unchanged, we can accumulate the single photon events over a long period of time. With enough time and accumulated photon detections (in the order of a few million photons), the doughnut-shape intensity profile will emerge. Also, single photon sensitive is a very generalized term for being able to measure very weak light signals. Most CCD/CMOS scientific cameras used now days are single photon sensitive ($\approx$ 50 % quantum efficiency) and those with the basic features are not expensive, the one used in this experiment the costs only $\approx$ 500 $ from Thorlabs (DCC154M) so is not difficult to acquire.

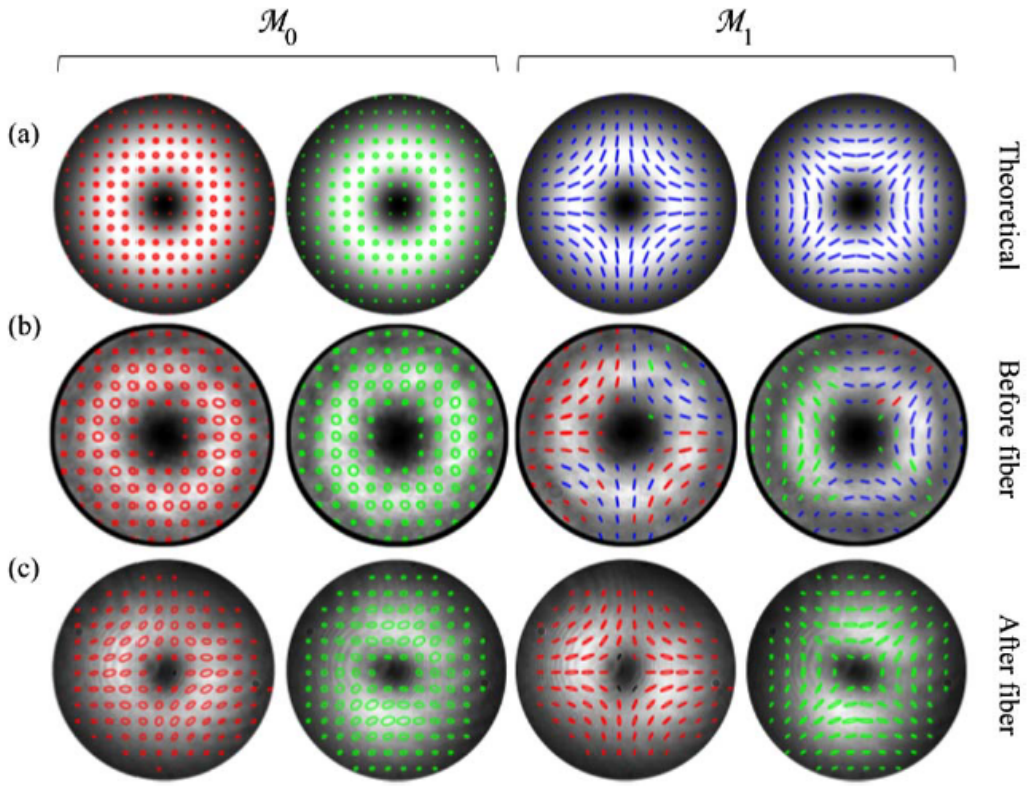

Figure 5.7: Intensity, shown in grayscale image, and polarization (overlaid colored pattern) distributions of the vortex fibre modes of $\mathcal{M}_0$ and $\mathcal{M}_1$ bases.(a) Theoretical representation, experimentally measured modes, (b) and (c) before and after the vortex fibre respectively [103].

A probability-of-detection matrices was formed using the normalized count of the her-

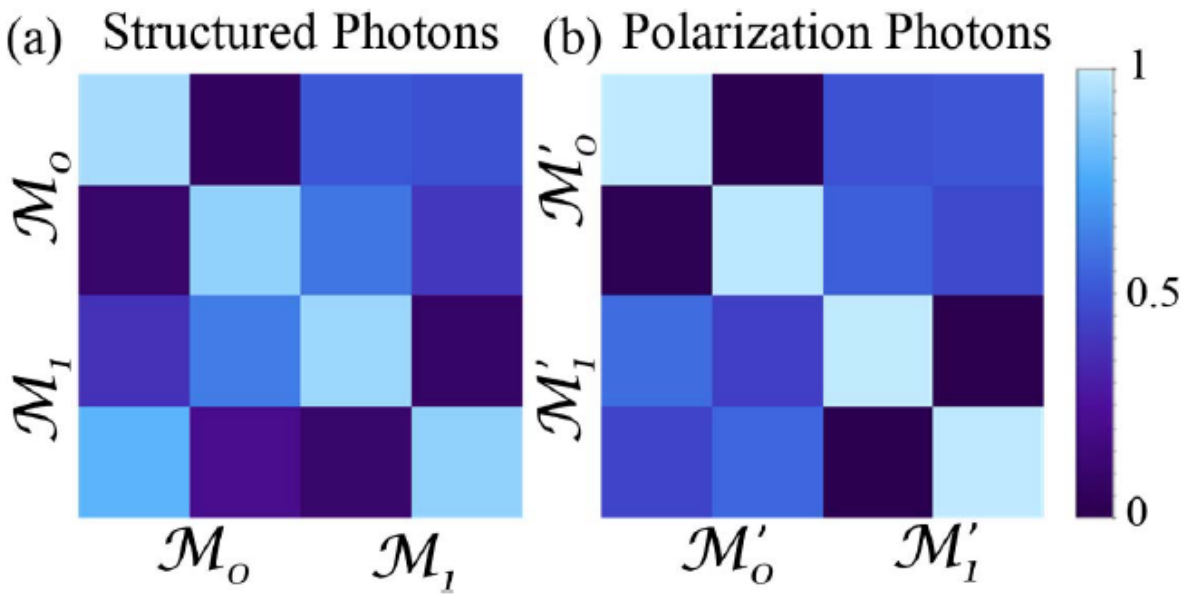

Figure 5.8: Shows the experimental measuring of the detection matrices probability for the BB84 protocol in dimension (d = 2). The rows representing the Alice send are the generation state $\mathcal{M}_0$ and $\mathcal{M}_1$, while columns measured by Bob are the projections state $\mathcal{M}_0$ and $\mathcal{M}_1$. (a) structured photons and (b) polarization photons [103].

alded single-photons which were further generated from each state: $\mathcal{M}_0$ and $\mathcal{M}_1$, and hence projecting results onto each state from $\mathcal{M}_0$ and $\mathcal{M}_1$. The probability-of-detection matrices between the MUBs sent by Alice $\mathcal{M}_0$, $\mathcal{M}_1$ and that measured by Bob $\mathcal{M}_0$, $\mathcal{M}_1$ using structured photons is shown in Figure 5.8 (a). In QKD, the threshold for quantum bit error rate (QBER) of the BB84 protocol at which the communications link is no longer considered secure is Q^{ℓ} =11%. The QBER we measured from probability-of-detection matrices, shown in Figure 5.8 (a), to be $Q^{\ell} = 8.6\%$ that is below the maximum tolerable limit [103]. Using spatial division multiplexing technique, the vortex fibre allows for simultaneous polarization only encoding with the photons having OAM $\ell = 0$. The probability-of-detection matrices for this case, polarization states, is shown in Figure 5.8(b). This is results for polarization degree of freedom and zero OAM value ($\ell = 0$). Probability-of-detection matrices has been filled for the elements as shown in Figure 1.7. The MUB for case $\ell = 0$ are $M'_0 = \{|L,0\rangle, |R,0\rangle\}$ and $M'_1 = \{(|L,0\rangle + |R,0\rangle)/\sqrt{2},\ (|L,0\rangle - |R,0\rangle)/\sqrt{2}\}$. The QBER, given by the diagonal elements of the probability-of-detection matrices, is $Q^0 =$

1.2% which is allowed multiplexing to send more information. The secret key rate for structured photon is 0.15 bits per sifted photon and the secret key rate for polarization photon is 0.81 bits per sifted photon.

This experiment serves as a technology demonstrator for implementing BB84 QKD protocol using structured photons with an OAM-preserving vortex fibre of $\ell = \pm 1$. We were able to establish a secure key between Alice and Bob below the QBER threshold of 11% for the BB84 protocol in two dimensions [103].

Chapter 6

Conclusion

In this chapter, the overall conclusions of this thesis are presented as well as plans future work.

In recent years, liquid crystals are moving beyond just display technology to wider uses such as in photonics research. In this thesis, we investigated into a few potential applications for liquid crystals devices, the spatial light modulator (SLM) and q-plate.

There has been a wide use of liquid crystal technology in recent years. Devices that are based on the properties of liquid crystals are now popular and widely used in the form of digital displays. These devices use advanced techniques to control light and produce very high-resolution and fidelity colour rich images. Furthermore, the growth of mobile computing, and the worldwide spread of smartphones are attributed to the development of liquid crystal display technology. Liquid crystal plays an important role in controlling the polarization and the beam shape and has been used in many technologies such as telecommunications [92], quantum communications[17, 103, 20] and general photonics research[6].

In the first project, liquid crystal-based SLMs are used. SLMs have the ability to control the amplitude, polarization, and phase of light. We investigated the theoretical

and experimental aspects of creating a magic mirror using a SLM. The theory behind this magic mirror follows Michael Berry's theory on the mechanisms of the magic mirror. To our knowledge, this is the first time that the magic mirror effect has been demonstrated using a SLM following Michael Berry's theory. An image is encoded into a special phase pattern that has no resemblance of the original image and is imprinted onto a SLM. So by observing the pattern of the SLM directly one cannot discern what the original image is, however, by reflecting light off this phase pattern and having the light propagated a certain distance onto a screen or camera, the original image will reappear. Experimental data are presented for the SQO and University of Ottawa's Gee-Gees logo and we are able to obtain good agreement between experimental and theoretical results. Our demonstration shows the possibility to construct a device that could help to encode hidden information on a reflective or transmissive surface.

Our results can be used as a guide on the fabrication of a new liquid crystal device which we term as the magic plate. The fabrication of the magic plate will be the next step of this project. The magic plate is essentially the same as a q-plate but with a different type of imprinted phase pattern, thus is similar to q-plate in terms of fabrication. So like a q-plate, the magic plate not only shapes the beam but can also alter the polarization of light. This will make the magic mirror/window smaller, cheaper and more portable. However, the objective is not to use the SLM to make the magic plate; the goal is to form the stage component utilizing the liquid crystal technique. The first step of this project will be the generation and the design of a liquid crystal device possessing a gentle variation of the refractive index. This refractive variation is not observable. However, when a linearly polarized light is shined on the plate, the polarization distribution of the beam will be modified according to the imprinted pattern (variation of the refractive index). Thus, even when viewed in the correct imaging plane, the hidden image still cannot be observable in intensity alone, but only through performing polarization tomography, the image can be revealed. Moreover, most of the magic mirror image is based on height, but in our case,

the image is based on reflective index. In future work, we can go to a plasmonic device where we can make a very thin device, but we still have the magic plate concept without changing the height and use the same physics.

In the second project, we explore the application of a liquid crystal device, the q-plate, in quantum communication. In this experiment, from a proof-of-principle aspect an experiment is performed to investigate the simultaneous use of a photon's spin and OAM, which is also known as a structured photon, generated through a q-plate, in QKD using the BB84 protocol through an OAM maintaining vortex fibre of 60 m. We were successful in generating a secure key between two parties with a (QBER= 8%), which is below the security threshold of 11 % for the BB84 protocol in 2 dimensions. Thus, this work demonstrate the feasibility of using structured photons in vortex fibres for long distance fibre based QKD. Also, the polarization tomography is being studied before the fibre and after the fibre and its theoretical and experimental polarization distribution for vortex fibre is compared as well. The fibre is being characterized, not only, to verify whether this vortex is suitable to consider it as a quantum channel or not, but also, to determine whether it's outcome is meeting the expectations or not. The experiment concluded, that in the quantum state, the send was not affected after passing through the vortex mode supported fibre.

The next step for this work is to use vortex fibre that supports higher values of OAM ($\pm 2, \pm 3, \pm 4, ..etc$). To support higher OAM modes a larger core radius is needed to support the larger ring at higher OAM. The access to higher OAM values increases the dimensionality of our Hilbert space. Therefore, one can demonstrate high-dimensional fibre-based QKD, increasing the amount of encoded information per photon and more error tolerance. Using 4D space will theoretically double the encoded information per photon (compared to 2D) and increase the error threshold from 11% to 19%. In addition to testing the BB84 protocol, other protocols such as Eckert91 and tomographic will also be tested

References

[1] Les Allen, Marco W Beijersbergen, RJC Spreeuw, and JP Woerdman. Orbital angular momentum of light and the transformation of laguerre-gaussian laser modes. *Physical review A*, 45(11):8185, 1992.

[2] David L Andrews and Mohamed Babiker. *The angular momentum of light*. Cambridge University Press, 2012.

[3] Sooryansh Asthana and V Ravishankar. State transfer with separable optical beams and variational quantum algorithms with classical light. *arXiv preprint arXiv:2106.00233*, 2021.

[4] SALEH BEA and MC Teich. "fundamentals of photonics". *Wiley*, page 313, 1991.

[5] Amber M Beckley, Thomas G Brown, and Miguel A Alonso. Full poincaré beams. *Optics express*, 18(10):10777–10785, 2010.

[6] Jeroen Beeckman, Kristiaan Neyts, and Pieter JM Vanbrabant. Liquid-crystal photonic applications. *Optical Engineering*, 50(8):081202, 2011.

[7] MW Beijersbergen, RPC Coerwinkel, M Kristensen, and JP Woerdman. Helical-wavefront laser beams produced with a spiral phaseplate. *Optics communications*, 112(5-6):321–327, 1994.

[8] Charles H Bennett, François Bessette, Gilles Brassard, Louis Salvail, and John Smolin. Experimental quantum cryptography. *Journal of cryptology*, 5(1):3–28, 1992.

[9] Charles H. Bennett and Gilles Brassard. Quantum cryptography: Public key distribution and coin tossing. *Theor. Comput. Sci.*, 560:7–11, 1984.

[10] Charles H Bennett and Gilles Brassard. Quantum cryptography: Public key distribution and coin tossing. *arXiv preprint arXiv:2003.06557*, 2020.

[11] Charles H Bennett, Gilles Brassard, Claude Crépeau, and Ueli M Maurer. Generalized privacy amplification. *IEEE Transactions on Information Theory*, 41(6):1915–1923, 1995.

[12] Noureddine Bennis, Jakub Herman, Aleksandra Kalbarczyk, Przemysław Kula, and Leszek R Jaroszewicz. Multifrequency driven nematics. *Crystals*, 9(5):275, 2019.

[13] Michael V Berry. Oriental magic mirrors and the laplacian image. *European journal of physics*, 27(1):109, 2005.

[14] Michael V Berry. Laplacian magic windows. *Journal of Optics*, 19(6):06LT01, 2017.

[15] Netanel Biton, Judy Kupferman, and Shlomi Arnon. Oam light propagation through tissue. *Scientific Reports*, 11(1):1–9, 2021.

[16] Ze'ev Bomzon, Gabriel Biener, Vladimir Kleiner, and Erez Hasman. Space-variant pancharatnam–berry phase optical elements with computer-generated subwavelength gratings. *Optics letters*, 27(13):1141–1143, 2002.

[17] Frédéric Bouchard, Robert Fickler, Robert W Boyd, and Ebrahim Karimi. High-dimensional quantum cloning and applications to quantum hacking. *Science advances*, 3(2):e1601915, 2017.

[18] Frédéric Bouchard, Khabat Heshami, Duncan England, Robert Fickler, Robert W Boyd, Berthold-Georg Englert, Luis L Sánchez-Soto, and Ebrahim Karimi. Experimental investigation of high-dimensional quantum key distribution protocols with twisted photons. *Quantum*, 2:111, 2018.

[19] Frédéric Bouchard, Harjaspreet Mand, Mohammad Mirhosseini, Ebrahim Karimi, and Robert W Boyd. Achromatic orbital angular momentum generator. *New Journal of Physics*, 16(12):123006, 2014.

[20] Frédéric Bouchard, Alicia Sit, Felix Hufnagel, Aazad Abbas, Yingwen Zhang, Khabat Heshami, Robert Fickler, Christoph Marquardt, Gerd Leuchs, Ebrahim Karimi, et al. Quantum cryptography with twisted photons through an outdoor underwater channel. *Optics express*, 26(17):22563–22573, 2018.

[21] Frédéric Bouchard, Natalia Herrera Valencia, Florian Brandt, Robert Fickler, Marcus Huber, and Mehul Malik. Measuring azimuthal and radial modes of photons. *Optics express*, 26(24):31925–31941, 2018.

[22] Nenad Bozinovic, Yang Yue, Yongxiong Ren, Moshe Tur, Poul Kristensen, Hao Huang, Alan E Willner, and Siddharth Ramachandran. Terabit-scale orbital angular momentum mode division multiplexing in fibers. *science*, 340(6140):1545–1548, 2013.

[23] David C Burnham and Donald L Weinberg. Observation of simultaneity in parametric production of optical photon pairs. *Physical Review Letters*, 25(2):84, 1970.

[24] WT Buttler, RJ Hughes, Paul G Kwiat, SK Lamoreaux, GG Luther, GL Morgan, JE Nordholt, CG Peterson, and CM Simmons. Practical free-space quantum key distribution over 1 km. *Physical Review Letters*, 81(15):3283, 1998.

[25] Filippo Cardano, Ebrahim Karimi, Sergei Slussarenko, Lorenzo Marrucci, Corrado de Lisio, and Enrico Santamato. Polarization pattern of vector vortex beams generated by q-plates with different topological charges. *Applied optics*, 51(10):C1–C6, 2012.

[26] Vladimir G Chigrinov. Liquid crystal devices for photonics applications. In *Passive Components and Fiber-based Devices IV*, volume 6781, page 67811M. International Society for Optics and Photonics, 2007.

[27] A Chu. Comments on" oriental magic mirrors and the laplacian image". *arXiv preprint physics/0512139*, 2005.

[28] Peter J Collings. *Liquid crystals: nature's delicate phase of matter*. Princeton University Press, 2002.

[29] Peter J Collings and John W Goodby. *Introduction to liquid crystals: chemistry and physics*. Crc Press, 2019.

[30] Peter J Collings and Michael Hird. *Introduction to liquid crystals: chemistry and physics*. CRC Press, 2017.

[31] Marcos Curty and Norbert Lütkenhaus. Intercept-resend attacks in the bennett-brassard 1984 quantum-key-distribution protocol with weak coherent pulses. *Physical Review A*, 71(6):062301, 2005.

[32] R Dabrowski, J Dziaduszek, K Garbat, Stanisław Urban, M Filipowicz, J Herman, M Czerwiński, and P Harmata. Nematic compounds and mixtures with high negative dielectric anisotropy. *Liquid Crystals*, 44(10):1534–1548, 2017.

[33] Vincenzo D'ambrosio, Filippo Cardano, Ebrahim Karimi, Eleonora Nagali, Enrico Santamato, Lorenzo Marrucci, and Fabio Sciarrino. Test of mutually unbiased bases for six-dimensional photonic quantum systems. *Scientific reports*, 3:2726, 2013.

[34] Asit Kumar Datta and Soumika Munshi. *Information photonics: fundamentals, technologies, and applications*. CRC Press, 2016.

[35] Pierre-Gilles De Gennes and Jacques Prost. *The physics of liquid crystals*, volume 83. Oxford university press, 1993.

[36] Uzi Efron. Spatial light modulators for optical information processing. In *1986 Intl Optical Computing Conf*, volume 700, pages 132–145. International Society for Optics and Photonics, 1987.

[37] Artur K Ekert. Quantum cryptography based on bell's theorem. *Physical review letters*, 67(6):661, 1991.

[38] BG Englert, D Kaszlikowski, HK Ng, WK Chua, J Rehácek, and J Anders. Highly efficient quantum key distribution with minimal state tomography, eprint. *arXiv preprint quant-ph/0412075*, 2004.

[39] WL Erikson and Surendra Singh. Polarization properties of maxwell-gaussian laser beams. *Physical Review E*, 49(6):5778, 1994.

[40] Alison D Ford, Stephen M Morris, and Harry J Coles. Photonics and lasing in liquid crystals. *Materials Today*, 9(7-8):36–42, 2006.

[41] Sonja Franke-Arnold, Les Allen, and Miles Padgett. Advances in optical angular momentum. *Laser & Photonics Reviews*, 2(4):299–313, 2008.

[42] Nahum Gat. Imaging spectroscopy using tunable filters: a review. In *Wavelet Applications VII*, volume 4056, pages 50–64. International Society for Optics and Photonics, 2000.

[43] Nicolas Gisin, Grégoire Ribordy, Wolfgang Tittel, and Hugo Zbinden. Quantum cryptography. *Reviews of modern physics*, 74(1):145, 2002.

[44] P Gregg, M Mirhosseini, A Rubano, L Marrucci, E Karimi, RW Boyd, and S Ramachandran. Q-plates as higher order polarization controllers for orbital angular momentum modes of fiber. *Optics letters*, 40(8):1729–1732, 2015.

[45] Ravindra Kumar Gupta and Achalkumar Ammathnadu Sudhakar. Perylene-based liquid crystals as materials for organic electronics applications. *Langmuir*, 35(7):2455–2479, 2018.

[46] H He, NR Heckenberg, and H Rubinsztein-Dunlop. Optical particle trapping with higher-order doughnut beams produced using high efficiency computer generated holograms. *Journal of Modern Optics*, 42(1):217–223, 1995.

[47] Engene Hecht and A Zajac. Optics forth edition, 2002.

[48] NR Heckenberg, R McDuff, CP Smith, H Rubinsztein-Dunlop, and MJ Wegener. Laser beams with phase singularities. *Optical and Quantum Electronics*, 24(9):S951–S962, 1992.

[49] NR Heckenberg, R McDuff, CP Smith, and AG White. Generation of optical phase singularities by computer-generated holograms. *Optics letters*, 17(3):221–223, 1992.

[50] Stefan W Hell. Far-field optical nanoscopy. *science*, 316(5828):1153–1158, 2007.

[51] Mark Hillery, Vladimír Bužek, and André Berthiaume. Quantum secret sharing. *Physical Review A*, 59(3):1829, 1999.

[52] Katsuhiko Hirabayashi, Hiroyuki Tsuda, and Takashi Kurokawa. Tunable liquid-crystal fabry-perot interferometer filter for wavelength-division multiplexing communication systems. *Journal of Lightwave Technology*, 11(12):2033–2043, 1993.

[53] Futoshi Hirose, Koji Nozato, Ken-ichi Saito, and Yasuyuki Numajiri. A compact adaptive optics scanning laser ophthalmoscope with high-efficiency wavefront correction using dual liquid crystal on silicon-spatial light modulator. In *Ophthalmic Technologies XXI*, volume 7885, page 788515. International Society for Optics and Photonics, 2011.

[54] Xinyao Hu, Qian Zhao, Panpan Yu, Xuanling Li, Ziqiang Wang, Yinmei Li, and Lei Gong. Dynamic shaping of orbital-angular-momentum beams for information encoding. *Optics express*, 26(2):1796–1808, 2018.

[55] Felix Hufnagel, Alessio D'Errico, Hugo Larocque, Fatimah Alsaiari, Jeremy Upham, and Ebrahim Karimi. Flat magic window. *arXiv preprint arXiv:2112.07053*, 2021.

[56] Keigo Iizuka. *Elements of Photonics, Volume I: In Free Space and Special Media*, volume 41. John Wiley & Sons, 2002.

[57] Antal Jákli. Biaxial nematic liquid crystals–theory, simulation and experiment, 2016.

[58] Y Jin, OJ Allegre, W Perrie, K Abrams, J Ouyang, E Fearon, SP Edwardson, and G Dearden. Dynamic modulation of spatially structured polarization fields for real-time control of ultrafast laser-material interactions. *Optics express*, 21(21):25333–25343, 2013.

[59] Sönke Johnsen. *The optics of life: a biologist's guide to light in nature*. Princeton University Press, 2012.

[60] Ebrahim Karimi, Lorenzo Marrucci, Corrado de Lisio, and Enrico Santamato. Time-division multiplexing of the orbital angular momentum of light. *Optics letters*, 37(2):127–129, 2012.

[61] Kedar Khare. *Fourier optics and computational imaging*. John Wiley & Sons, 2015.

[62] Jihwan Kim, Chulwoo Oh, Steve Serati, and Michael J Escuti. Wide-angle, nonmechanical beam steering with high throughput utilizing polarization gratings. *Applied optics*, 50(17):2636–2639, 2011.

[63] Naim Konforti, Emanuel Marom, and S-T Wu. Phase-only modulation with twisted nematic liquid-crystal spatial light modulators. *Optics letters*, 13(3):251–253, 1988.

[64] Mario Krenn, Robert Fickler, Matthias Fink, Johannes Handsteiner, Mehul Malik, Thomas Scheidl, Rupert Ursin, and Anton Zeilinger. Communication with spatially modulated light through turbulent air across vienna. *New Journal of Physics*, 16(11):113028, 2014.

[65] K Kugimiya. Makyoh: The 2000 year old technology still alive. *Journal of crystal growth*, 103(1-4):420–422, 1990.

[66] Hugo Larocque, Jérémie Gagnon-Bischoff, Frédéric Bouchard, Robert Fickler, Jeremy Upham, Robert W Boyd, and Ebrahim Karimi. Arbitrary optical wavefront shaping via spin-to-orbit coupling. *Journal of Optics*, 18(12):124002, 2016.

[67] Hugo Larocque, Ido Kaminer, Vincenzo Grillo, Gerd Leuchs, Miles J Padgett, Robert W Boyd, Mordechai Segev, and Ebrahim Karimi. 'twisted'electrons. *Contemporary Physics*, 59(2):126–144, 2018.

[68] Hyun-Gyu Lee, Sundas Munir, and Soo-Young Park. Cholesteric liquid crystal droplets for biosensors. *ACS applied materials & interfaces*, 8(39):26407–26417, 2016.

[69] Sensen Li, Yulei Wang, Zhiwei Lu, Lei Ding, Can Cui, Yi Chen, Du Pengyuan, Dexin Ba, Zhenxing Zheng, Hang Yuan, et al. Spatial beam shaping for high-power frequency tripling lasers based on a liquid crystal spatial light modulator. *Optics Communications*, 367:181–185, 2016.

[70] Sheng-Kai Liao, Wen-Qi Cai, Wei-Yue Liu, Liang Zhang, Yang Li, Ji-Gang Ren, Juan Yin, Qi Shen, Yuan Cao, Zheng-Ping Li, et al. Satellite-to-ground quantum key distribution. *Nature*, 549(7670):43–47, 2017.

[71] Hoi-Kwong Lo, Hoi Fung Chau, and Mohammed Ardehali. Efficient quantum key distribution scheme and a proof of its unconditional security. *Journal of Cryptology*, 18(2):133–165, 2005.

[72] H Angus Macleod. *Thin-film optical filters*. CRC press, 2017.

[73] Se-yuen Mak and Din-yan Yip. Secrets of the chinese magic mirror replica. *Physics Education*, 36(2):102, 2001.

[74] GB Malykin. Use of the poincare sphere in polarization optics and classical and quantum mechanics. review. *Radiophysics and quantum electronics*, 40(3):175–195, 1997.

[75] L Marrucci, E Karimi, S Slussarenko, B Piccirillo, E Santamato, E Nagali, and F Sciarrino. Spin-to-orbital optical angular momentum conversion in liquid crystal "q-plates": Classical and quantum applications. *Molecular Crystals and Liquid Crystals*, 561(1):48–56, 2012.

[76] Lorenzo Marrucci, Ebrahim Karimi, Sergei Slussarenko, Bruno Piccirillo, Enrico Santamato, Eleonora Nagali, and Fabio Sciarrino. Spin-to-orbital conversion of the angular momentum of light and its classical and quantum applications. *Journal of Optics*, 13(6):064001, 2011.

[77] Lorenzo Marrucci, Carlo Manzo, and Domenico Paparo. Optical spin-to-orbital angular momentum conversion in inhomogeneous anisotropic media. *Physical review letters*, 96(16):163905, 2006.

[78] Giovanni Milione, HI Sztul, DA Nolan, and RR Alfano. Higher-order poincaré sphere, stokes parameters, and the angular momentum of light. *Physical review letters*, 107(5):053601, 2011.

[79] Prasanta K. (Prasanta Kumar) Misra. *Physics of condensed matter*. Academic Press, Burlington, MA, 2011.

[80] CD Modes, M Warner, C Sanchez-Somolinos, LT De Haan, and D Broer. Mechanical frustration and spontaneous polygonal folding in active nematic sheets. *Physical Review E*, 86(6):060701, 2012.

[81] A Muller, T Herzog, B Huttner, W Tittel, H Zbinden, and N Gisin. "plug and play" systems for quantum cryptography. *Applied Physics Letters*, 70(7):793–795, 1997.

[82] Antoine Muller, J Breguet, and N Gisin. Experimental demonstration of quantum cryptography using polarized photons in optical fibre over more than 1 km. *EPL (Europhysics Letters)*, 23(6):383, 1993.

[83] Syed H Murshid. *Optical Fiber Multiplexing and Emerging Techniques*. Morgan & Claypool Publishers, 2018.

[84] Munir H Nayfeh. *Fundamentals and applications of nano silicon in plasmonics and fullerines: current and future trends*. Elsevier, 2018.

[85] Bienvenu Ndagano, Robert Brüning, Melanie McLaren, Michael Duparré, and Andrew Forbes. Fiber propagation of vector modes. *Optics express*, 23(13):17330–17336, 2015.

[86] Salah Obayya, Mohamed Farhat O Hameed, and Nihal FF Areed. *Computational liquid crystal photonics: fundamentals, modelling and applications*. John Wiley & Sons, 2016.

[87] Lynn Paterson, Michael P MacDonald, J Arlt, Wilson Sibbett, PE Bryant, and Kishan Dholakia. Controlled rotation of optically trapped microscopic particles. *Science*, 292(5518):912–914, 2001.

[88] Charles P Poole Jr. *Encyclopedic dictionary of condensed matter physics*. Academic Press, 2004.

[89] MG Rahimian, A Jain, H Larocque, PB Corkum, E Karimi, and VR Bhardwaj. Spatially controlled nano-structuring of silicon with femtosecond vortex pulses. *Scientific reports*, 10(1):1–7, 2020.

[90] Siddharth Ramachandran and Poul Kristensen. Optical vortices in fiber. *Nanophotonics*, 2(5-6):455–474, 2013.

[91] JG Rarity, PR Tapster, and PM Gorman. Secure free-space key exchange to 1.9 km and beyond. *Journal of Modern Optics*, 48(13):1887–1901, 2001.

[92] Sergio R Restaino and Scott W Teare. *Introduction to liquid crystals for optical design and engineering*. SPIE Press, 2015.

[93] Ferenc Riesz. Geometrical optical model of the image formation in makyoh (magic-mirror) topography. *Journal of Physics D: Applied Physics*, 33(23):3033, 2000.

[94] Ferenc Riesz. A note on 'oriental magic mirrors and the laplacian image'. *European journal of physics*, 27(4):N5, 2006.

[95] Andrea Rubano, Filippo Cardano, Bruno Piccirillo, and Lorenzo Marrucci. Q-plate technology: a progress review. *JOSA B*, 36(5):D70–D87, 2019.

[96] Halina Rubinsztein-Dunlop, Andrew Forbes, Michael V Berry, Mark R Dennis, David L Andrews, Masud Mansuripur, Cornelia Denz, Christina Alpmann, Peter Banzer, Thomas Bauer, et al. Roadmap on structured light. *Journal of Optics*, 19(1):013001, 2016.

[97] Neil Savage. Digital spatial light modulators. *Nature Photonics*, 3(3):170–172, 2009.

[98] Peter Schemmel, Giampaolo Pisano, and Bruno Maffei. Modular spiral phase plate design for orbital angular momentum generation at millimetre wavelengths. *Optics express*, 22(12):14712–14726, 2014.

[99] DA Seregin, AG Seregin, and MG Tomilin. Method of shaping the front profile of metallic mirrors with a given relief of its back surface. *Journal of Optical Technology*, 71(2):121–122, 2004.

[100] Peng Shi, Shi-Cheng Zhao, Yong-Jian Gu, and Wen-Dong Li. Channel analysis for single photon underwater free space quantum key distribution. *JOSA A*, 32(3):349–356, 2015.

[101] Shri Singh and David A Dunmur. *Liquid crystals: fundamentals*. World Scientific, 2002.

[102] Alicia Sit, Frédéric Bouchard, Robert Fickler, Jérémie Gagnon-Bischoff, Hugo Larocque, Khabat Heshami, Dominique Elser, Christian Peuntinger, Kevin Günthner, Bettina Heim, et al. High-dimensional intracity quantum cryptography with structured photons. *Optica*, 4(9):1006–1010, 2017.

[103] Alicia Sit, Robert Fickler, Fatimah Alsaiari, Frédéric Bouchard, Hugo Larocque, Patrick Gregg, Lu Yan, Robert W Boyd, Siddharth Ramachandran, and Ebrahim Karimi. Quantum cryptography with structured photons through a vortex fiber. *Optics letters*, 43(17):4108–4111, 2018.

[104] Alicia Sit, Lambert Giner, Ebrahim Karimi, and Jeff S Lundeen. General lossless spatial polarization transformations. *Journal of Optics*, 19(9):094003, 2017.

[105] Sergei Slussarenko, Anatoli Murauski, Tao Du, Vladimir Chigrinov, Lorenzo Marrucci, and Enrico Santamato. Tunable liquid crystal q-plates with arbitrary topological charge. *Optics express*, 19(5):4085–4090, 2011.

[106] Alexei Smolyaninov, Abdelkrim El Amili, Felipe Vallini, Steve Pappert, and Yeshaiahu Fainman. Programmable plasmonic phase modulation of free-space wavefronts at gigahertz rates. *Nature Photonics*, 13(6):431–435, 2019.

[107] Allan W Snyder and John Love. *Optical waveguide theory*. Springer Science & Business Media, 2012.

[108] Michael J Stephen and Joseph P Straley. Physics of liquid crystals. *Reviews of Modern Physics*, 46(4):617, 1974.

[109] Derek B Swinson. Chinese "magic" mirrors. *The Physics Teacher*, 30(5):295–299, 1992.

[110] US Tripathi and Vipul Rastogi. Liquid crystal-based widely tunable integrated optic wavelength filters. *JOSA B*, 36(7):1883–1889, 2019.

[111] Raju Valivarthi, Qiang Zhou, Gabriel H Aguilar, Varun B Verma, Francesco Marsili, Matthew D Shaw, Sae Woo Nam, Daniel Oblak, Wolfgang Tittel, et al. Quantum teleportation across a metropolitan fibre network. *Nature Photonics*, 10(10):676, 2016.

[112] Jayalakshmi Vallamkondu, Edwin Bernard Corgiat, Gollapelli Buchaiah, Ramesh Kandimalla, and P Hemachandra Reddy. Liquid crystals: a novel approach for cancer detection and treatment. *Cancers*, 10(11):462, 2018.

[113] Giuseppe Vallone, Davide Bacco, Daniele Dequal, Simone Gaiarin, Vincenza Luceri, Giuseppe Bianco, and Paolo Villoresi. Experimental satellite quantum communications. *Physical Review Letters*, 115(4):040502, 2015.

[114] Giuseppe Vallone, Vincenzo D'Ambrosio, Anna Sponselli, Sergei Slussarenko, Lorenzo Marrucci, Fabio Sciarrino, and Paolo Villoresi. Free-space quantum key distribution by rotation-invariant twisted photons. *Physical review letters*, 113(6):060503, 2014.

[115] Pramode K Verma, Mayssaa El Rifai, and Kam Wai Clifford Chan. *Multi-photon Quantum Secure Communication*. Springer, 2019.

[116] David Vettese. Liquid crystal on silicon. *Nature Photonics*, 4(11):752–754, 2010.

[117] Stephen Wiesner. Conjugate coding. *ACM Sigact News*, 15(1):78–88, 1983.

[118] Shin-Tson Wu, Uzi Efron, and LaVerne D Hess. Birefringence measurements of liquid crystals. *Applied optics*, 23(21):3911–3915, 1984.

[119] Lu Yan, P Gregg, Ebrahim Karimi, A Rubano, L Marrucci, R Boyd, and S Ramachandran. Q-plate enabled spectrally diverse orbital-angular-momentum conversion for stimulated emission depletion microscopy. *Optica*, 2(10):900–903, 2015.

[120] Pochi Yeh and Claire Gu. *Optics of liquid crystal displays*, volume 67. John Wiley & Sons, 2009.

[121] Juan Yin, Yuan Cao, Yu-Huai Li, Sheng-Kai Liao, Liang Zhang, Ji-Gang Ren, Wen-Qi Cai, Wei-Yue Liu, Bo Li, Hui Dai, et al. Satellite-based entanglement distribution over 1200 kilometers. *Science*, 356(6343):1140–1144, 2017.

[122] Huanguo Zhang, Zhaoxu Ji, Houzhen Wang, and Wanqing Wu. Survey on quantum information security. *China Communications*, 16(10):1–36, 2019.